Space-time variability of the Eastern Tropical Atlantic Ocean circulation and its relationship with climate indices

Isabel Cecília Arada Cardoso
Remote Sensing
Departamento de Geociências, Ambiente e Ordenamento do Território
2022

Supervisor
Clara Lázaro, Assistant Professor, FCUP

Co-supervisor
Isabel Iglesias, Researcher, CIIMAR


U.PORTO
FACULDADE DE CIÊNCIAS
UNIVERSIDADE DO PORTO

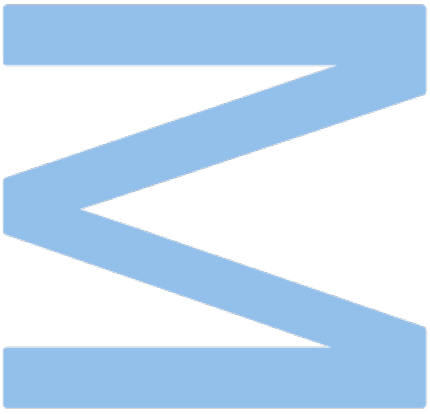

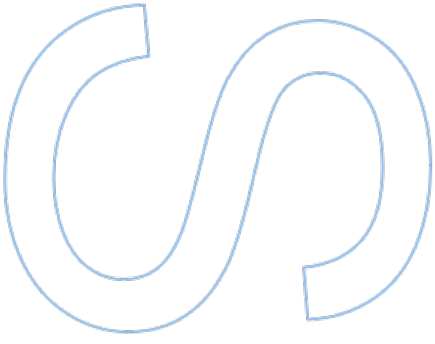

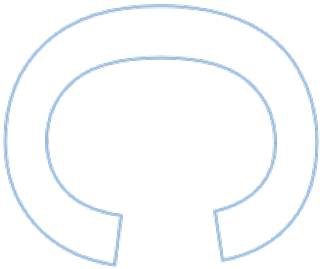

Sworn Statement

I, Isabel Cecília Arada Cardoso, enrolled in the Master Degree in Remote Sensing at the Faculty of Sciences of the University of Porto hereby declare, in accordance with the provisions of paragraph a) of Article 14 of the Code of Ethical Conduct of the University of Porto, that the content of this dissertation reflects perspectives, research work and my own interpretations at the time of its submission.

By submitting this dissertation, I also declare that it contains the results of my own research work and contributions that have not been previously submitted to this or any other institution.

I further declare that all references to other authors fully comply with the rules of attribution and are referenced in the text by citation and identified in the bibliographic references section. This dissertation does not include any content whose reproduction is protected by copyright laws.

I am aware that the practice of plagiarism and self-plagiarism constitute a form of academic offense.

Isabel Cecília Arada Cardoso

29th September 2022

Acknowledgements

To my supervisor, Professor Clara Lázaro, and to my co-supervisor, Professor Isabel Iglesias, for their support, availability, and for always pushing me to go a little further.

To my parents, for always supporting me, in this project and along all the routes I choose to take.

Thank you very much.

Last, but not least, thank you for the fun times!

Resumo

Desde 1993, as medidas de altimetria por satélite com elevada resolução espacial e temporal, a constante melhoria do seu rigor e a preocupação em assegurar a sua continuidade, têm vindo a contribuir de forma significativa para a monitorização e compreensão da dinâmica dos oceanos, no atual cenário de alterações climáticas. Este estudo pretende analisar a circulação média e sazonal do Oceano Atlântico Tropical Leste (ETAO, Eastern Tropical Atlantic Ocean) e a sua dinâmica de mesoescala através de dados de altimetria por satélite, e a avaliar a sua correlação com os índices climáticos (CI, Climate Indices) na região. Os mapas de anomalias do nível do mar (SLA, sea level anomaly), energia cinética turbulenta (EKE, eddy kinetic energy) e magnitude das correntes geostróficas de superfície foram calculados tendo por base grelhas de dados criadas a partir de observações por satélite para o oceano global entre 1993 e 2020, distribuídas pelo Copernicus Climate Change Service (C3S). Numa primeira fase, foi realizada uma caracterização prévia dos campos oceânicos globais, incluindo uma análise espácio-temporal e de variação regional, a partir da geração de mapas de tendência onde cada pixel expressa o valor numérico da tendência resultante do ajuste linear à série temporal desse pixel. Esta análise global pretendeu validar a metodologia adotada através da comparação dos resultados obtidos com os publicados em estudos prévios. Na segunda fase, foi estudada a variabilidade espácio-temporal destes campos oceanográficos para o ETAO, com o objetivo de perceber como as alterações na circulação do oceano e a variabilidade de mesoescala se correlacionam com os CI que atuam na região. As SLA, EKE e magnitude das correntes geostróficas de superfície no ETAO apresentaram uma clara sazonalidade, que parece ser fortemente influenciada pelas principais correntes da zona, em particular a Contracorrente Equatorial do Norte (NECC, North Equatorial Counter Current). Foram encontradas fortes correlações entre as SLA e vários CI como o North Atlantic Oscillation, Tropical North Atlantic, Tropical South Atlantic, Atlantic Meridional Mode, Western Hemisphere Warm Pool, e Southern Oscillation Index. Para latitudes a norte de 10°N, onde a influência da NECC é menor, a EKE parece aumentar sempre que a correlação entre as SLA e cada CI é positiva (negativa) e esse CI se encontra numa fase significativamente positiva (negativa).

Palavras-chave: Altimetria por satélite, Oceano Atlântico Tropical Leste, anomalias do nível do mar, energia cinética turbulenta, correntes geostróficas de superfície, índices climáticos, dinâmica oceânica de mesoescala.

Abstract

Since 1993, the spatial and temporal resolution of the satellite altimetric measurements, their accuracy improvement and the guarantee of their continuity, have been contributing significantly to the monitoring and understanding of the ocean dynamics in the framework of the current climate-changing scenario. This study aims to analyse the mean annual and seasonal ocean circulation and the mesoscale ocean dynamics derived from satellite altimetry in the Eastern Tropical Atlantic Ocean (ETAO), and their correlation with the climate indices that act on the region. Sea level anomaly (SLA), eddy kinetic energy (EKE) and magnitude of the surface geostrophic currents maps, used in this study, were based on a sea level daily gridded data set from satellite observations for the global ocean from 1993 to 2020, distributed by Copernicus Climate Change Service (C3S). Firstly, a global characterization of these oceanographic fields was carried out, including spatial and time series analysis, as well as the analysis of their regional change by creating trend maps in which each pixel represents the slope of the linear trend of the time series for that pixel. The purpose of this global analysis was to validate the methodology by comparison with previous studies. Secondly, the space-time variability of these oceanographic variables was then investigated in the ETAO, aiming to understand how changes in ocean circulation and mesoscale variability correlate with the climate indices that act in the region. The SLA, EKE, and magnitude fields in the ETAO showed pronounced seasonality that seems to be strongly influenced by the main currents in the area, mainly the North Equatorial Counter Current (NECC). Strong correlations have been found between SLA and several climate indices (CI), particularly the North Atlantic Oscillation (NAO), Tropical North Atlantic (TNA), Tropical South Atlantic (TSA), Atlantic Meridional Mode (AMM), Western Hemisphere Warm Pool (WHWP), and Southern Oscillation Index (SOI). Northwards of 10°N, when the influence of the NECC is weaker, the mean EKE intensity seems to increase whenever the correlation between SLA and each CI is positive (negative) and that CI is in a significantly positive (negative) phase.

Keywords: Satellite altimetry, Eastern Tropical Atlantic Ocean, sea level anomaly, eddy kinetic energy, geostrophic surface currents, climate indices, mesoscale ocean dynamics.

Table of Contents

List of Tables

List of Figures

List of Abbreviations

ACCP	Atlantic Climate Change Program
ADT	Absolute Dynamic Topography
AMM	Atlantic Meridional Mode
AMO	Atlantic Multidecadal Oscillation
aut	Autumn
C3S	Copernicus Climate Change Service
CC	Canary Current
CI	Climate Indices
CLIVAR	Climate Variability and Prediction Research Programme
CNES	Centre National d'Etudes Spatiales
DUACS	Data Unification and Altimeter Combination System
EA	East Atlantic
EA-WR	East Atlantic–West Russia
ECV	Essential Climate Variables
EKE	Eddy Kinetic Energy
ENP	Eastern North Pacific
ETAO	Eastern Tropical Atlantic Ocean
GC	Guinea Current
GCOS	Global Climate Observing System
GD	Guinea Dome
GIA	Glacial Isostatic Adjustment
ITCZ	Intertropical Convergence Zone
MC	Mauritania Current
MDT	Mean Dynamic Topography
MSS	Mean Sea Surface
NAO	North Atlantic Oscillation
NBC	North Brazilian Current
NBUC	North Brazil Undercurrent
NEC	North Equatorial Current
NECC	North Equatorial Counter Current
NEUC	North Equatorial Undercurrent
NOAA	National Oceanographic and Atmospheric Administration

nSEC	Northern branch of the South Equatorial Current
PSD	Power Spectral Density
rms	Root mean squared
s.d.	Standard deviation
SEC	South Equatorial Current
SLA	Sea Level Anomaly
SLP	Sea Level Pressure
SLR	Sea Level Rise
SOI	Southern Oscillation Index
spr	Spring
SSH	Sea Surface Height
SST	Sea Surface Temperature
SSTA	Sea Surface Temperature Anomaly
sum	Summer
TNA	Tropical North Atlantic
TSA	Tropical South Atlantic
WHWP	Western Hemisphere Warm Pool
WOCE	World Ocean Circulation Experiment
wtr	Winter

1. Introduction

The oceanic water masses are essential for the Earth's climate regulation and their warming, which has been increasing during the last decades, is changing the ecosystems' structure, organisms' biogeography, coastal ecosystems, fisheries catch, and their composition on a global scale. Beyond that, the most recent projection scenarios for the next decades, and even centuries, are nothing less than alarming (Binfoff et al., 2019). The observed accelerating sea level rise is expected to have significant impacts and consequences in the coastal areas, reducing natural habitats and biodiversity and causing lateral and inland migration, with high variations on a regional scale (Oppenheimer et al., 2019). Also, ocean circulation can be affected by the warming of the upper ocean and the change in wind stress and water fluxes caused by climate changes (Martínez-Moreno et al., 2021). Therefore, urgent mitigation actions are needed. The deep knowledge of the ocean dynamics and its interaction with the climate modes, both on a global and regional scale, is one of the essential tools to define, plan and apply them.

The Global Climate Observing System (GCOS) includes the sea level as one of the 54 Essential Climate Variables[1] (ECVs) to be monitored. This is because precision measurements of the sea level rise are critical to understanding how the climate system responds to global warming, clarifying the relative contributions of natural climate variability and anthropogenic forcing, as well to develop and validate climate models to help project future changes (Ablain et al., 2015). Before 1993, a network of coastal tide gauges was the main tool to measure sea level change. However, its sparse distribution, locations limited to coastal areas or islands, and the considerable interannual and decadal variability registered in these individual records, limited the precision of the sea level trends (Church & White, 2011). Satellite altimetry introduced the possibility of global coverage monitoring with high spatial-temporal resolution (Cabanes et al., 2001), showing that the sea level change is not uniform worldwide but is a dynamic quantity and includes, at each location, the influences of local and regional meteorological effects, modes of climate variability and long-term trends (Church & White, 2011).

Satellite altimetry has been used in several studies to investigate the relation between sea level variations and atmospheric teleconnection patterns and/or oceanic modes

[1] https://gcos.wmo.int/en/essential-climate-variables/table

(Iglesias et al., 2017, Chafik et al., 2017, Efthymiadis et al., 2002, Woolf et al., 2003, Park et al., 2019). However, most of these studies focus mainly on wide and/or highly energetic regions of the North Atlantic or North Pacific oceans. Focusing on either smaller or less energetic areas may unveil connections overshadowed by the influence of stronger relations, allowing detailing the analysis as if it would be viewed with a magnifying lens, and therefore complementing the existing knowledge.

The eastern tropical ocean basins are known to be low-energy regions in terms of ocean circulation and associated variability and therefore have received lesser attention than their western counterparts, where the strongest currents flow. However, significant atmosphere-ocean interaction takes place in these regions, which is crucial to variability across sub-seasonal to decadal time scales (Roberts & Clayson, 2012). Moreover, the World's major areas of permanent upwelling are found in these regions (Kämpf & Chapman, 2016b), associated with the cold eastern boundary currents (e.g. Canary and California currents in the Northeast Atlantic and Pacific oceans, respectively). Upwelling brings oxygen and nutrients from depth to the surface, allowing the growth of Phyto and zooplankton, which in turn allow the development of the food chain and the region's biodiversity (fishes, mammals, seabirds, etc.). Consequently, these regions are among the World's most fertile ecosystems and there is an urgent need to preserve these coastal ecosystems which could be endangered as a response to ocean warming, acidification and oxygen loss (Binfoff et al., 2019). The understanding of the dynamics of the ocean circulation in these regions, as well as their role in the earth's climate, is therefore of vital importance.

1.1 Overview of satellite altimetry, its current applications, and potential

Satellite radar altimetry has already celebrated its 29th anniversary and exceeded all the initial expectations as it has been continuously proving its value in a diversity of fields such as (Abdalla et al., 2021):

- monitoring and understanding the ocean dynamics in the Earth's climate system;
- determining the sea level rise (SLR) and assessing its acceleration rate;
- monitoring coastal areas and predicting their evolution to assess eventual hazards impacting both ecological niches as well as human society and economy;

- studying inland waters such as lakes, rivers, estuaries, reservoirs, and flood plains;
- evaluating the ice-covering behaviour in the polar regions and the polar oceans' circulation and their relation with global warming and climate changes;
- providing useful information to help measure several ocean biological parameters.

Since its initial days at the beginning of the 1990s, major technical improvements have been achieved in reducing instrumental errors and improving orbital reference accuracy (Abdalla et al., 2021). The simultaneous operation of, at least, two missions (from reference, complementary, and opportunity missions), allowed the combination of their data to resolve space and time scales of the ocean circulation, creating homogenized merged maps and reducing the mapping errors (Ducet et al., 2000). The spatial and temporal resolution of the altimetric measurements, jointly with their accuracy, and continuity, provide a data coverage that allows the global and mesoscale analysis of the ocean circulation and its variability, not only on a short-time basis but also on its long-time effects.

Three oceanographic fields derived from satellite altimetry are fundamental for ocean circulation studies: the sea level anomaly (SLA), the eddy kinetic energy (EKE) per unit mass (hereafter referred to solely as eddy kinetic energy or EKE), and the surface geostrophic currents. The SLA is the anomaly of the ocean signal as referred to as its mean component (Tabburet et al., 2021). The magnitude of the ocean currents may be quantified by the total kinetic energy (KE) which, in turn, can be divided into the mean kinetic energy (MKE) and the EKE. While the first is determined by the time-mean velocity field, the latest is determined by the time-varying velocity and is, therefore, dominated by the mesoscale (i.e., spatial scale from about 10 to 100 km) variability (Martínez-Moreno et al., 2021). Mesoscale flows impact the sea surface height (SSH), the sum of the Mean Sea Surface (MSS) and the SLA or, alternatively, the sum of the geoid undulation (N) and the Absolute Dynamic Topography (ADT), the variable of interest for ocean circulation studies (equations below).

$$SSH = MSS + SLA \quad \text{Eq. 1}$$

$$SSH = ADT + N \quad \text{Eq. 2}$$

Therefore, to derive the ADT from satellite altimetry, the knowledge of the geoid with the same accuracy (centimetre level) is needed.

The combination of the previous equations shows that the ADT can be derived from satellite altimetry SLA, provided the Mean Dynamic Topography (MDT) is known, according to the following equations.

$$MDT = MSS - N \quad \text{Eq. 3}$$

$$ADT = SLA + (MSS - N) \quad \text{Eq. 4}$$

ADT gradients along the zonal and meridional directions are proportional to the components of the surface geostrophic flow along the same directions, so the absolute geostrophic velocities (zonal component – *u* and meridional component – *v*) are computed using the equations below (Rummel & Sansò, 1993).

$$u = -\frac{\gamma}{fR}\frac{\partial \zeta}{\partial \varphi} \quad \text{Eq. 5}$$

$$v = \frac{\gamma}{fRcos\varphi}\frac{\partial \zeta}{\partial \lambda} \quad \text{Eq. 6}$$

where γ is the normal gravity, ζ is the absolute dynamic topography, φ and λ are the latitude and longitude, respectively, $f = 2\omega_e sin\varphi$ is the Coriolis parameter, R is the Earth's radius and ω_e is the Earth's angular velocity.

The magnitude of the surface geostrophic velocity is then computed using the following equation.

$$mag = \sqrt{u^2 + v^2} \quad \text{Eq. 7}$$

SLA gradients are proportional to the time-varying surface geostrophic flow, from which EKE per unit mass can be computed, according to the equations below. Consequently, eddy-rich regions can be identified through the knowledge of EKE (Martínez-Moreno et al., 2021).

$$u' = -\frac{\gamma}{fR}\frac{\partial \zeta'}{\partial \varphi} \quad \text{Eq. 8}$$

$$v' = \frac{\gamma}{fRcos\varphi}\frac{\partial \zeta'}{\partial \lambda} \quad \text{Eq. 9}$$

$$EKE = \frac{1}{2}(u'^2 + v'^2) \quad \text{Eq. 10}$$

where *u'* and *v'* are the geostrophic velocity anomalies components and ζ' is the SLA.

1.2 Climate indices in the Eastern Tropical Atlantic Ocean

The Earth's climate system components exchange mass, momentum, and energy on all time scales. Global or regional-scale climate variables fluctuate almost regularly. Many of these fluctuations are known as modes or oscillations, and their states are monitored by climate indices (CI), which are scalar values resulting from a combination of several climate variables – e.g. sea surface temperature (SST), surface pressure, wind speed, and rainfall – that allow monitoring the modes of the referred fluctuations (de Viron et al., 2013). Teleconnections between these indices are known to exist, as they describe the climate links between two regions separated by long distances, which can go up to opposite locations on Earth, spatially represented by patterns based on the correlation strength of the indices (Wagner et al., 2021). Therefore, the teleconnection indices describe the preferred modes of low-frequency (longer than 1-2 weeks) variability in these two or more strongly coupled together centres of action and highlight the coupling between the planetary-scale circulation quasi-stationary upper air and the short-term climatic fluctuations near the surface (Panagiotopoulos et al., 2002). Since they influence the atmospheric temperature and precipitation regimes, they govern the location and intensity of jet streams and the corresponding storm tracks. At the same time, they can produce anomalous weather patterns that take place over different regions simultaneously and persist for a long period (Panagiotopoulos et al., 2002).

The most important CI that may influence the Eastern Tropical Atlantic Ocean (ETAO) climate were identified and analysed. Table 1 summarizes those that have been considered the most relevant for the study area, according to the information provided on the National Oceanographic and Atmospheric Administration (NOAA) Physical Sciences Laboratory webpage[2] and the Climate Prediction Center webpage[3].

The North Atlantic Oscillation (NAO) is one of the most dominant teleconnections in the North Atlantic, associated with the gradient of the sea level pressure (SLP) between two negatively correlated centres, a low-pressure one in the subpolar region over Greenland and a high pressure one on the subtropical North Atlantic – Azores (Panagiotopoulos et al., 2002). The NAO index reflects the strength of the atmospheric forcing over the North Atlantic region, especially during winter, so that, during its positive phase, the prevailing westerly winds are particularly strong, inducing higher-

[2] https://psl.noaa.gov/data/climateindices/list/
[3] https://www.cpc.ncep.noaa.gov/data/teledoc/telecontents.shtml

intensity storms. During its negative phase, the weaker-than-normal winds cause the southward shift of the jet stream and, consequently, also of the storm tracks (Chafik et al., 2017). Hence, along with the increased storming and precipitation in northern Europe during the NAO positive phases, the air masses arriving from lower latitudes also bring warmer than average temperatures, while in southern Europe storm intensity and precipitation stay below average. The opposite occurs during the negative phases (Donev, 2017). Historical data also suggest that the NAO presents important interannual and interdecadal variability, more pronounced since the 1950s (Panagiotopoulos et al., 2002). Since the fundamental mechanisms of NAO are still unclear, the role of anthropogenically-induced climate change is yet to be determined in the NAO increasing trend over the last decades (Stephenson et al., 2000). Western and eastern Europe's climate is therefore strongly influenced by the NAO, as well as the North Atlantic oceanic ecosystems (Stephenson et al., 2000), although some findings suggest that other leading modes may also need to be taken into account to justify the forcing mechanisms (Chafik et al., 2017).

Figure 1 illustrates the NAO SLP difference during its positive and negative phases.

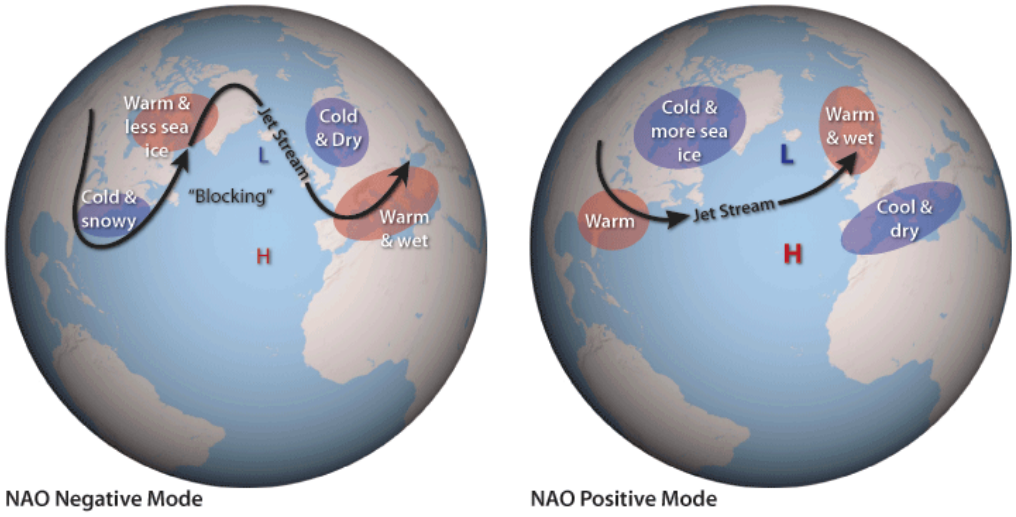

Figure 1 – Illustration of NAO SLP in its negative and positive modes (image source: NOAA[4])

[4] National Oceanic and Atmospheric Administration. (July 22, 2016). ''NAO Modes'' [Online]. Available: https://www.climate.gov/sites/default/files/NAO_Schematic_0.png

The Tropical North Atlantic (TNA) and the Tropical South Atlantic (TSA) indices were defined in 1999, aiming to determine the degree of occurrence of sea surface temperature anomalies (SSTA) of opposite signs, in each tropical Atlantic hemisphere (Enfield et al., 1999). Although a dominant dipole mode was not found, the SSTA gradient of the tropical oceans of each hemisphere tropical ocean is still an important tool for analyse the Atlantic climate (Enfield et al., 1999).

Covering both the TNA and TSA areas, the Atlantic Meridional Mode (AMM) is characterized by the north-south interhemispheric SSTA gradient (Servain et al., 1999). Its fluctuations have been associated with strongly coupled ocean-atmosphere variability in the Tropical Atlantic related to hurricane activity, even though its maximum variance usually occurs during boreal spring (Vimont & Kossin, 2007). The AMM may also indirectly influence the transport and availability of nutrients in the tropical band since its negative (positive) phases have been associated with a southward (northward) shift of the Intertropical Convergence Zone (ITCZ) (Skliris et al., 2022). Some extreme negative AMM phases have also been related to stronger easterly winds in the tropical and subtropical eastern North Atlantic, impacting the coastal upwelling and the North Equatorial Current (NEC) strength and, consequently, the nutrients transport course in this area (Skliris et al., 2022).

The Western Hemisphere Warm Pool (WHWP) of sea surface water warmer than 28.5 °C is the second-largest tropical warm pool and it is located entirely north of the equator, between 7°N and 27°N, extending from the Eastern North Pacific (ENP) 110°W up to the east of the Caribbean, around 50°W (Wang & Enfield, 2001). Since during boreal winter the water is always below 28.5 °C in this area, the WHWP only starts to develop during spring in ENP, expanding eastward during summer and reaching its eastern limit in late summer/early autumn. This is related to the weaker easterly winds in the tropical North Atlantic, a warmer and moister troposphere, and reduced SLP, which favour the formation of storms (Wang & Enfield, 2001). Apart from a seasonal cycle, WHWP also presents important interannual and longer-time scale variability (Wang & Enfield, 2001). Strong warm pools do not always develop, and the NAO seems to introduce constructive or destructive interference in WHWP. For a strong warm pool to be likely to develop, beyond the persistence of the SSTA in the eastern Pacific during boreal winter and spring (e.g. El Niño events), a negative winter NAO pattern should evolve to reinforce the signal from the Pacific. On the other hand, a positive NAO will likely mitigate the atmospheric bridge from the Pacific, minimizing the Atlantic warm pool (Enfield et al., 2006).

Figure 2 shows the location of the TNA, TSA, AMM and WHWP areas, relative to the study area (shadowed in red).

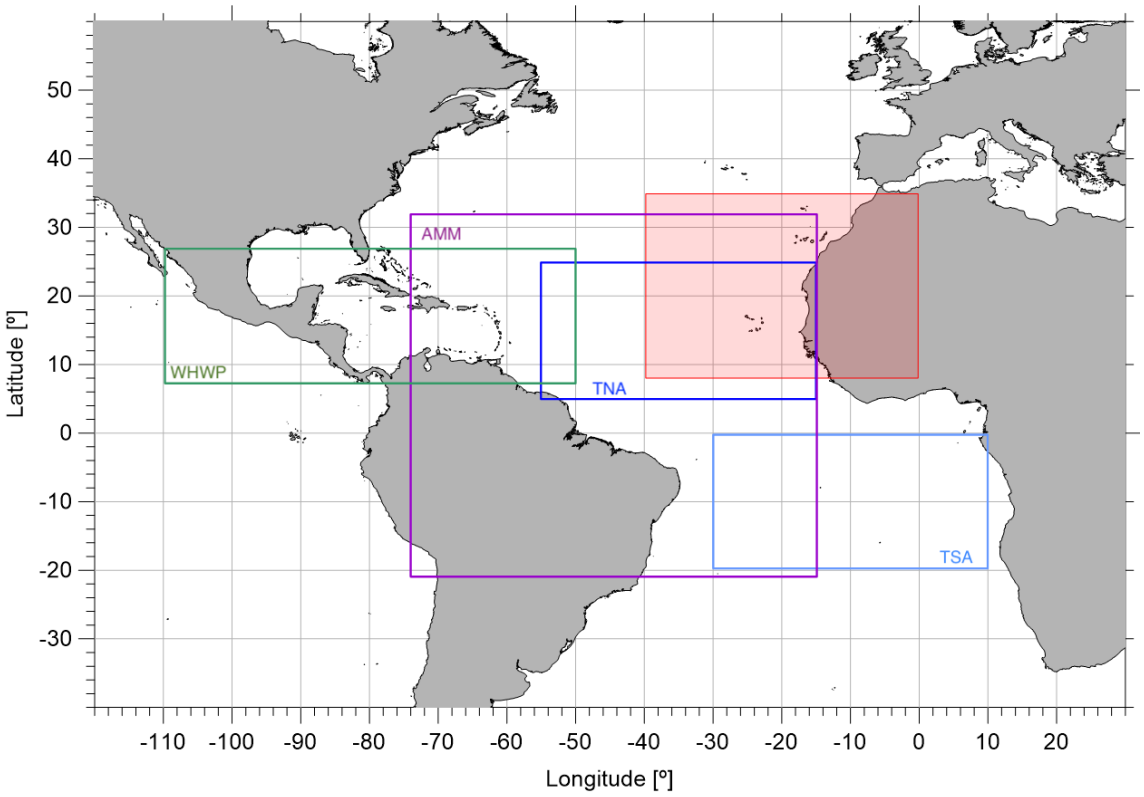

Figure 2 – Schematic location of the TNA, TSA, AMM and WHWP areas (study region shaded in red).

The Southern Oscillation Index (SOI) measures the sea surface pressure anomalies in two locations, Tahiti and Darwin, Australia, indicating whether the large-scale circulation of the atmosphere over the tropical Pacific is stronger (La Niña events) or weaker (El Niño events) than normal (Lindsey, 2009). It is one of the indices used to assess the strength of El Niño and La Niña events, since its negative phase coincides with abnormally warm water in the eastern tropical Pacific Ocean, typical of El Niño, while its positive phase coincides with abnormally cold water, typical of La Niña[5].

Figure 3 illustrates the SOI SLP difference during its positive and negative phases.

[5] https://www.ncei.noaa.gov/access/monitoring/enso/soi.

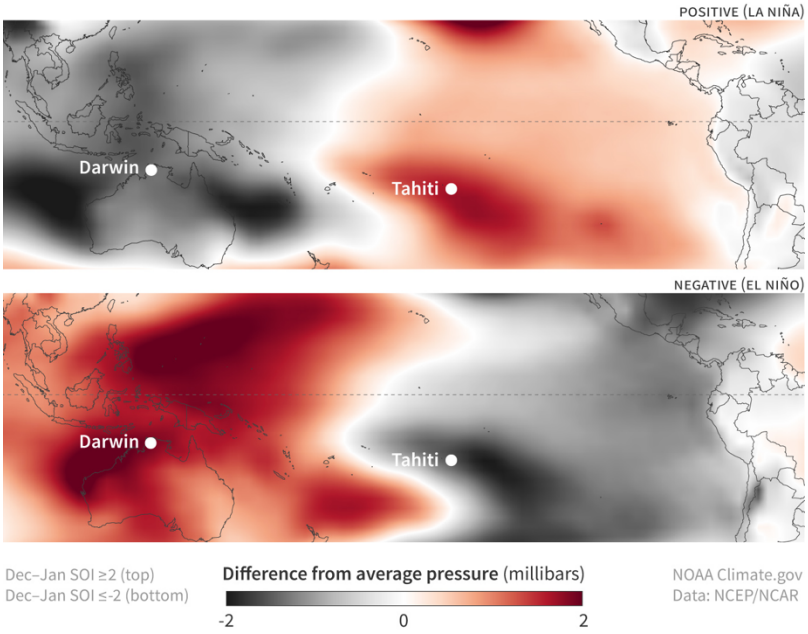

Figure 3 – Difference of average SLP during winter when SOI is positive (top image) or negative (bottom image) (image source: NOAA[6]).

Table 1 – Summary of the CI used in the analysis: description and geographic location.

Index	Location	Description
NAO – North Atlantic Oscillation	20N° – 80°N 90°W – 40°E (Hurrel, 1995)	Difference of surface SLP between a dipole of anomalies located over Greenland (low) and the subtropical – Azores area (high).
TNA – Tropical Northern Atlantic	5°N – 25°N 55°W – 15°W	Anomaly of the average monthly SST in the eastern tropical North Atlantic Ocean.
TSA – Tropical Southern Atlantic	20°S – 0.0° 30°W – 10°E	Anomaly of the average monthly SST in the eastern tropical South Atlantic Ocean.
AMM – Atlantic Meridional Mode	21°S – 32°N 74°W – 15°E	SST meridional variability in the tropical Atlantic Ocean.
WHWP – Western Hemisphere Warm Pool	7°N – 27°N 110°W – 50°W (Wang & Enfield, 2001)	Monthly anomaly of SST in the region where the water is warmer than 28.5° C (Wang & Enfield, 2001).
SOI – Southern Oscillation Index	-	Difference of surface SLP between a dipole of anomalies located over Tahiti and Darwin, Australia.

[6] National Oceanic and Atmospheric Administration. (August 30, 2009). 'Climate Variability: Southern Oscillation Index'' [Online]. Available: https://www.climate.gov/media/13062

1.3 Motivation and objectives

When studying climate problems, the knowledge of the tropical ocean circulation is of utmost importance given the large heat storage in this region (Arnault & Fonds, 1987). The ETAO has been studied by several authors relating to the variability of surface circulation (Lázaro et al., 2005), oceanographic characterization and sea level rise (Fernandes & Lazaro, 2005; Sarr et al., 2021), energy conversion (Erasmi et al., 1998) and current and flow systems (Peña-Izquierdo et al., 2012; Vangriesheim et al., 2003), but the relationship between ocean circulation and climatic indices have mainly been focused in northern latitudes (Iglesias et al., 2017).

This study aims to extend the scope of previous works by trying to relate several oceanographic variables with climatic indices in the southeastern region of the North Atlantic Ocean. In that perspective, it focused on the scarcely studied ETAO region between 3°N to 30°N and 40°W to 0°, to investigate the space-time variability of the SLA, EKE and surface geostrophic velocity, and their relation to the climate indices (CI) on the region. Taking advantage of the length of the presently available altimeter dataset, a study period of 28 years (between 1993 and 2020) was considered, to maximize the accuracy of the interannual signals to be analysed. In addition to each variable mean time series, including the discrimination of the annual, interannual and residual components, this time window also provides the possibility to study each variable regional change by creating “trend maps”. In these maps, each pixel represents the slope of the linear trend, fitted to the interannual signal of the variable time series for that pixel. This approach is usually applied to characterize the SLA regional change, and several studies have been published by different study groups[7]. However, results of its application to both EKE and magnitude fields have hardly been published in the literature.

The detailed analyses of these variables are, therefore, expected to improve the current knowledge of how they change in the ETAO region and how they might relate to the atmosphere, through their correlation with climate indices.

[7] https://sealevel.colorado.edu/data/sea-level-trends-satellite-altimeters and https://www.aviso.altimetry.fr/en/data/products/ocean-indicators-products/mean-sea-level.html#c15717

1.4 Thesis structure

This dissertation is structured as follows. Section 1 introduces an overview of the altimetry products' current application and potential, describes the most common CI in the ETAO, and presents this study's motivation and objectives. Section 2 describes the data used in the study and the adopted data processing methodology, the oceanographic characterization of the study area, the implemented processing tools, and the calculation approach. In section 3, the results and discussion are presented. The conclusions are presented in section 4. Finally, suggestions for further work are proposed in section 5.

2. Data and Methodology

2.1 Study Area

The ETAO between 3°to 30°N and 40°W to 0° is an area of interaction of several currents as well as intense trade winds which induce coastal circulation (Figure 4), potentially favouring coastal upwelling and marine diversity. This area is largely affected by the Intertropical Convergence Zone (ITCZ), a permanent low-pressure feature over the Atlantic and the Pacific oceans around latitude 7°N (Wallace & Hobbs, 2006) where the north-easterly and south-easterly trade winds converge and, together with the heat and moisture from the surface evaporation, create an area of increased precipitation, marking the meteorological equator (Waliser & Jiang, 2015). The seasonal shift of the ITCZ along the meridional direction, following the migration of the sun towards the warmer hemisphere, influences climate not only in the tropical band but also globally (Zhang et al., 2021). During the boreal summer months, when the southeast trade winds are more intense so that they extend to the northern hemisphere and the ITCZ is between 10° and 15°N, the surface ocean currents are stronger in the Tropical Atlantic (Philander, 2001). On longer timescales, shifts in the ITCZ position over the Atlantic Ocean have been related to solar luminosity and volcanic events, while variations over the Pacific and Indian Oceans seem to mostly induce fluctuations in atmosphere and ocean states (Roldán-Gómez et al., 2022).

Between latitudes 3° and 10°N, the eastward flowing North Equatorial Counter Current (NECC) prevails, bordering north with the westward North Equatorial Current (NEC) and south with the northern branch of the South Equatorial Current (nSEC) (Hormann et al., 2012). Being partially fed by the retroflection of the North Brazilian Current (NBC), it extends east towards the Gulf of Guinea feeding the Guinea Current (Dimoune et al., 2020), and providing oxygen-rich water to the tropical North Atlantic low oxygen warm waters (Hormann et al., 2012). When reaching the African continental slope, part of the NECC flow drifts north along the coast in the so-called Mauritania Current (MC), following the NECC seasonality (Fernandes & Lazaro, 2005). The geostrophic velocities of the NECC present a strong seasonal variation, with a maximum in late summer/early autumn (30 cm/s at 7°N in October) and decreasing to a minimum in spring (6 cm/s at 7°N in April) (Richardson et al., 1992).

Both the NEC and the SEC flow westward, the former between approximately 7° and 20°N, being fed by the northeast Atlantic waters, forming the southern limb of the North

Atlantic subtropical gyre and coming to its maximum during the boreal summer (Bischof et al., 2004). The SEC, on the other hand, extends from around 4°N to 15-25°S, depending on the longitude and the season (Bonhoure et al., 2004). The bifurcation of the SEC into the Brazil Current (BC) to the south and the North Brazil Undercurrent/Current (NBUC/NBC) to the north changes both in latitude and depth, occurring between 10°S and 20°S in the surface layer (top 100 m) (Stramma & Schott, 1999) and reaching south of 27°S at 1000 m (Rodrigues et al., 2007). In the top layer, it reaches its southernmost position in July and its northernmost position in November, associated with changes in the local wind stress curl related with the ITCZ migration (Rodrigues et al., 2007). Its geostrophic velocities present two maxima throughout the year: in July at 1°N and in November at 2°N (Richardson et al., 1992).

Around 10°N and 22°W another feature develops during summer, the Guinea Dome (GD), associated with the northward shift of the ITCZ (Doi et al., 2009). When the geostrophic flow contributions of the NECC, the North Equatorial Undercurrent (NEUC), and the NEC strengthen the GD, the resulting increase in surface nutrients impact the chlorophyll-*a* concentration and influence biological activities in the area (Doi et al., 2009).

The Canary Current (CC) flows south-westward from around 33°N along the African coast, bringing cool water from the north and also from the coastal upwelling waters up until around 20°N when it starts to flow west under the influence of the NEC (Mittelstaedt, 1991). This current, associated with intense coastal upwelling, is mostly driven by the trade winds along the coast (Philander, 2001) and it becomes stronger during winter following the strengthening of the winds (Gyory et al., 2013). Along with the NECC, it also feeds the Guinea Current that flows eastwards at around 3°N and presents an intensification during the boreal summer (Gyory et al., 2005)

Table 2 presents a summary of the main currents in the study area indicating their seasonality.

Table 2 – Summary of the ocean current in the study area and their seasonality.

Current	Winter (wtr)	Spring (spr)	Summer (sum)	Autumn (aut)	Winter (wtr)
NECC		min	max		
MC			max		
NEC			max		
SEC			max	max	
CC	max				
GC			max		
GD			max		

In addition to these currents, the northwest African coast is also identified as one of the major upwelling regions in the world (Kämpf & Chapman, 2016b). Three different systems can be identified within the study area (Figure 4): a continuous wind-driven upwelling north of 20°N (north of 25°N its maximum intensity occurs during summer and early autumn); a seasonal, also wind-driven, upwelling from Cape Blanc down to Dakar with maximum intensity during winter and spring (Mittelstaedt, 1991); and a seasonal upwelling system along the zonal oriented coast of the Ivory Coast and Ghana, from July to October (Kämpf & Chapman, 2016a). These upward movements of cold subsurface water masses are essential to provide these areas with nutrients, consequently increasing biological productivity (Mittelstaedt, 1991), expanding primary production, and supporting local economies (Narayan et al., 2010).

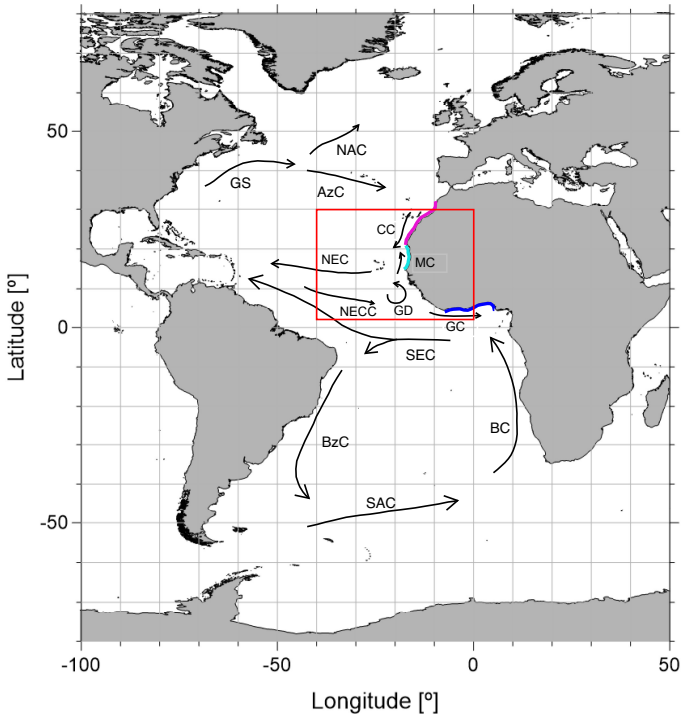

Currents within the study area:

- CC – Canary Current
- MC – Mauritania Current
- NEC – North Equatorial Current
- NECC – North Equatorial Counter Current
- GD – Guinea Dome
- GC – Guinea Current
- SEC – South Equatorial Current

Upwelling systems (flagged in colour):

- Pink – continuous (wind-driven)
- Light blue – seasonal (wind-driven)
- Dark blue – seasonal (other)

Other main currents in the Atlantic Ocean:

- GS – Gulf Stream
- AzC – Azores Current
- NAC – North Atlantic Current
- BzC – Brazil Current
- SAC – South Atlantic Current
- BC – Benguela Current

Figure 4 – Schematic representation of the main currents and upwelling systems in the study area (delimited by the red rectangle).

2.2 Data and Processing

The altimeter data used in this study were downloaded from the Copernicus Climate Change Service – C3S webpage[8] and correspond to the reprocessed DUACS (Data Unification and Altimeter Combination System) Delayed-Time vDT2021products.

The along-track data only allow us to obtain the cross-track component of the geostrophic velocities while the gridded data provide independent information both on zonal and meridional geostrophic velocities (Ducet et al., 2000). Gridded products were chosen for this study because one of the objectives was to analyse not only the SLA interaction with climate anomalies but also the EKE and geostrophic velocities space-time variability. C3S Delayed-Time vDT2021 Level 4 gridded products have been created by combining cross-calibrated altimeter measurements from several missions – reference missions (Topex/Poseidon, Jason-1, Jason-2, and Jason-3) and complementary missions (ERS-1, ERS-2, Envisat, SARAL/Altikaand presently Sentinel-3A) – to create global maps (Taburet et al., 2021). Considering the different missions, the best spacing between two adjacent satellite tracks, and therefore the best spatial resolution on the ground, varies, in the study region, from 80 km at latitude 3°N to 69 km at latitude 30°N.

To assure the long-term stability of these delayed-time gridded products, several additional improvements have been taken into account in the mapping procedure (Taburet et al., 2021):

- global and regional inter-mission biases have been removed;
- along-track measurements have been cross-calibrated, allowing for the reduction of the long wavelength errors as well as the geographically correlated errors;
- high frequency aliased signals have been removed;
- data have been filtered using a 65 km cut-off length filter;
- along-track measurements have been subsampled for the mapping, keeping one along-track point out of two.

SLA and geostrophic velocities are available in ¼° spatial resolution daily gridded maps from 1993 to the present, disseminated to users in NetCDF (Network Common Data Form) format and using CF (Climate and Forecast) Metadata convention. In order to include only complete years, the study was limited to the period from 1993 to 2020.

[8] https://cds.climate.copernicus.eu/cdsapp#!/dataset/satellite-sea-level-global?tab=form

The CI monthly time series were extracted from the National Oceanographic and Atmospheric Administration (NOAA) Physical Sciences Laboratory webpage[9] and the Climate Prediction Center webpage[10].

Data processing and computation were performed in *Matlab R2020a* and *Surfer 11* software. All scripts for the processing and analysis of satellite altimetry have been implemented in the scope of this study. These include: scripts to compute the maps for the 28-year correction of SLA, surface geostrophic velocity anomalies and EKE and, for each variable, the root mean square (rms), variance and trend maps, the variance decomposition and seasonal means maps, the time series, time series decomposition and power spectrum density (PSD) graphics, and the seasonal means graphics for each climate index. Correlation maps were computed using a *Matlab* script kindly made available by Professor Isabel Iglesias. All figures included to illustrate the results were created either in *Surfer 11 (Golden Software)* or *Matlab*.

2.3 Methodology

The altimeter data were used to derive several oceanographic variables, using the methodology described in the following subsections. In a second step, the correlation between these variables and the selected CI were computed. The main steps of the processing methodology are summarized in Figure 5.

[9] https://psl.noaa.gov/data/climateindices/list/
[10] https://www.cpc.ncep.noaa.gov/data/teledoc/telecontents.shtml

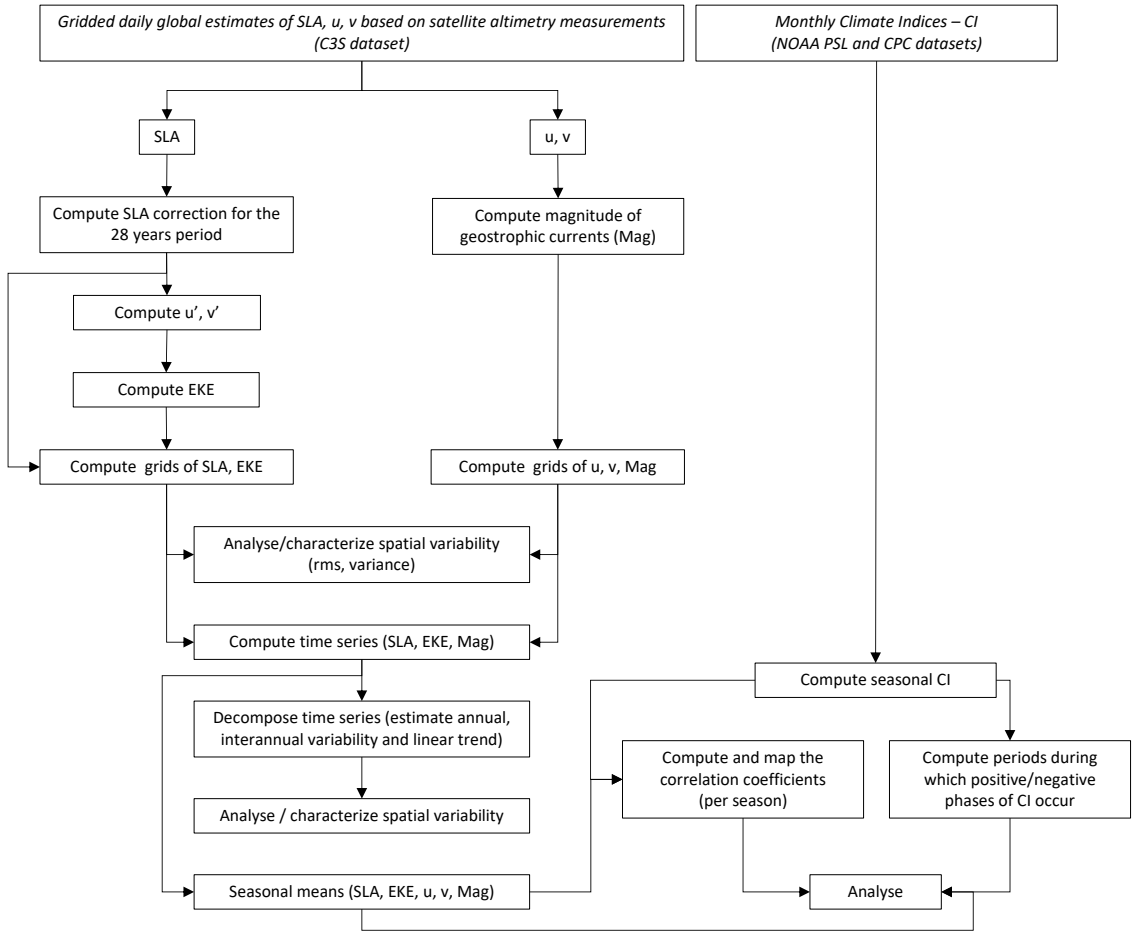

Figure 5 – Summary of the main steps considered in this study. Boxes with italic text represent data downloaded from exterior sources.

2.3.1 Pre-processing of satellite altimetry

SLA represent variations of the sea level relative to a given reference period, resulting that the mean SLA for the same period should generally converge to zero. In the C3S reprocessed DUACS Delayed-Time vDT2021 products, the SLA and the ADT are computed considering the 20-year reference period from 1993 to 2012 (Taburet et al., 2021). The mean SLA for the period 1993-2012 is presented in Figure 6 where zero or close to zero values are observed. The explanation of not having an exact zero at some locations is related to the mean reference convention adopted in the DUACS products, which arbitrarily referenced the sea level time series so that its mean average during the year 1993 is set to zero which, as a consequence of the sea level rise during the 20 years period 1993-2012, returns a mean average of about 2.5 cm (without Glacial Isostatic Adjustment – GIA correction) (Mertz & Legeais, 2020).

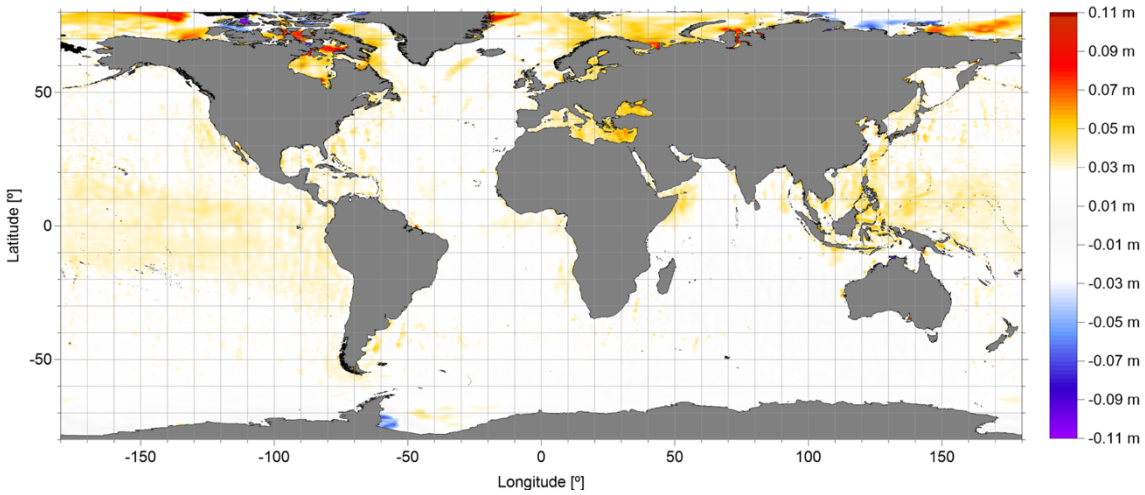

Figure 6 – Mean overall SLA for the period 1993-2012.

Since the present study covers the 28-year period from 1993 to 2020, events occurring between 2013 and 2020 (e.g. interannual variability occurring during these years) are not included in the C3S reference period. As a consequence, when the 1993-2020 mean SLA is computed, those signals, that should have been included in the reference period, appear (Figure 7) leading to SLA values that significantly depart from zero.

High latitude results presented in the C3S daily grids should be evaluated with caution, since the validity of altimeter data depends, on the one hand, on the ice coverage and, on the other hand, only the complementary missions acquire data up to latitudes ±82° (the reference missions acquire data only up to latitudes ±66°) (Mertz & Legeais, 2020). Therefore, gridded SLA values cannot be taken as representative of results for regions north or southwards, more or less, of the Arctic and Antarctic circles, respectively.

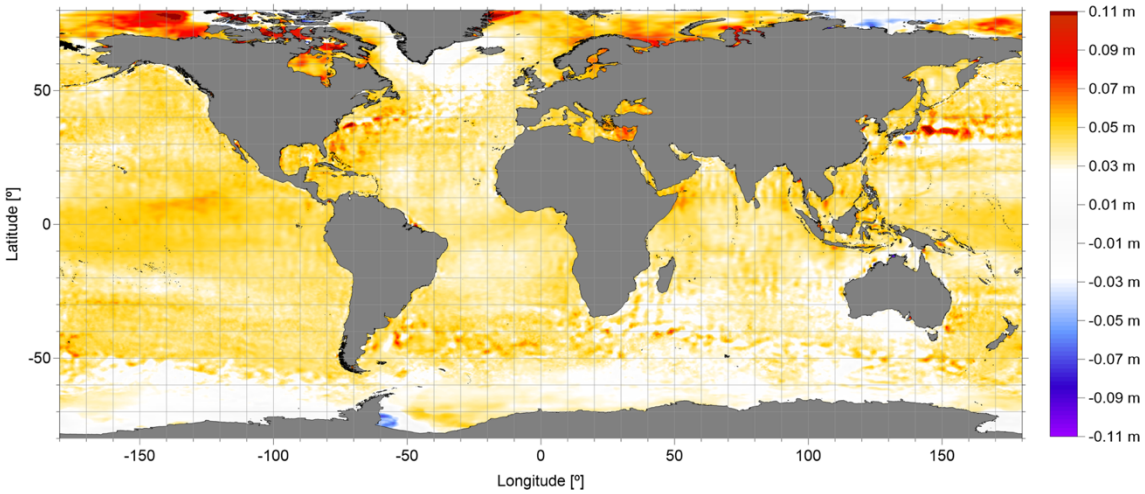

Figure 7 – Mean overall SLA for the period 1993-2020.

The reference period for the gridded SLA products can, however, be corrected to the study period according to the following equations (Pujol et al., 2016).

$$SLA_{1993-2020} = SLA_{1993-2012} - \langle SLA_{1993-2012} \rangle_{1993-2020} \quad \text{Eq. 11}$$

$$MSS_{1993-2020} = MSS_{1993-2012} + \langle SLA_{1993-2012} \rangle_{1993-2020} \quad \text{Eq. 12}$$

$$MDT_{1993-2020} = MDT_{1993-2012} - \langle SLA_{1993-2012} \rangle_{1993-2020} \quad \text{Eq. 13}$$

$$ADT = SLA_{1993-2012} + MDT_{1993-2012} = SLA_{1993-2020} + MDT_{1993-2020} \quad \text{Eq. 14}$$

Where $\langle SLA \rangle_X$ is the temporal mean of the SLA over the period X, MSS is the Mean Sea Surface, MDT is the Mean Dynamic Topography and ADT is the Absolute Dynamic Topography. Therefore, to compute each daily grid corrected for the 28-year SLA mean, $SLA_{1993-2020}$ (left-hand side of Eq. 11), the mean of all the SLA daily grids provided by C3S during the 28-year period, $\langle SLA_{1993-2012} \rangle_{1993-2020}$, referred to an MSS computed for the 1993-2012 period, $\langle SLA_{1993-2012} \rangle$, was subtracted from each daily grid provided by C3S, $SLA_{1993-2012}$.

The absolute geostrophic velocities (zonal component – *u* and meridional component – *v*) are computed from the ADT, using equations 5 and 6 in section 1.1. Since the ADT is obtained by combining SLA and MDT over the same reference period, independently of what period is used, there is no need to change the reference period for these variables and, therefore, the values used in this study were those directly downloaded from the C3S webpage.

As for the SLA data, the 28-year correction was applied according to equation 11, and the geostrophic velocity anomalies (zonal component – *u'* and meridional component – *v'*), as well as the eddy kinetic energy (EKE) per unit mass, were computed according to equations 8, 9 and 10 in section 1.1.

The SLA partial derivatives were computed using a nine-point stencil width (number of grid points used to estimate the finite difference approximation to the derivative) methodology, according to the following equation (Arbic et al., 2012)

$$\frac{\partial \zeta\prime}{\partial \varphi} = \frac{-3\zeta\prime(r+4h)+32\zeta\prime(r+3h)-168\zeta\prime(r+2h)+672\zeta\prime(r+h)-672\zeta\prime(r-h)+168\zeta\prime(r-2h)-32\zeta\prime(r-3h)+3\zeta\prime(r-4h)}{840h}$$

Eq. 15

where ζ' is the SLA, r is the location for which SLA is being computed, and h is the grid spacing.

Earth's gravity varies with latitude due to its oblateness and spin, so a correction according to the following equation was applied (Vajda et al., 2005).

$$g = g_e \frac{1+ksin^2\varphi}{\sqrt{1-e^2sin^2\varphi}} \quad \text{Eq. 16}$$

$$k = \frac{bg_p}{ag_e} \quad \text{Eq. 17}$$

$$e^2 = \frac{a^2-b^2}{a^2} \quad \text{Eq. 18}$$

where g is the normal gravity, g_e is the normal gravity at the equator, g_p is the normal gravity at the pole, k is the normal gravity constant, e^2 is the square of the first eccentricity, a and *b* are the Earth's semi-major and semi-minor axis, respectively.

Because the Earth is shaped as an ellipsoid, its radius changes with latitude, and therefore a correction was also applied to this variable according to the following equation (Torge & Müller, 2012).

$$R = \sqrt{M(\varphi)N(\varphi)} \quad \text{Eq. 19}$$

$$M = \frac{a(1-e^2)}{(1-e^2sin^2\varphi)^{\frac{3}{2}}} \quad \text{Eq. 20}$$

$$N = \frac{a}{\sqrt{1-e^2sin^2\varphi}} \quad \text{Eq. 21}$$

where R is the Earth Radius, M is the meridian radius of curvature, and N is the radius of curvature in the prime vertical.

Along the latitudes near the equator, the Coriolis parameter tends to zero, $f \to 0$, the flow becomes independent of the sea level gradient, which may exist as a result of ageostrophic balances and, therefore, the f-plane formulation is no longer applicable (Lagerloef et al., 1999). Around latitudes 2-3°, a transition from the f-plane to a β-plane geostrophic approximation, which involves a second derivative of the surface height, should be considered (Lagerloef et al., 1999). So, around the 3°N-3°S latitude band, because the constant term of the Coriolis force tends to zero, the so-called equatorial β-plane takes place and the f-plane approximation cannot be adopted. However, since the study area under analysis does not include this band's latitudes, the f-plane approximation, where only the constant term of the Coriolis force is considered. ($f \cong f_0$), was used and all the results between latitudes 3°N and 3°S were excluded from the subsequent analysis.

The difference between *u'* and *v'* velocities calculated in this study, without the 28-year correction, and those made available by C3S is presented in Figure 8 and Figure 9, respectively, for one random day selected from the total period of analysis (28 years). The differences in *u'* and *v'* are zero, meaning that the calculated geostrophic velocity anomalies very well agree with the ones provided by C3S. On the other hand, Figure 10 and Figure 11 show the results for the same difference but now the geostrophic velocity anomalies were calculated using corrected SLA values, i.e. SLA values obtained after removing the 28-year SLA mean. Results are no longer exactly zero, even though they are all very close to zero. This is due to the shift in the SLA values introduced by the SLA correction for the reference period.

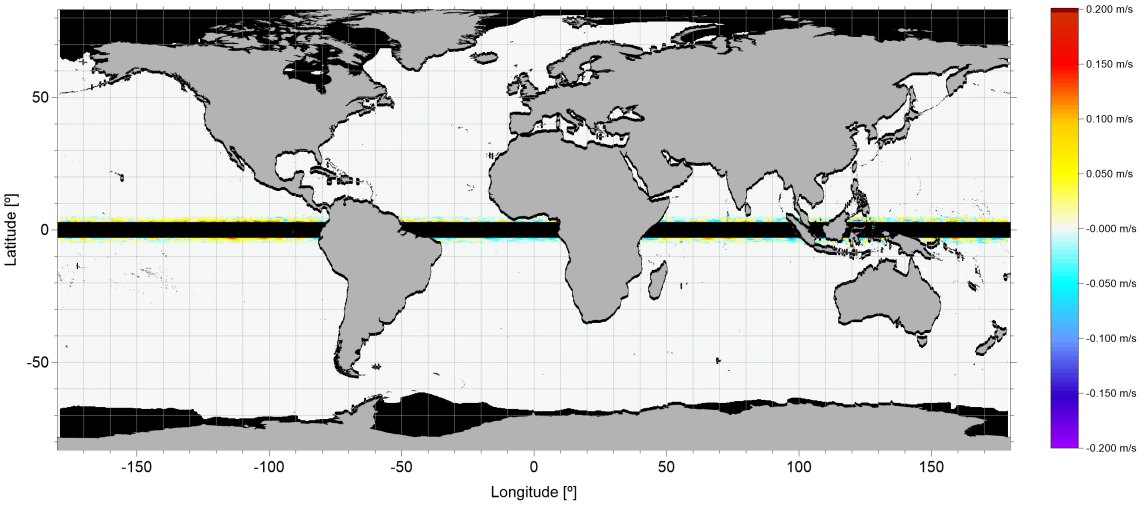

Figure 8 – Difference between geostrophic velocity anomalies (zonal component, u') without the 28-year mean SLA correction and the correspondent geostrophic velocity anomalies made available by C3S, for the date 06/05/2015. The 3°S-3°N latitude has been set to "no data" value.

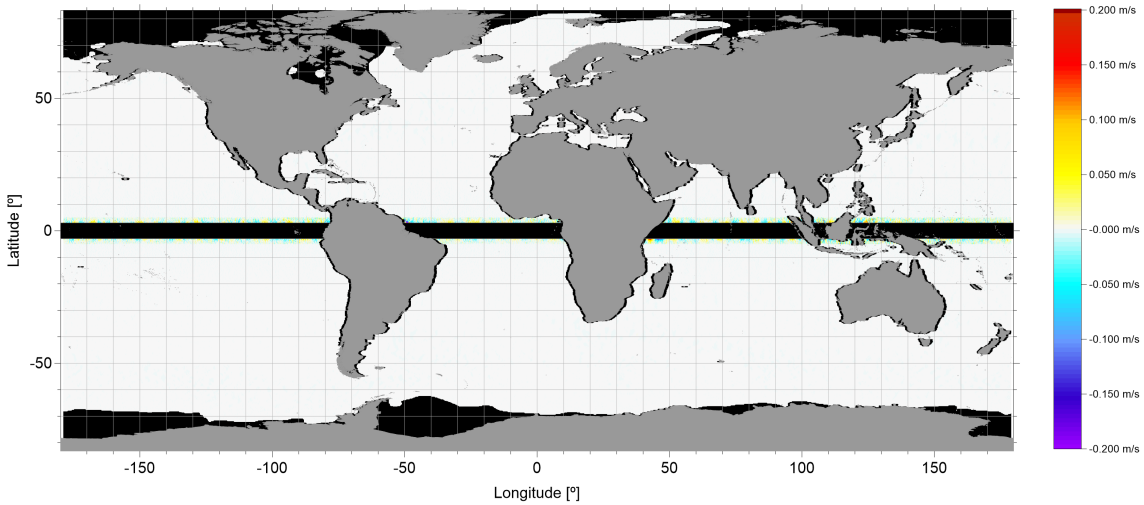

Figure 9 – Difference between geostrophic velocity anomalies (meridional component, v') without the 28-year mean SLA correction and the correspondent geostrophic velocity anomalies made available by C3S, for the date 06/05/2015. The 3°S-3°N latitude has been set to "no data" value.

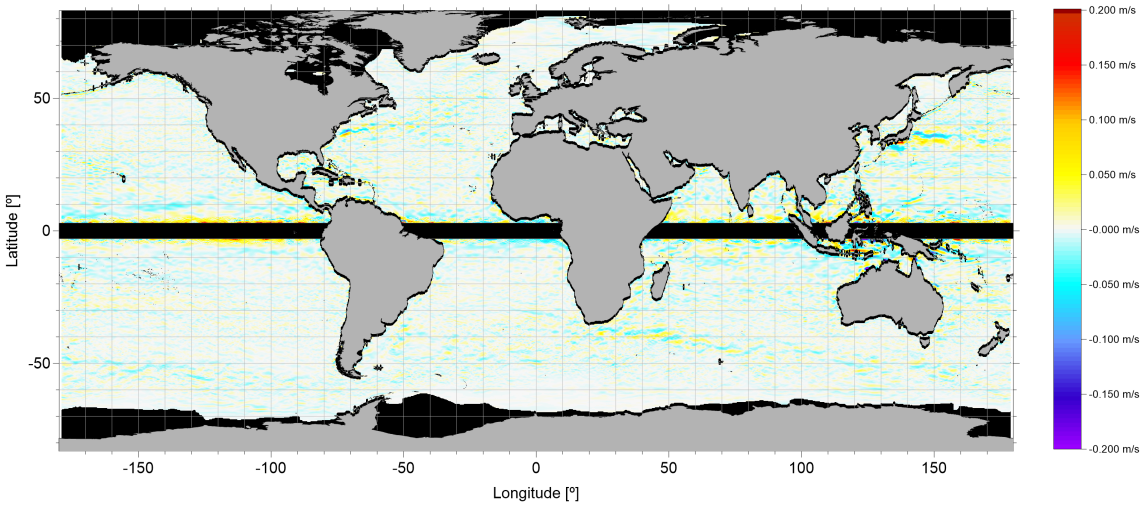

Figure 10 – Difference between geostrophic velocity anomalies (zonal component, u') including the 28-year mean SLA correction and the correspondent geostrophic velocity anomalies made available by C3S, for the date 06/05/2015. The 3°S-3°N latitude has been set to "no data" value.

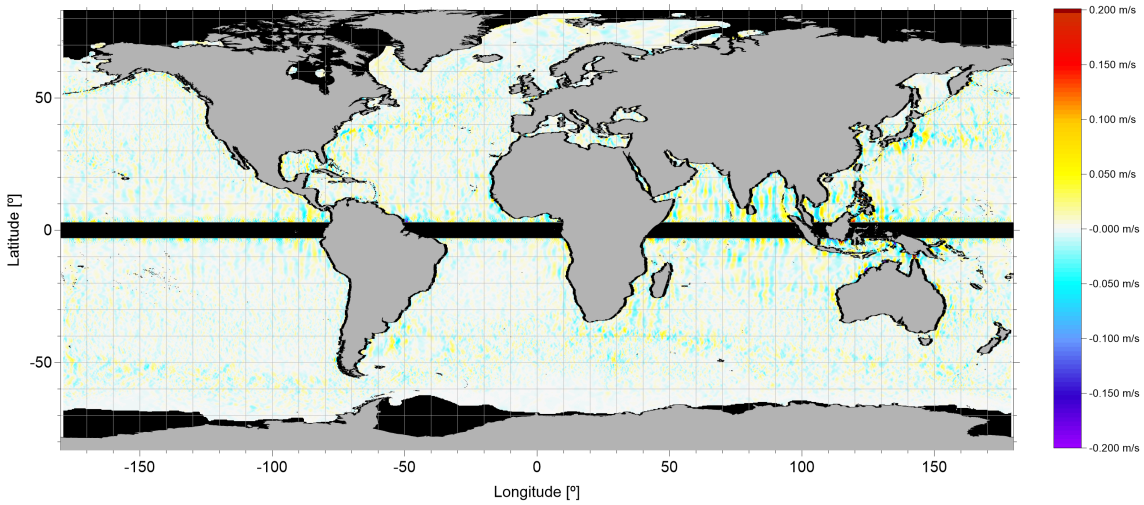

Figure 11 – Difference between geostrophic velocity anomalies (meridional component, v') including the 28-year mean SLA correction and the correspondent geostrophic velocity anomalies made available by C3S, for the date 06/05/2015. The 3°S-3°N latitude has been set to "no data" value.

Similar results were attained for other random dates during the period of analysis (not shown), confirming the validity of the methodology for the calculation of the geostrophic velocity anomalies.

2.3.2 SLA, EKE, and magnitude fields characterization

EKE was computed using the f-plane methodology as described earlier. No data pixels at high latitudes and adjacent to land areas are a consequence of the nine-point stencil width methodology used in the computation.

The root mean square (rms) for each of these variables was calculated to determine their average magnitude, using the following equation.

$$x_{rms} = \sqrt{\frac{1}{n}\left(\sum_{i=1}^{n} x_i^2\right)} \qquad \text{Eq. 22}$$

where, for each pixel in the SLA, EKE, or magnitude grids, x_i is the data value, and n is the number of values.

The dispersion of each variable with respect to its mean is determined by the variance, using the following equation.

$$var = \frac{\sum_{i=1}^{n}(x_i - \bar{x})^2}{n-1} \qquad \text{Eq. 23}$$

where, for each pixel in the SLA, EKE, or magnitude grids, $\bar{x}$ is the mean of all the values.

In the calculation of the time series for the different oceanographic fields, data for the 29th of February were systematically excluded so that each year would consider exactly 365 days. The time series were obtained by averaging, for each daily grid, the field under study, after weighting the pixel values by the cosine of the latitude. The signals of interest in the generated time series are the annual, interannual, and linear trend. Since the interannual signal was computed using a two-sided moving average of length of 367 days to exclude signals with a period inferior to one year, the first and the last 183 data elements were removed to avoid the distortion of the linear trend, which has been fitted from the interannual signal. After detrending the signal, a stable seasonal filter was applied to extract the annual signal. Since the data is daily with periodicity 365, the same number of indices were created, each corresponding to each day's observations. The average of each index was put back into a vector and the seasonal estimate was centred to fluctuate around zero. Finally, the residual signal was computed by subtracting the annual and the interannual from the original time series.

A similar approach was used to compute the variance decomposition maps, by applying this methodology to each pixel in the variance map. In this way, it was

possible to geographically discriminate the annual, interannual and residual contribution to the total variance for each variable.

The regional change maps represent the linear trend value computed at each pixel considering the period between 1993 and 2020. This means that, for each grid (SLA, EKE, or magnitude) pixel, the time series was calculated, the linear trend was adjusted to the respective interannual signal and the slope value was saved to be shown in its geographic location.

In the maps of SLA trends (in Figure 14), the Glacial Isostatic Adjustment (GIA) correction was also applied. This correction is related to the Earth's (land and ocean) response to the collapse of the Pleistocene ice sheets from the last glacial cycle about 20.000 years ago, still ongoing (Tamisiea & Mitrovica, 2011). The two grids, "relative sea level (tide gauge) prediction" and "vertical land motion (GPS or GNSS) prediction" were downloaded from the National Oceanographic Centre – Permanent Service for Mean Sea Level webpage[11]. Because satellite signals are measured relative to the centre of mass of the planet and not relative to the surface of the solid earth, the GIA correction applied to the SLA trend map was the sum of the two downloaded grids (Peltier, 2001). These grids are supplied on a 1°x1° spatial resolution and, therefore, a bilinear interpolation was applied to convert them to 0.25°x0.25° resolution grids. This way, their sum could be subtracted from the calculated SLA trend map.

To compute the global characterization maps of regional change and variance, a subsampling of one measurement every ten was chosen, to avoid computing limitations.

2.3.3 Correlation maps

Correlation maps between each selected climate index and SLA were computed for the study area, to investigate whether there is a correlation between them and the geographical distribution of these correlations. The methodology to calculate these correlations was the same used by Iglesias et al. (2017), where the linear association between each CI and SLA at each grid point (0.25°x0.25° grid pixel) was calculated using a Pearson correlation coefficient. A statistical Student's t-test was used to determine the significance coefficient of ± 0.318 to achieve a confidence interval of at least 95%. All the time series were previously detrended and normalized using the

[11] https://www.psmsl.org/train_and_info/geo_signals/gia/peltier/index.php).

'zscore' method (centres the data to have mean 0 and scales it to have standard deviation (s.d.) 1).

The analysis was based on seasonal mean values of SLA at each grid point and each CI, calculated from the corresponding monthly time series and considering winter (wtr) as the period of December, January and February, spring (spr) as March, April and May, summer (sum) as June, July and August, and autumn (aut) as September, October and November. Similar correlation maps were also computed between each CI and EKE as well as between each CI and magnitude. However, no significant results were found and therefore those results were excluded from this report.

For each season where a significant correlation between SLA and the CI was found, results are presented and compared with the mean EKE and surface geostrophic currents, considering their values in the seasons when each index was significantly positive and negative. Positive correlations identify the simultaneous increase or decrease of both variables, and negative correlations identify opposite movements of the two variables.

3. Results and discussion

3.1 Global characterization of the oceanographic fields

Several statistical parameters, including the root mean square (rms) and variance were computed to spatially characterize, in global terms, the behaviour of the SLA, EKE and magnitude of surface geostrophic currents during the 28-year period. Time series for the same oceanographic fields were computed and analysed to investigate their temporal variability. The main objective of these global analyses was to validate the methodology adopted in this study by comparing the obtained results with those from previous studies. For EKE field, however, the presented results, especially those showing the regional EKE change, are hardly found in the published literature. Martínez-Moreno et al. (2021) included an EKE trend analysis but used a different methodology and different individual regions that limited the comparison of the authors' results with those of this study.

3.1.1 SLA

Results for the rms and variance of SLA are shown in Figure 12 and Figure 13, respectively. The rms is a measure of the expected magnitude of the oceanographic field, while the variance provides information about the variability of the field over time. Therefore, regions with high variance values are more unstable and energetic than regions of low variance values. Regions with close to zero variance values present a steady or quasi-steady state of the ocean, where the variables defining the behaviour of the system are unchanging in time.

The highest values of both statistical parameters (rms around 0.40 to 0.50 m and variance above 0.050 m^2) occur in areas associated with the strongest oceanic currents, as expected, particularly along the Gulf stream, the Brazil-Malvinas confluence, the confluence of the Agulhas, Mozambique and the Antarctic Circumpolar currents, at the south and east of the African continent and along the Kuroshio current in the Pacific Ocean, near the coast of Japan. The lowest rms values (below 0.05 m) are located mainly in the South Atlantic Ocean and in the Southeastern Pacific Ocean. Associated with these low rms values, also the variance values in these areas are zero, or very close to zero, therefore describing quasi steady-states regions. In the North Pacific and North Atlantic gyres, although significant SLA rms values can be found, the variance values are also very low (below 0.005 m^2), characterizing very low energy

areas. On the other hand, the significant rms values and high variances presented in the Indian Ocean gyre area, are in agreement with an unstable and highly energetic region.

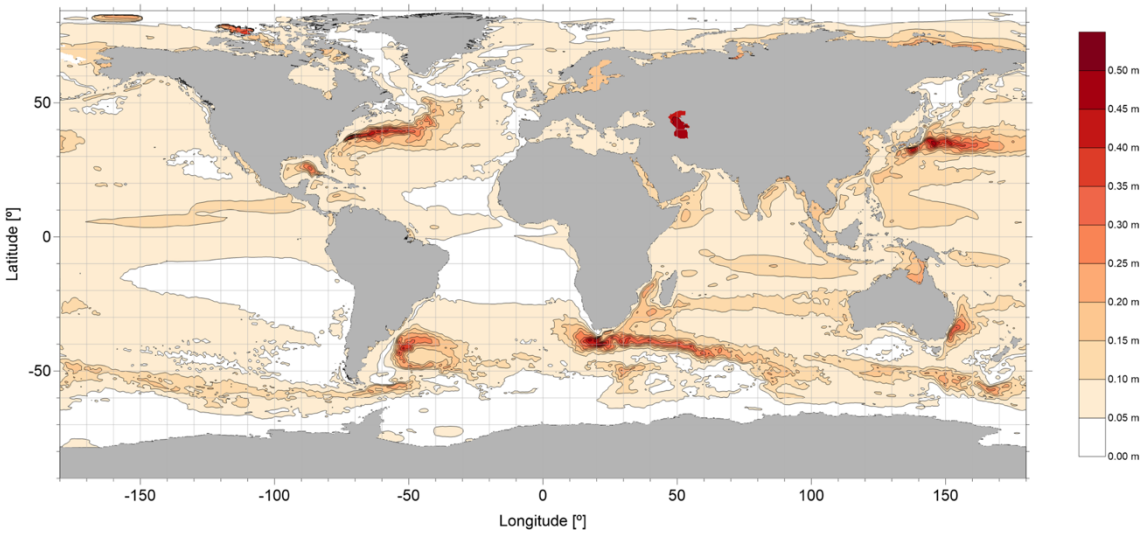

Figure 12 – SLA rms (m) over the 28-year period.

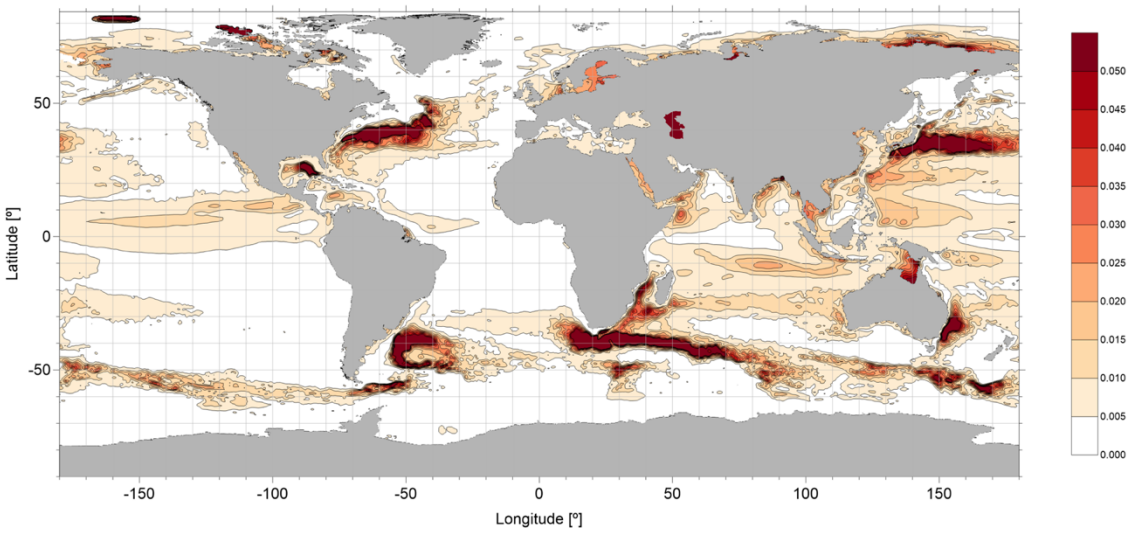

Figure 13 – SLA variance (m^2) over the 28-year period.

The global SLA trend map is presented in Figure 14. The result seems to be in good agreement with those published by the University of Colorado Sea Level Research Group[12] and by the Centre National d'Etudes Spatiales (CNES) Aviso+ Satellite Altimetry Data[13], with mostly positive trend values that can reach up to 7-8 mm/y. The highest values can be observed along the western boundary currents in the Atlantic Ocean, Indian Ocean, the north and southwestern Pacific Ocean, and in the Southern

[12] https://sealevel.colorado.edu/data/sea-level-trends-satellite-altimeters
[13] https://www.aviso.altimetry.fr/en/data/products/ocean-indicators-products/mean-sea-level.html#c15717

Ocean, also known as the Antarctic Ocean. Some minor and localized regions present negative trend values, mostly on higher latitudes, precisely where land uplift occurs.

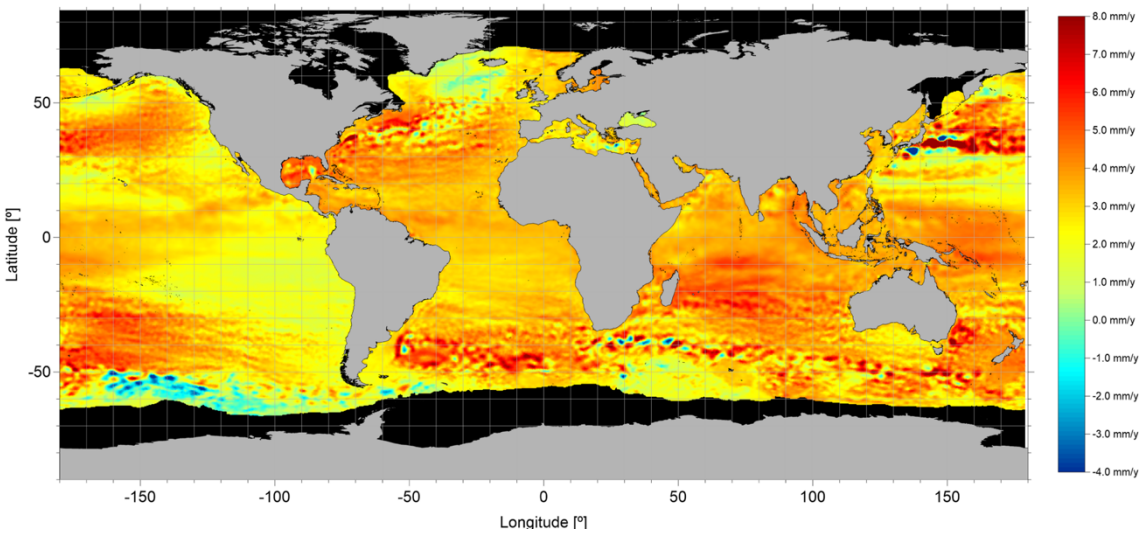

Figure 14 – Regional SLA change: slope (mm/year) of the linear trend for the 28-year period. Computation includes GIA correction.

The SLA global mean time series (shown in Figure 15a by the blue solid line) demonstrates that the mean sea level is rising. The slope of the linear fit to the interannual signal (black line in Figure 15a) provides us with a rising rate value of 3.15 mm/y. After considering the mean global value of 0.3 mm/y for the GIA correction (Peltier, 2001), the result becomes 3.45 mm/y, in good agreement with the current published data, namely the 3.4 mm/y derived by C3S (Legeais, 2021), 3.53 mm/y derived by CNES[14] and 3.3 mm/y derived by the University of Colorado Sea Level Research Group[15]. The dashed blue line shown in the 1993-1998 period (tpa corrected) represents the estimation of the SLA after applying the empirical correction for the TOPEX-A instrumental drift as made available by C3S. If considered, this correction would reduce the rate of the global mean sea level rise (from 3.45 to 3.24 mm/y) and change the fit from linear to quadratic (Legeais, 2021). However, given the lack of consensus on the best approach to estimate this correction, and the recommendation to wait for a future release of a reprocessed TOPEX dataset (Taburet et al., 2021), this correction will not be considered in the subsequent analysis.

The annual signal can be clearly identified in the time series (blue line in Figure 15a) which is supported by the corresponding Power Spectral Density (PSD), estimated using the periodogram (Figure 15b), and is the strongest signal present in the time

[14] https://www.aviso.altimetry.fr/en/data/products/ocean-indicators-products/mean-sea-level.html#c15717
[15] https://sealevel.colorado.edu/data/2021rel2

series. The PSD computed for a specific interval of frequencies indicates the strength of the variations in that frequency range, allowing the identification of at which frequencies the variations are strong or weak (Cygnus Team, 2015). In this plot, a second periodic signal with a 6-month period, with significance for the analysis, can also be seen (Figure 15b). The 1997/98 and 2015/16 time series peaks are coincident with the occurrence of the two strongest El Niño events after 1993. The inverted peak in 2010/11 is in agreement with the development of a strong La Niña event (Null, 2022). These stronger peaks are also visible in the interannual signal (red line in Figure 15a).

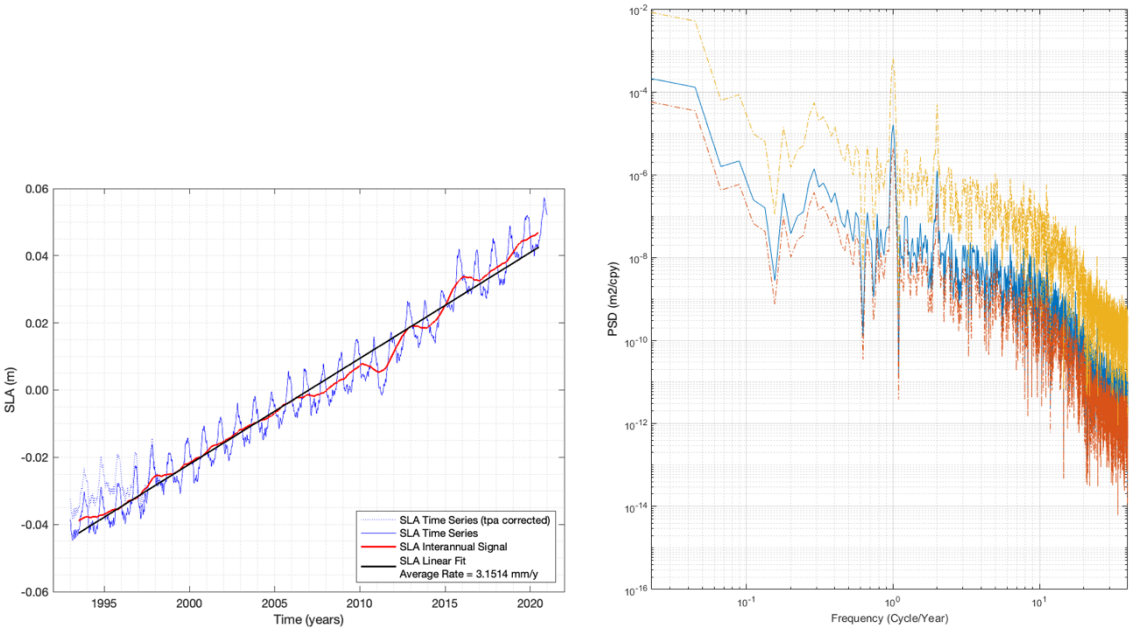

a) b)

Figure 15 – a) Time series of the global mean of SLA (1993-2020). b) PSD computed for the global mean SLA signal (in blue). Red and yellow lines in the PSD identify the lower and upper 95% confidence interval limits, respectively.

3.1.2 EKE

Results for the EKE rms and variance are presented in Figure 16 and Figure 17, respectively. As would be expected, eddy-rich regions are clearly identifiable in the vicinity of the major current systems such as the Gulf Stream, Agulhas, and Mozambique currents along the eastern African coast, the Kuroshio Current along the coast of Japan, the Antarctic Circumpolar Current and at the Brazil-Malvinas confluence zone. EKE rms values in these regions can reach up to 5000 cm^2/s^2 and variance exceeds 500 $(cm^2/s^2)^2$. Latitudes between 3°N and 3°S were excluded from the maps and therefore the equatorial currents are not evident. However, higher rms values shown in Figure 16 along the latitude bands 3°N-10°N and 5°S-3°S, both on the Pacific and Atlantic oceans, are most likely associated with these currents.

Figure 18 and Figure 19 show the same EKE rms and variance fields but with a saturated colour scale for the higher energy areas so that the lower energy regions could be analysed. The southern Atlantic between the Equator and approximately 30°S and the south Pacific up until around 140°W present the lower energy levels, with rms below 25 cm^2/s^2, unlike the Indian ocean where eddies extend all the way from eastern Africa to Australia, showing rms values above 350 cm^2/s^2. In the north Atlantic, the energy levels are also generally low, below 50 cm^2/s^2, in the latitudes south of 30°N, except around the Canary and Cape Verde archipelagos and also on the western African coast, where eddy-rich spots can be identified. In the Pacific and Atlantic oceans gyres, both on the northern and southern hemispheres, although the rms values may by significant in some areas, the null variances indicate that these are very low energy regions.

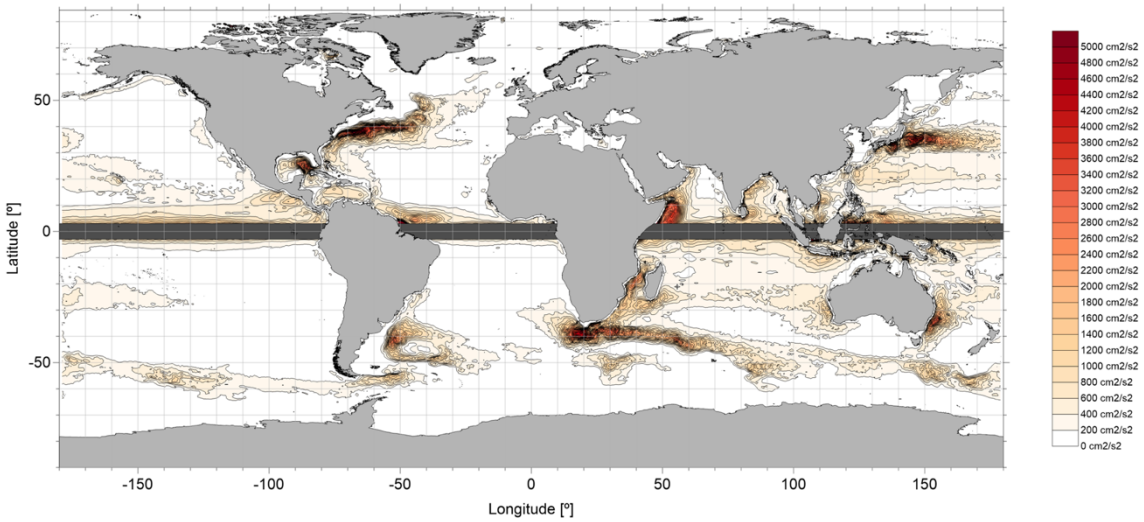

Figure 16 – EKE rms (cm^2/s^2) over the 28-year period.

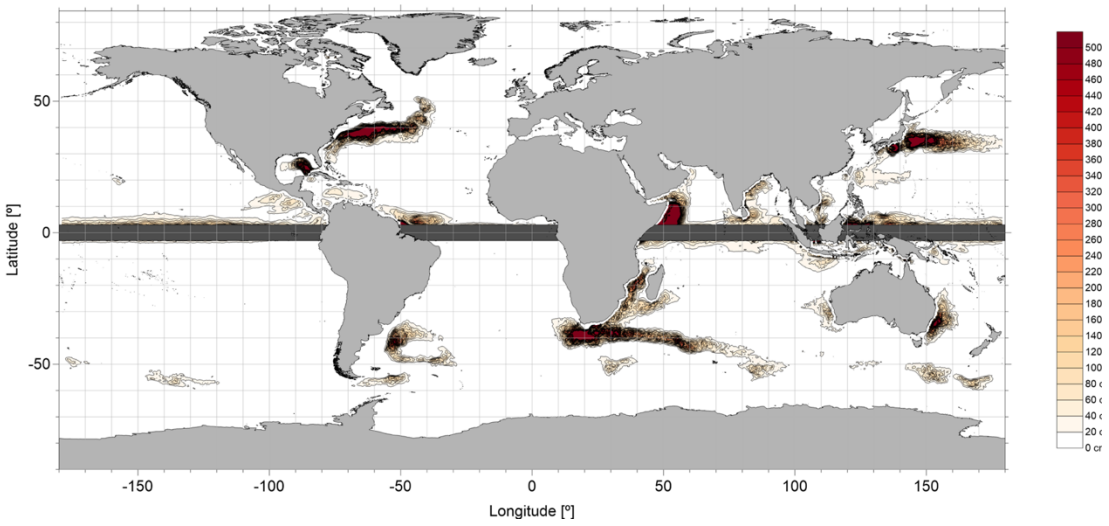

Figure 17 – EKE variance ((cm²/s²)²) over the 28-year period.

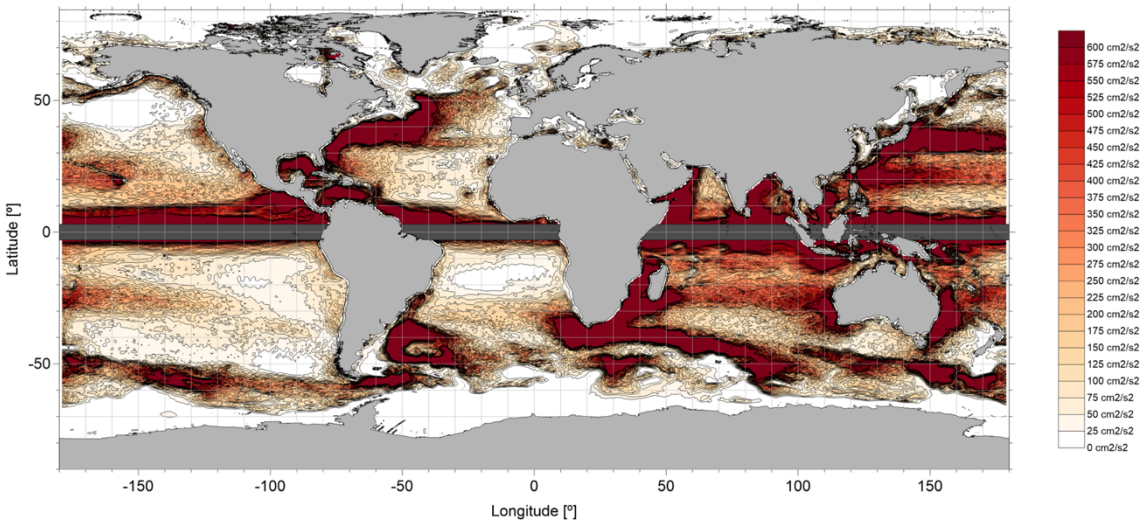

Figure 18 – EKE rms (cm²/s²) over the 28-year period with a saturated colour scale.

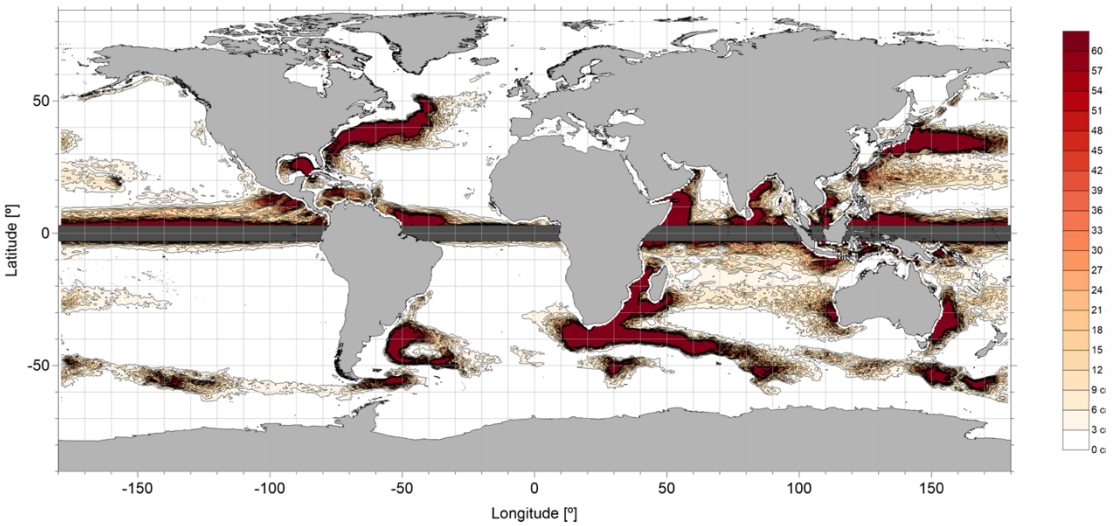

Figure 19 – EKE variance ((cm²/s²)²) over the 28-year period with a saturated colour scale.

The regional EKE change can be analysed by computing the slope of the linear trend, fitted to the interannual signal of the EKE time series for each pixel, and plotting this value geographically. The regional EKE change map is shown in Figure 20. Patterns with opposite increasing (red colours) and decreasing (blue colours) trends are clearly observed, mainly over the eddy richer regions previously identified in the rms and variance maps (Figure 16 to Figure 19). The western Pacific Ocean seems to concentrate the larger areas with the more extreme trend values while in the Indian Ocean, although an eddy-rich region was previously noted, the trends are smaller.

One of the regions with the stronger trends is the Gulf Stream Current area, where the EKE trend is highly positive (up to 8.0 (cm^2/s^2)/year) close to the North American coast and then becomes highly negative (up to -8.0 (cm^2/s^2)/year), in the area where the current moves away from the continental region, around 50°W. The same phenomena seem to occur in the Azores Current region but with lower trend values. Similar results are shown in the Agulhas Current region, with high trend values, but the negative values are then eliminated, around 30°S, by the highly positive trend associated with the Mozambique Current. In the Kuroshio Current region, the results appear to be more complex. The trend values start highly positive and also turn to highly negative until they reach the North Pacific Current region, around 150°W, when they turn back to highly positive along latitude 40°N but stay highly negative along latitude 30°N, forming a zonal pattern. This behaviour may induce that changes have been occurring in the mesoscale EKE signals surrounding the major oceanic currents and should be further investigated. Another interesting feature that should be explored is the opposite positive and negative twin trend bands around latitudes 30°S and 20°S in the middle of the South Pacific Gyre.

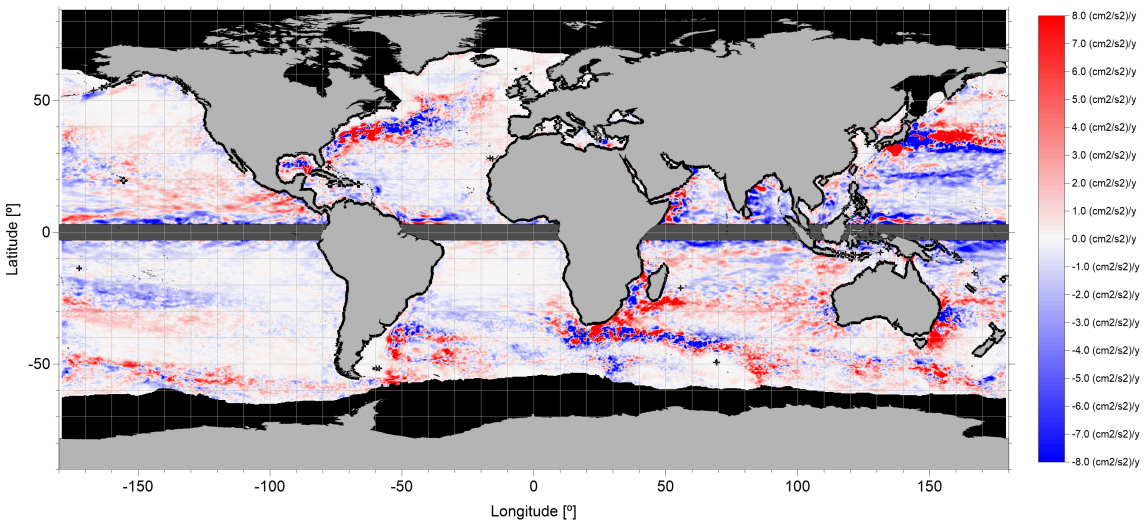

Figure 20 – Regional EKE change: slope (cm^2/s^2/year) of the linear trend for the 28-year period.

The global mean EKE time series (blue line in Figure 21a) shows a positive linear trend (black line Figure 21a) of 0.0064 cm^2/s^2/year (the linear trend was adjusted to the interannual signal – red line in Figure 21a). Maximum values occur simultaneously with El Niño events, being noteworthy the 1997/98 and the 2015/16 peaks with the highest eddy-energy values (above 220 cm^2/s^2). Minimum values, on the other hand, are synchronized with La Niña events, most of them immediately preceding El Niño events (ex.: 1995/96, 2002, 2009). A single significant seasonality (annual signal) is identified in the PSD estimated using the periodogram (blue line in Figure 21b).

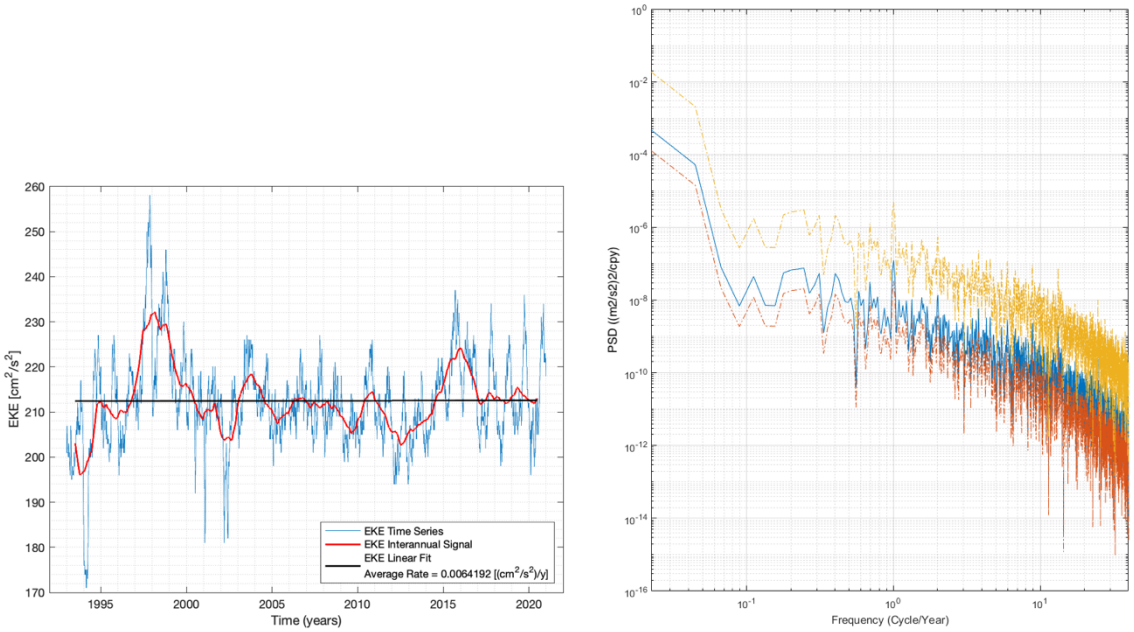

a) b)

Figure 21 – a) Time series of the global mean of EKE (1993-2020). b) PSD computed for the global mean EKE signal (in blue). Red and yellow lines in the PSD identify the lower and upper 95% confidence interval limits, respectively.

3.1.3 Magnitude of the surface geostrophic currents

Figure 22 and Figure 23 present the rms and variance results for the magnitude of the surface geostrophic currents, respectively. As would be expected, the highest rms values (above 0.90 m/s) follow the main global currents allowing us to identify the major current systems. The lesser dynamic areas are again in the subtropical basins of the Atlantic and Pacific oceans, with rms values lower than 0.10 m/s. In the same way as in the previous SLA and EKE analysis, the null variances in the Pacific and Atlantic gyres areas, although rms values may not always be disregarded, are an indication of quasi-steady-state regions. The higher variance values in the Indian Ocean gyre show evidence of a more unstable and highly energetic region.

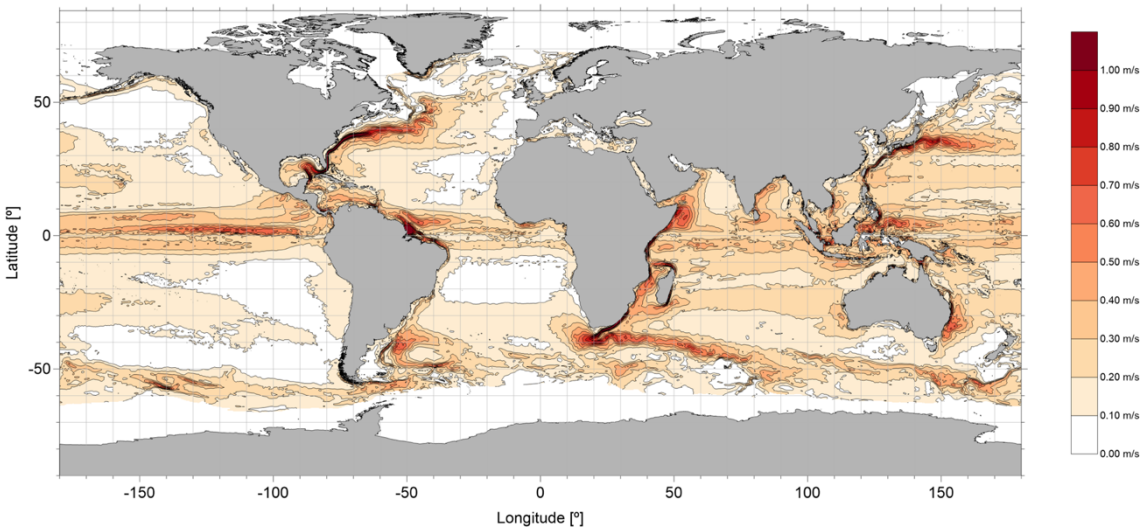

Figure 22 – Rms (m/s) of the magnitude of the surface geostrophic currents for the 28-year period.

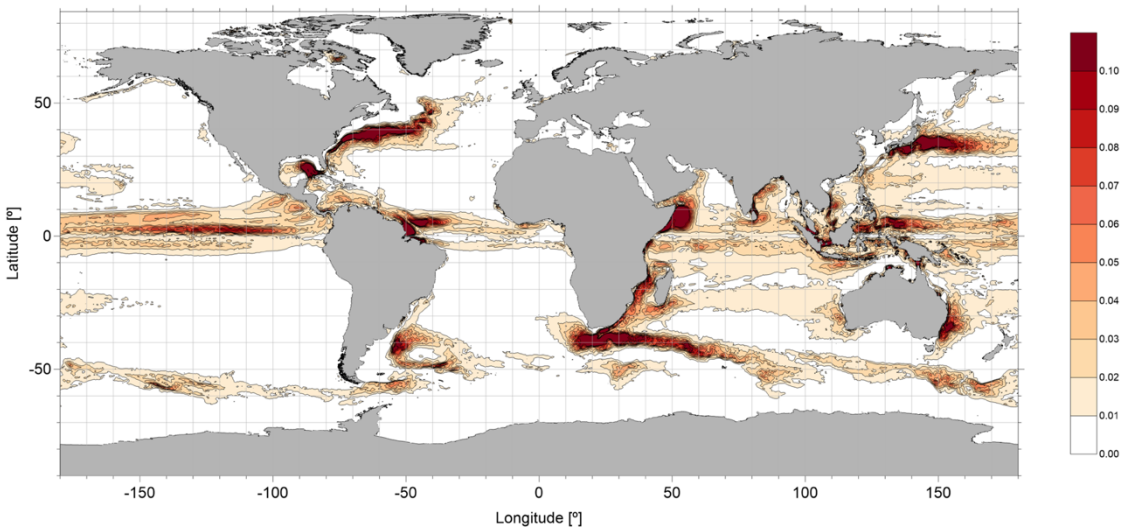

Figure 23 – Variance (m^2/s^2) of the magnitude of the surface geostrophic currents for the 28-year period).

Opposite increasing and decreasing patterns in the regional change map are scattered all over the oceans (Figure 24) but with higher definition and intensity in the confluence of different ocean currents as in the southern Pacific, Atlantic, and Indian Oceans, the Northern Atlantic, the equatorial band, and north of the Kuroshio Current. In the Gulf Stream Current region, a similar effect as in EKE, of a high positive trend near the coast and a high negative trend in the Atlantic area, seems to be occurring. The same similarity to the EKE trend map can also be seen in the Agulhas and Kuroshio currents regions. In the South Pacific Gyre, the zonal positive and negative trend bands are also visible, but the relative values seem to be more significant than in the EKE trend map.

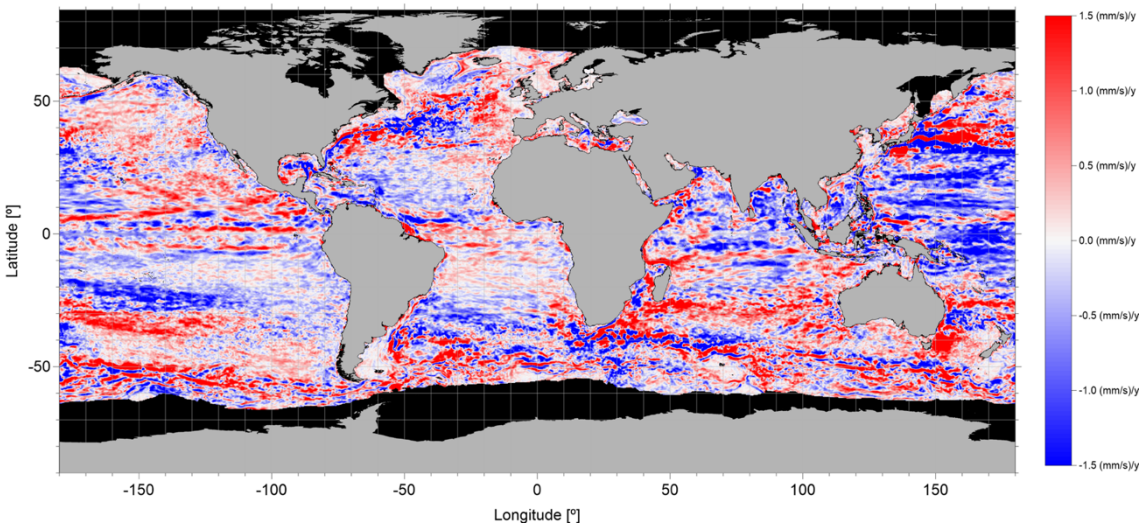

Figure 24 – Regional change of the magnitude of the surface geostrophic currents: slope (m/s/year) of the linear trend for the 28-year period.

The mean global trend of the magnitude of the surface geostrophic currents is positive (Figure 25a) and equal to 3.0×10^{-5} m/s/year. The maximum values of the time series generally coincide with El Niño years. A significant peak in the PSD shows the existence of an annual signal in the variable (Figure 25).

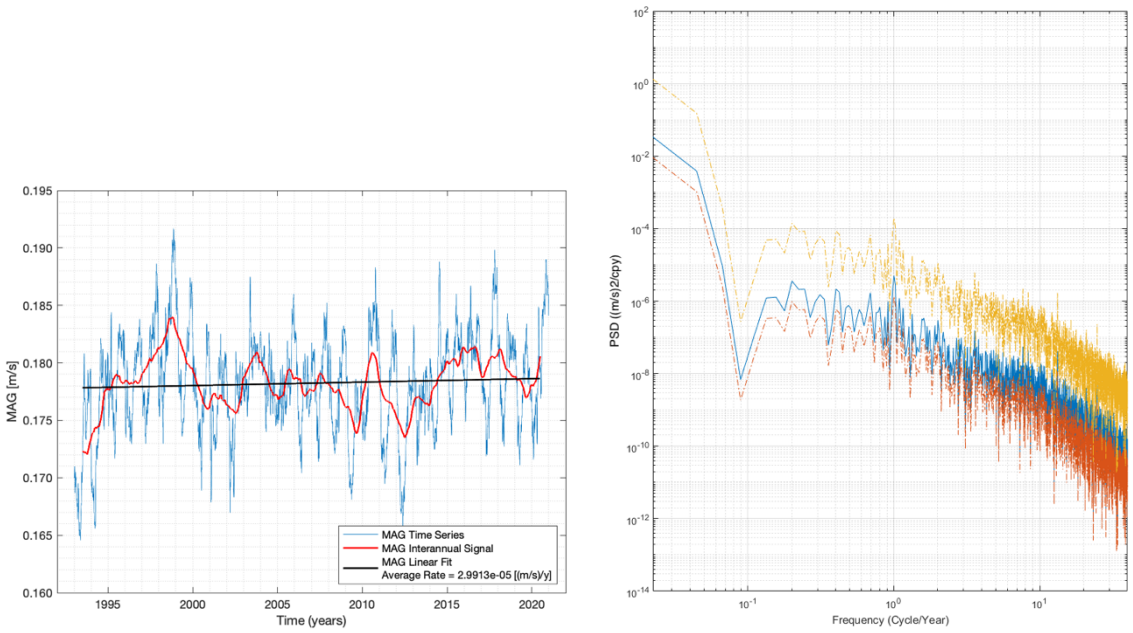

a) b)

Figure 25 – a) Time series of the global mean of the magnitude of the surface geostrophic currents (1993-2020). b) PSD computed for the global mean magnitude of the surface geostrophic currents signal (in blue). Red and yellow lines in the PSD identify the lower and upper 95% confidence interval limits, respectively.

3.2 Characterization of the oceanographic fields in the study region

The previous global SLA, EKE, and magnitude characterization allowed us to take a general view of these oceanographic fields and assess the processing methodology by comparison with previously published data. The results seem to agree with what would be expected given the current knowledge regarding the global oceans' dynamics and climatic events (ex.: El Niño events) occurring during the study period 1993-2020. Henceforward, the focus will be on the chosen study region located in the ETAO region around the Cape Verde Archipelago, defined by latitudes and longitudes 3° to 30°N and 40°W to 0°, respectively

Similarly to what has been adopted in the global analysis, the TOPEX-A instrumental drift correction has not been considered in the calculations due to the lack of knowledge concerning the instrumental drift regional variation, the lack of consensus on the best approach to estimate this correction, and the recommendation to wait for a future release of a reprocessed TOPEX dataset (Taburet et al., 2021).

3.2.1 SLA

The highest SLA rms (Figure 26a) and variance (Figure 26b) values, reaching up to 10 cm and 1 cm^2, respectively, are located in the southwest region of the study area, particularly south of 10ºN. This area is coincident with the NECC's influence region. SLA rms values of around 6 to 8 cm and variances of 0.4 to 0.6 cm^2 can also be found along the African coast in areas characterized by strong upwelling. In the top left area of the study region, the higher rms and variance values of 7 cm and 0.5 cm^2, respectively, may be associated with the influence of the Azores Current.

The decomposition maps depicted in Figure 27 show that in the NECC's influence area and on the African coast, where the upwelling is relevant, the SLA annual signal has a contribution above 50% to the total SLA variance. Also, the residual signal has a contribution that can go up to 40-45% south of 10°N and west of 35°W, leaving the interannual component as the one with the lowest contribution, in the NECC's influence area. In the Cape Verde region and westwards, the SLA interannual component prevails with a contribution above 45%, followed by the residual signal, adding up to 35%. The annual component shows a negligible contribution to this region. In the overall study area, the contribution of the residual component for the total SLA variance is, therefore, the lesser relevant, except in some limited areas between 5°-10°N and

35°W and southwest of the Cape Verde archipelago due to the confluence of the northward branch of the NECC that flows along the African coast, i.e. the Mauritanian Current, and the NEC, where it can reach up to 40%. The residual component, being associated with signals with higher than 1 cycle per year frequency, shows the regions where large eddies occur, mainly related to the NECC and the NEC confluence regions.

Seasonal means (Figure 28) computed for the study period show opposite SLA mean values in winter and spring when compared to summer and autumn, with the most extreme values occurring during spring and autumn. In spring, when the NECC reaches its minimum, latitudes south of 5°N present the strongest negative mean SLA, up to -10 cm. Highly negative values can also be found along the coast of Mauritania and Senegal, an area characterized by strong seasonal upwelling. Westwards of Cape Verde, between latitudes ~7°N and ~17°N, the SLA mean values are mostly zero or barely positive. During autumn, on the other hand, the mean SLA becomes highly positive (up to 7 cm) in the areas where it was negative during spring. Between ~7°N and ~17°N, westwards of Cape Verde, the mean SLA is now strongly negative (up to -6 cm). Similar opposite patterns are shown in winter and summer, although the absolute values are significantly lower than the ones in spring and autumn, and the central area between ~7°N and ~17°N seems to extend eastwards, closer to land.

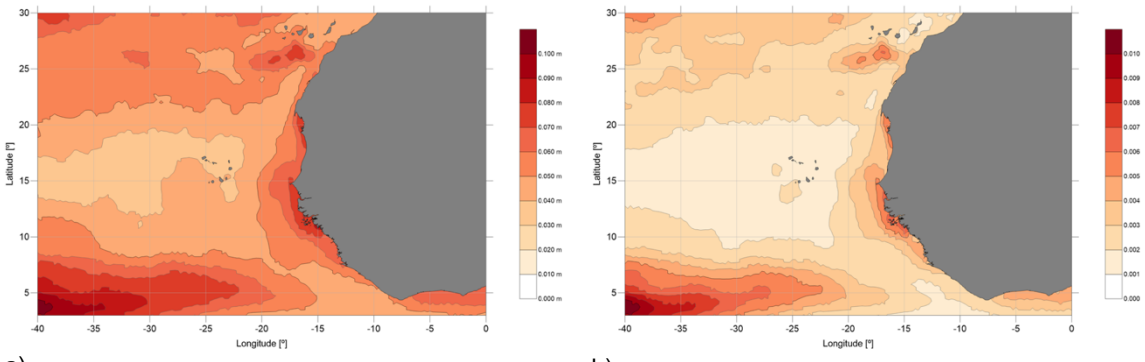

a) b)

Figure 26 – SLA rms (m) (a) and variance (m^2) (b) for the study area over the 28-year period.

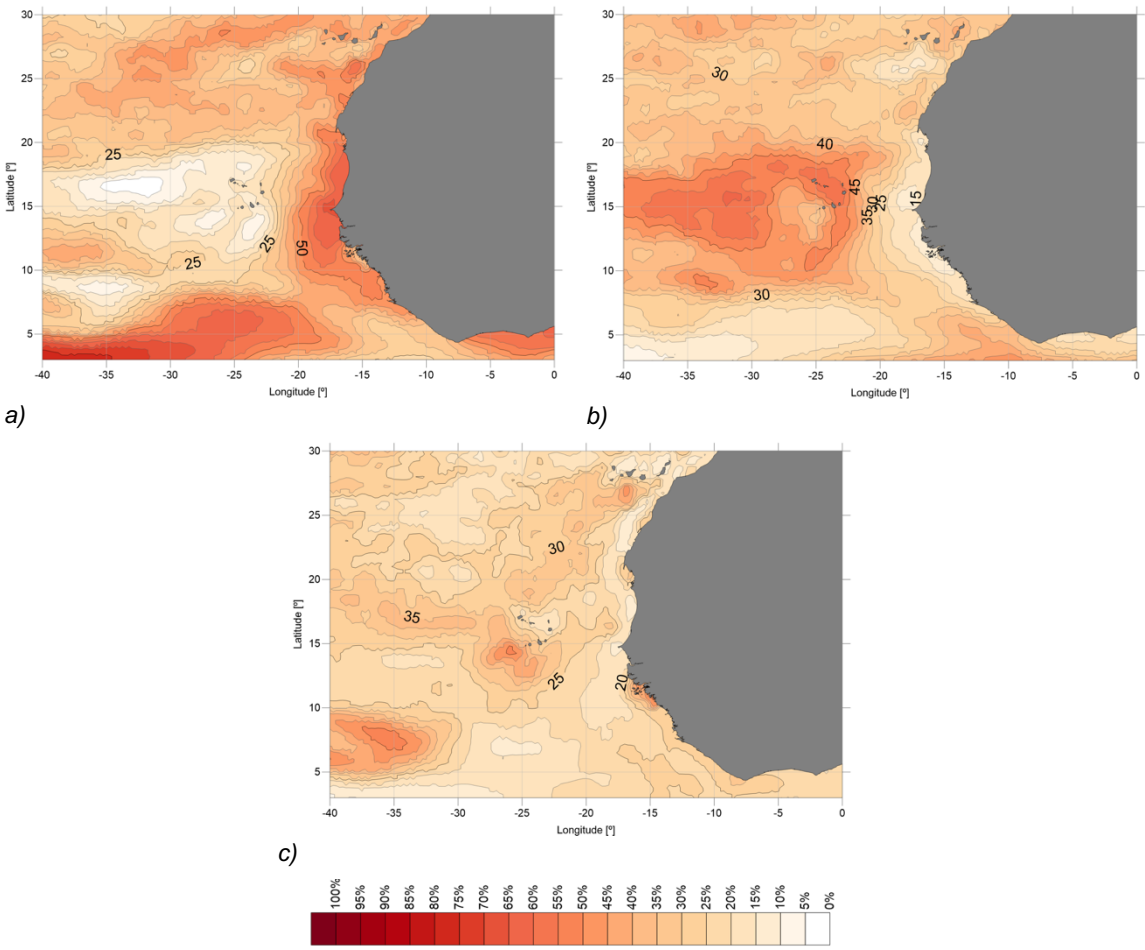

Figure 27 –Contribution of the annual, interannual and residual SLA signals for the total variance in the study region. a) percentage of the annual signal contribution, b) percentage of the interannual signal contribution, c) percentage of the residual signal contribution.

The sea level change is irregular along the study region. Figure 29 shows the slope of the linear trend, computed from the SLA time series, for each pixel. The highest values, reaching up to 5 mm/y, are located in the northeastern area around 28 - 30°N and 40° - 27°W, most certainly associated with the southernmost part of the Azores Current. High values of approximately 3.5 to 4 mm/y also occur below 10°N in the influence area of the NECC, and in the African coastal areas, where the upwelling is a relevant feature. Latitudes between 10°N and 20°N have the lowest sea level rising rates even though still positive, in the range of 2.5 to 3.5 mm/y. However, the SLA time series for the study region (Figure 30) shows that the sea level in the ETAO is rising at a rate of 3.25 mm/y, higher than the global average of 3.15 mm/y (not including the GIA correction).

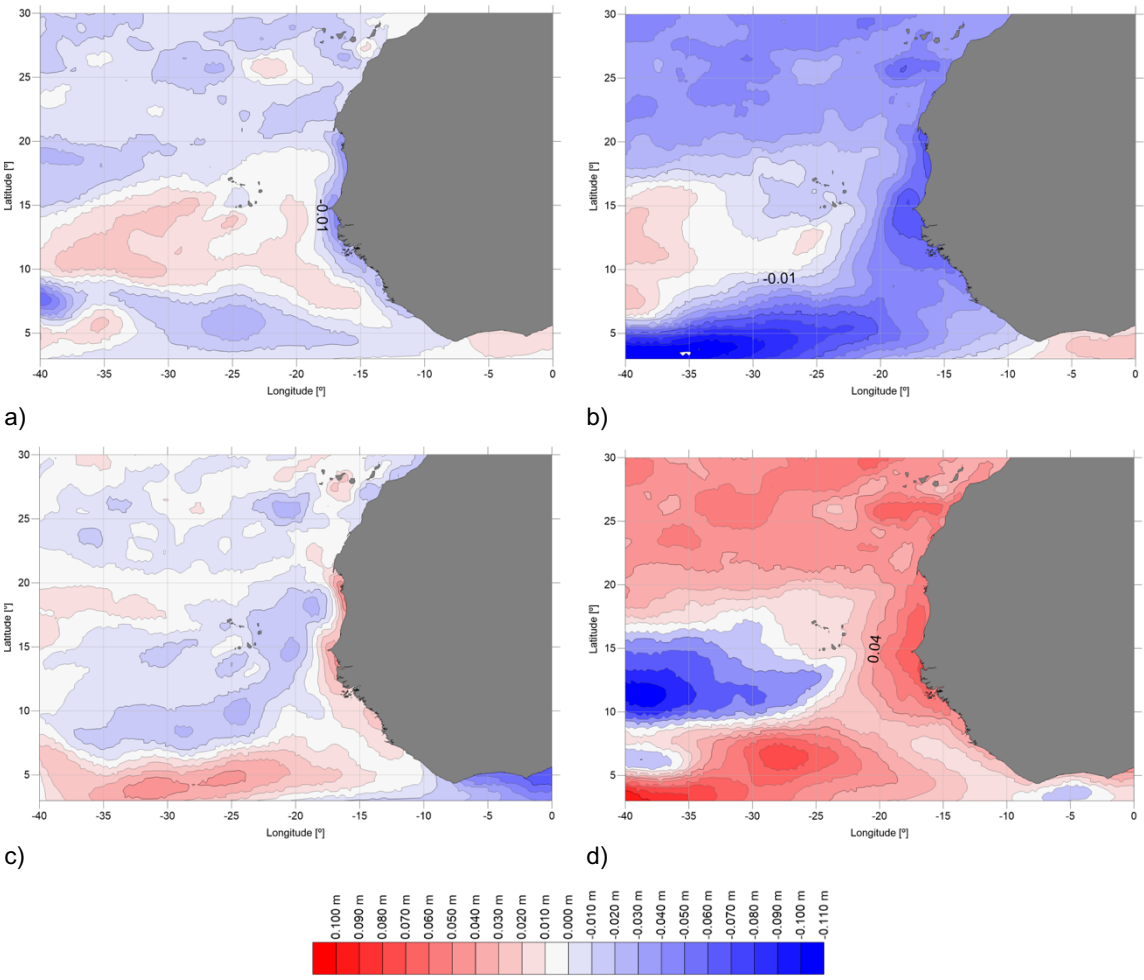

Figure 28 – SLA seasonal means (m) over the 1993 – 2020 period: a) winter, b) spring, c) summer, d) autumn.

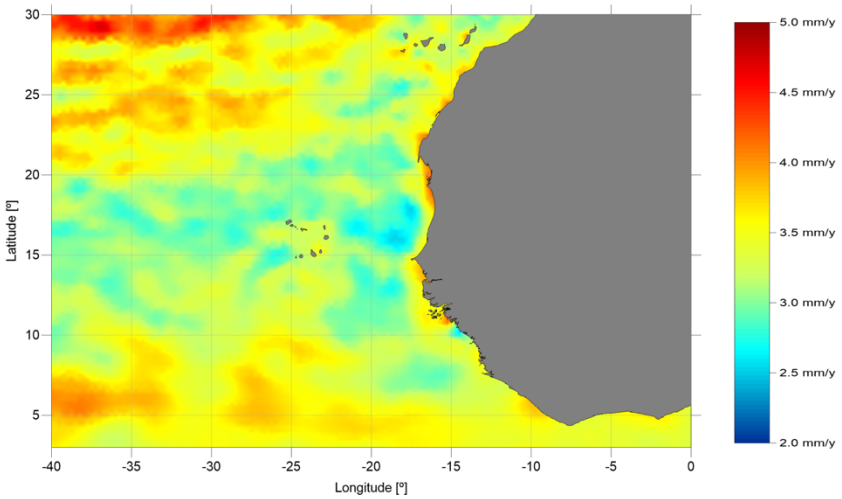

Figure 29 – Regional SLA change for the study area: slope (mm/year) of the linear trend for the 28-year period. Computation includes the GIA correction.

Six relevant peaks are identifiable in the interannual signal (red curve in Figure 30a and Figure 31, second topmost panel), in 1995, 1998, 2001, 2010, 2013, and 2017, from which three coincide with moderate to very strong El Niño events (1995, 1998, 2010). Although an annual, a semi-annual, and also a weaker higher frequency signals can be identified in the PSD (Figure 30b), only the annual and semi-annual ones are clearly identifiable in the time series decomposition (Figure 31).

In the time series decomposition, only the interannual signal shows a positive trend rate (Figure 31, second topmost panel). The residual signal (Figure 31, bottom panel), although with significant amplitude variations, seems to fluctuate around zero without showing a specific trend.

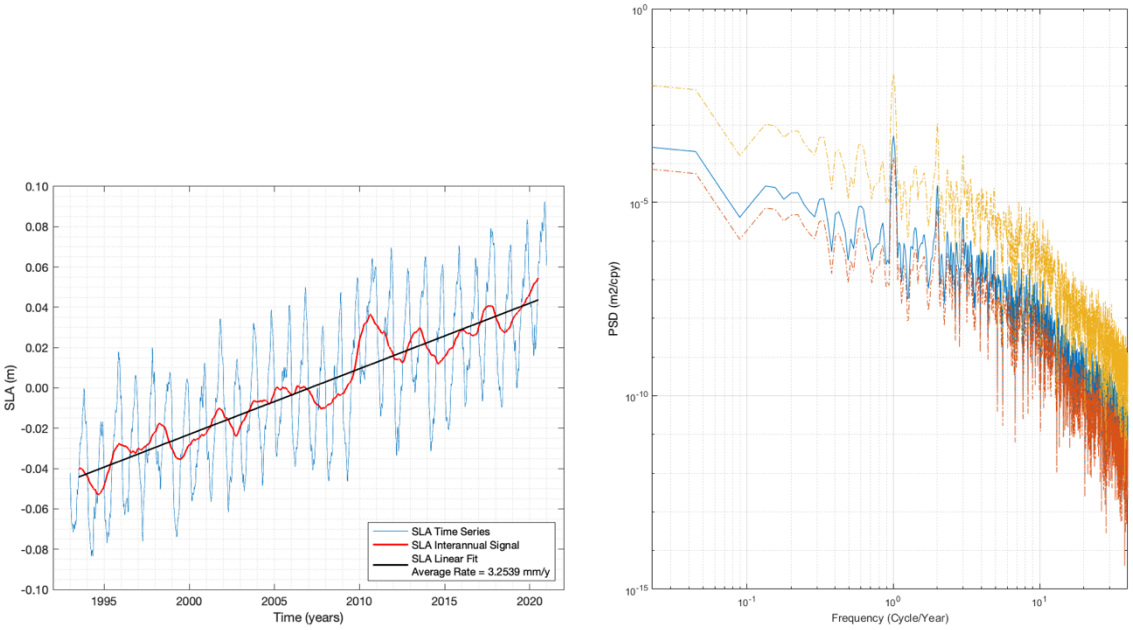

a) b)

Figure 30 – Time series of SLA for the study area (a) and PDS (in blue) (b) for the 28-year period (1993-2020). Red and yellow lines in the PSD identify the lower and upper 95% confidence interval limits, respectively.

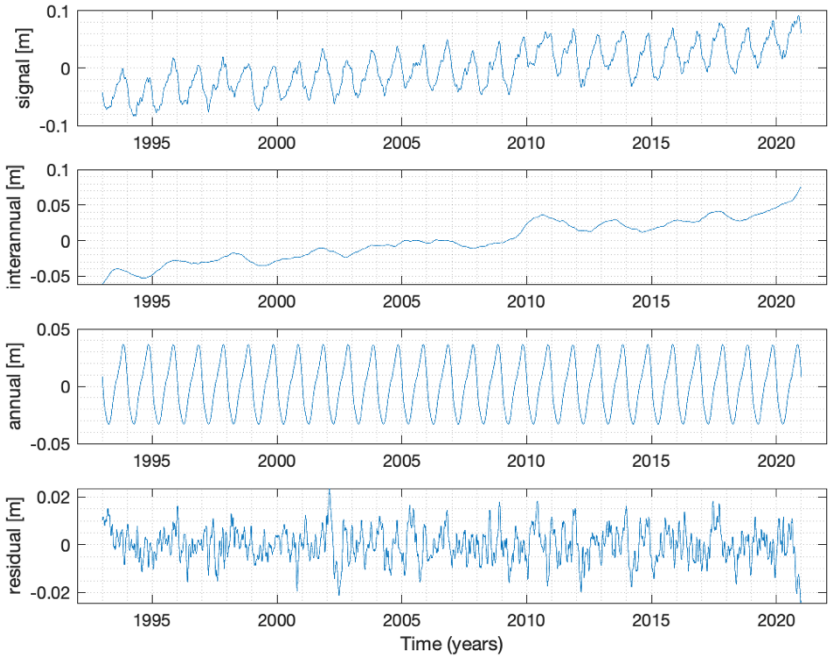

Figure 31 – SLA time series decomposition for the study area over the 28-year period.

3.2.2 EKE

The EKE in the study region seems to be strongly dominated by the NECC's influence acting south of 10°N (Figure 32). Rms values can easily exceed 600 cm^2/s^2, and variances register values over $(60\ cm^2/s^2)^2$ mainly west of 30°W. North of 10°N, the energy levels are generally lower (below 125 cm^2/s^2) except for localized eddies south of the Canary Islands, southwest of Cape Verde archipelago, and in the Guinea coast. These rms energy levels results are in agreement with previous studies (Lázaro et al., 2005). The variance, however, is zero over the whole area north of 10°N, indicating a steady state region, even though intense currents and upwelling processes occur.

The decomposition maps in Figure 33 show that, in the overall study region, the annual and the interannual signals have a much smaller contribution to the total EKE variance, which is therefore dominated by the residual component associated with signals with higher than 1 cycle per year frequency. However, south of 10°N, in the NECC's influence area, the annual component can still contribute up to 25% to the total variance, whereas north of this latitude, although the annual component may be negligible, the interannual component represents up to 15% of the total variance.

A marked seasonal behaviour south of 10°N can be seen in Figure 34, with maximum values in autumn and minimum during spring, following the NECC annual cycle.

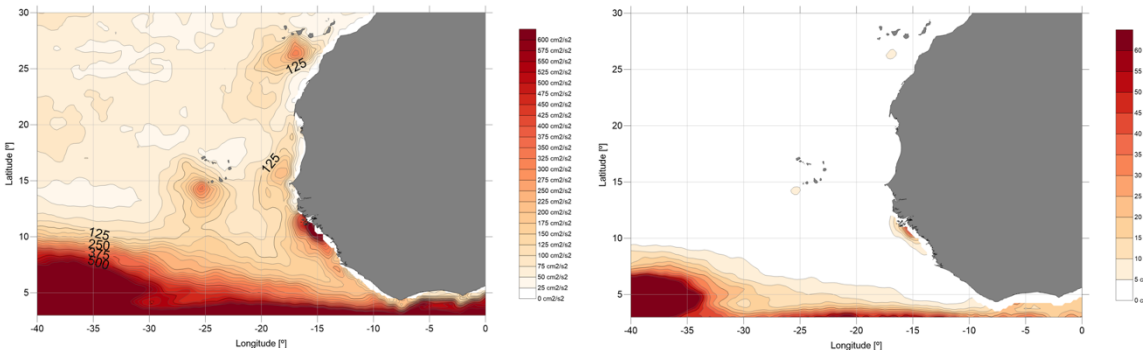

Figure 32 – EKE rms (cm^2/s^2) (a) and variance ($(cm^2/s^2)^2$) (b) over the 28-year period for the study area.

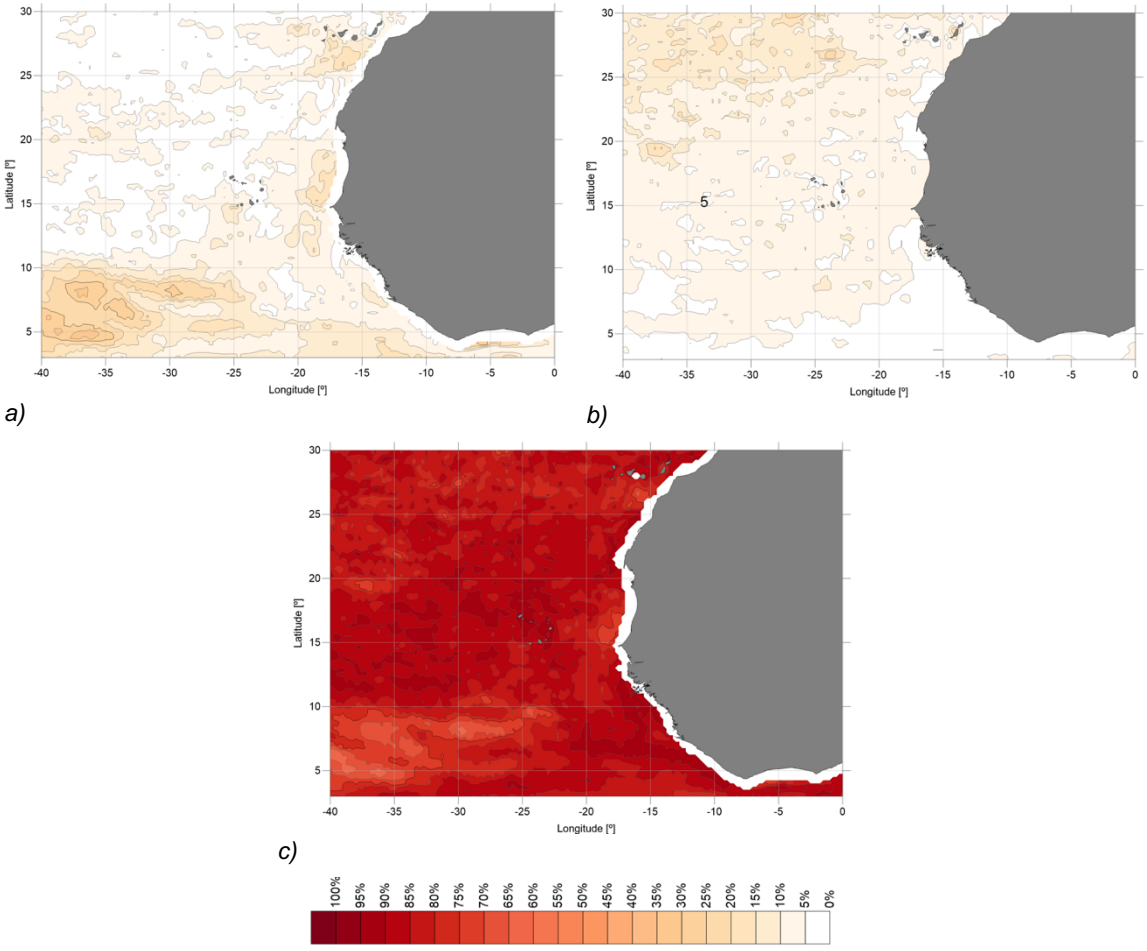

Figure 33 – Contribution of annual, interannual and residual signals in the study area for the total EKE variance. a) percentage of the annual signal contribution, b) percentage of the interannual signal contribution, c) percentage of the residual signal contribution.

The map of linear trends computed from the EKE time series in Figure 35 presents significant differences between north and south of latitude 10°N, where opposite sign trends are particularly relevant, around latitude 5°N, which may be a consequence of the NECC and the nSEC influence. During the total 1993-2020 period, however, the EKE linear trend presents a decreasing rate of -0.41 cm^2/s^2 per year (Figure 36a), in

opposition to the positive linear trend of 0.0064 cm^2/s^2/year for the global mean previously shown in section 0.

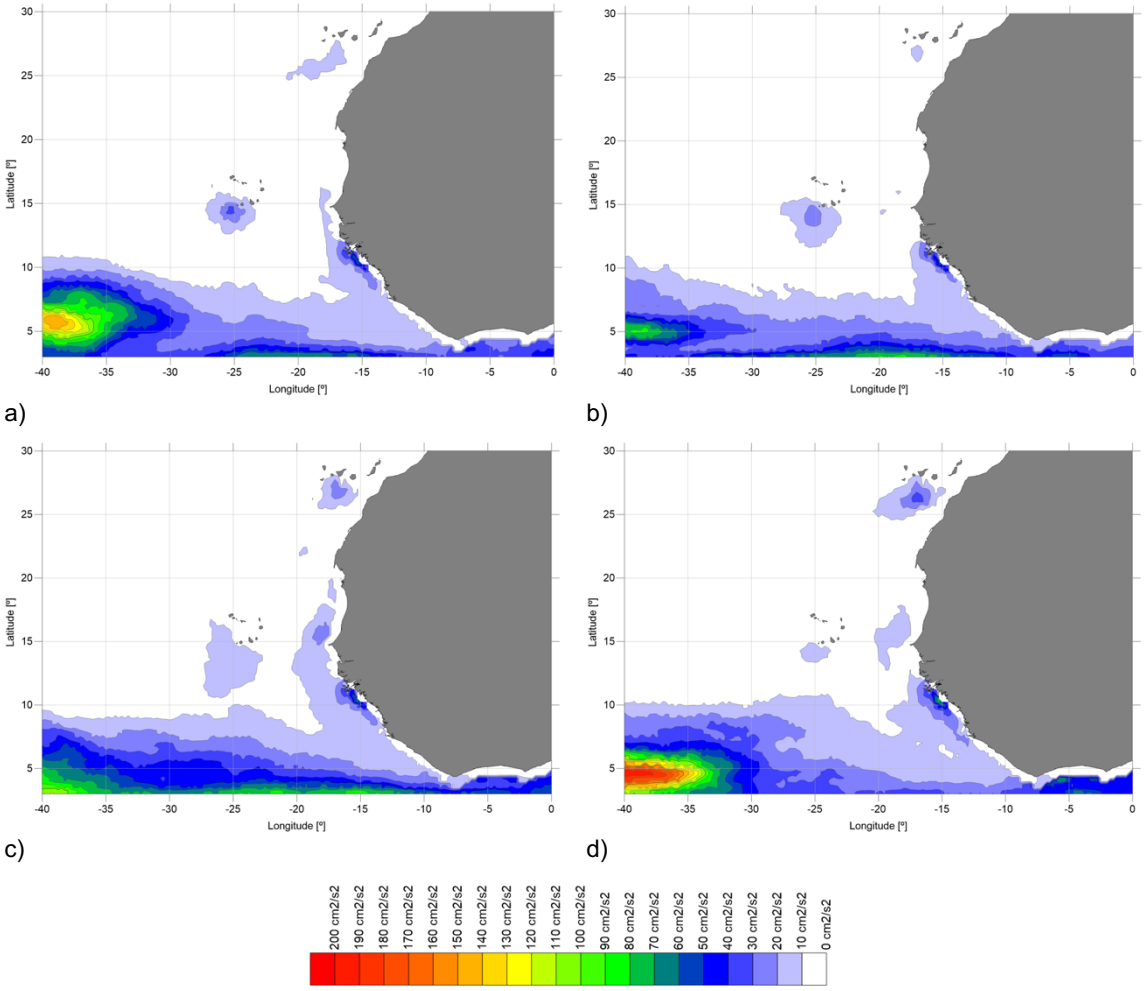

Figure 34 – EKE seasonal means over the 1993 – 2020 period: a) winter, b) spring, c) summer, d) autumn.

The inspection of the interannual variability in Figure 37 (second topmost panel) shows anomalous events occurring in 1994/95, 1996, 1999/00, 2001/02, 2004/05, 2008/09, and 2017/18, being worthy of note that most of them are synchronized with El Niño or La Niña events. Since El Niño events have been associated with a strengthening of the two most active currents at these latitudes, the NECC and the nSEC (Martínez-Moreno et al., 2021), it may be of interest to investigate the eventual influence of these currents in the results. Furthermore, the PSD shown in Figure 36b, shows that EKE presents an annual and a semi-annual signal, and the time series decomposition in Figure 37 (third topmost panel) shows that the maximum values of those signals occur around summer and autumn. The semi-annual signal disappears when the time series is computed for latitudes between 10°N and 30°N (not shown in this report), excluding the latitude band most influenced by the NECC and the nSEC.

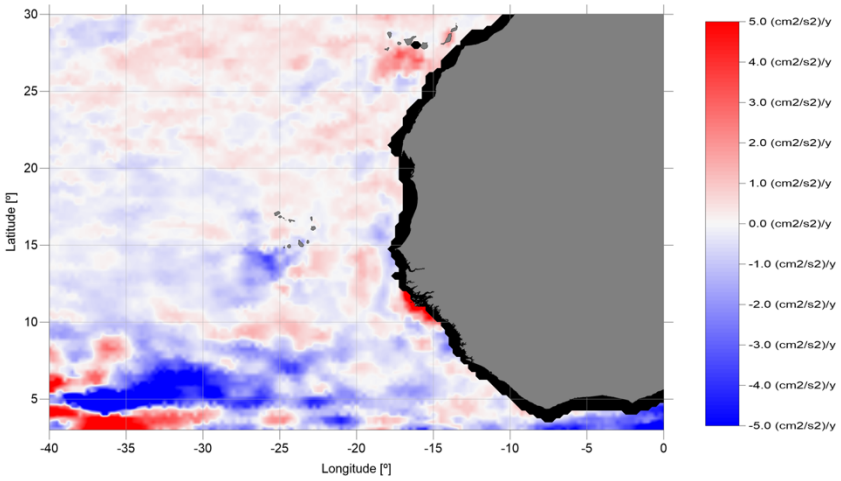

Figure 35 – Regional EKE change for the study area: slope (cm^2/s^2//year) of the linear trend for the 28-year period.

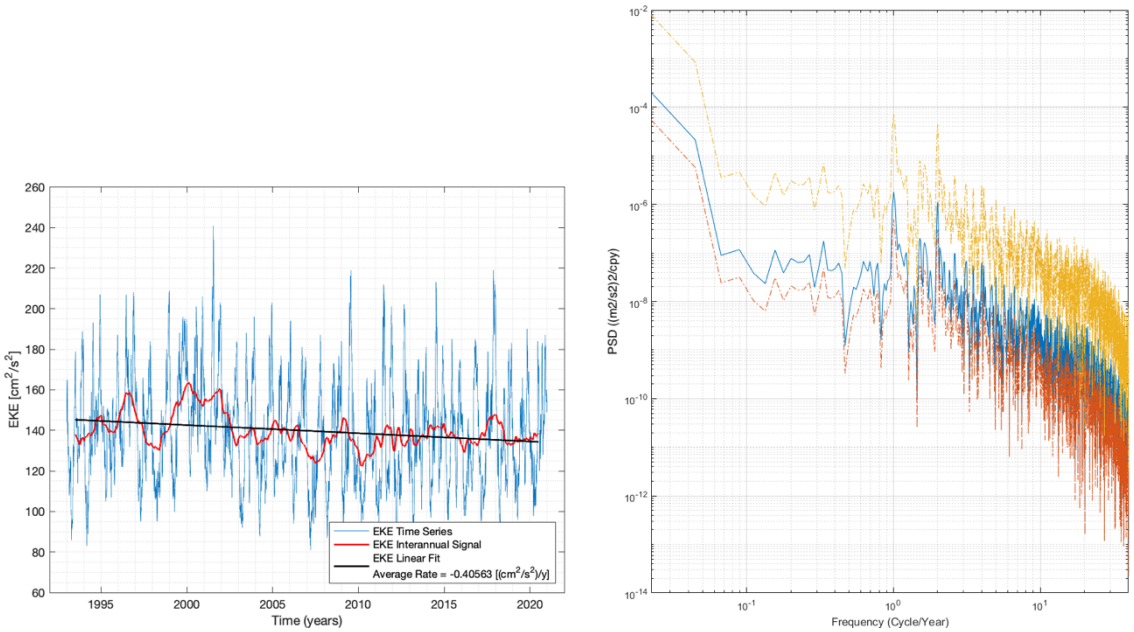

a) b)

Figure 36 – Time series of mean EKE for the study area (a) and PSD (in blue) (b) for the 28-year period). Red and yellow lines in the PSD identify the lower and upper 95% confidence interval limits, respectively.

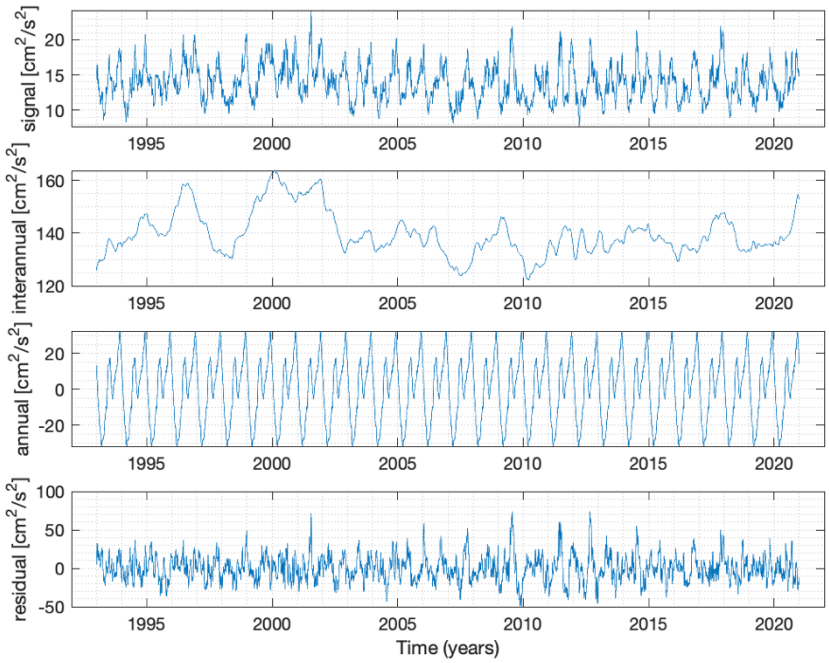

Figure 37 – EKE time series decomposition for the study area over the 28-year period.

3.2.3 Magnitude of the surface geostrophic currents

The rms and variance of the magnitude of the surface geostrophic currents computed for the study region (Figure 38) show that the highest values occur south of 10°N, in the area where the NECC develops and also along the African coast, in the GC region. The variance in these areas also shows significant values, up to 0.09 m^2/s^2, indicating that these regions present higher instability. North of 10°N, the variance is mostly zero, although rms values can still reach up to 0.15 m/s, denoting a steady state region. These results are in good agreement with the previous EKE analysis.

South of 10°N, the decomposition maps (Figure 39) show that the variance's annual component can contribute up to 40-45% to the total variance, in the NECC and GC regions. North of 10°N, however, the residual component prevails, indicating that the magnitude signal may have a frequency of more than one cycle per year. The interannual component has a negligible contribution to the total magnitude variance in the study region, with a maximum of around 10% in the latitudes north of 25°N.

The seasonal means represented in Figure 40 show that the currents are stronger in the autumn and weaker during spring, in agreement with the typical NECC maximum and minimum values, respectively. The direction of the currents, represented in Figure 40 shows the NECC feeding the GC, which reaches its maximum values in summer, and drifting north to feed the MC during summer and autumn (Figure 40c and d). Also,

during summer and autumn, the NEC can be identified as a broad southwest flow (Figure 40c and d).

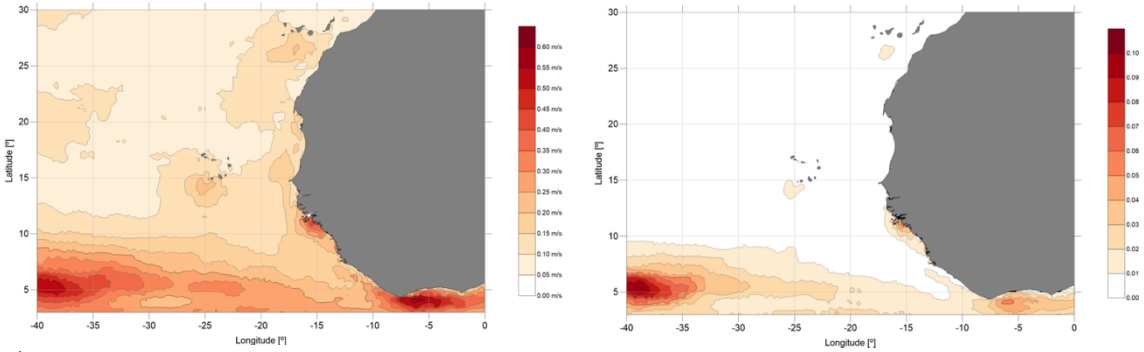

Figure 38 – Rms (m/s) (a) and variance (m^2/s^2) (b) of the magnitude of the surface geostrophic currents over the 28-year period in the study area.

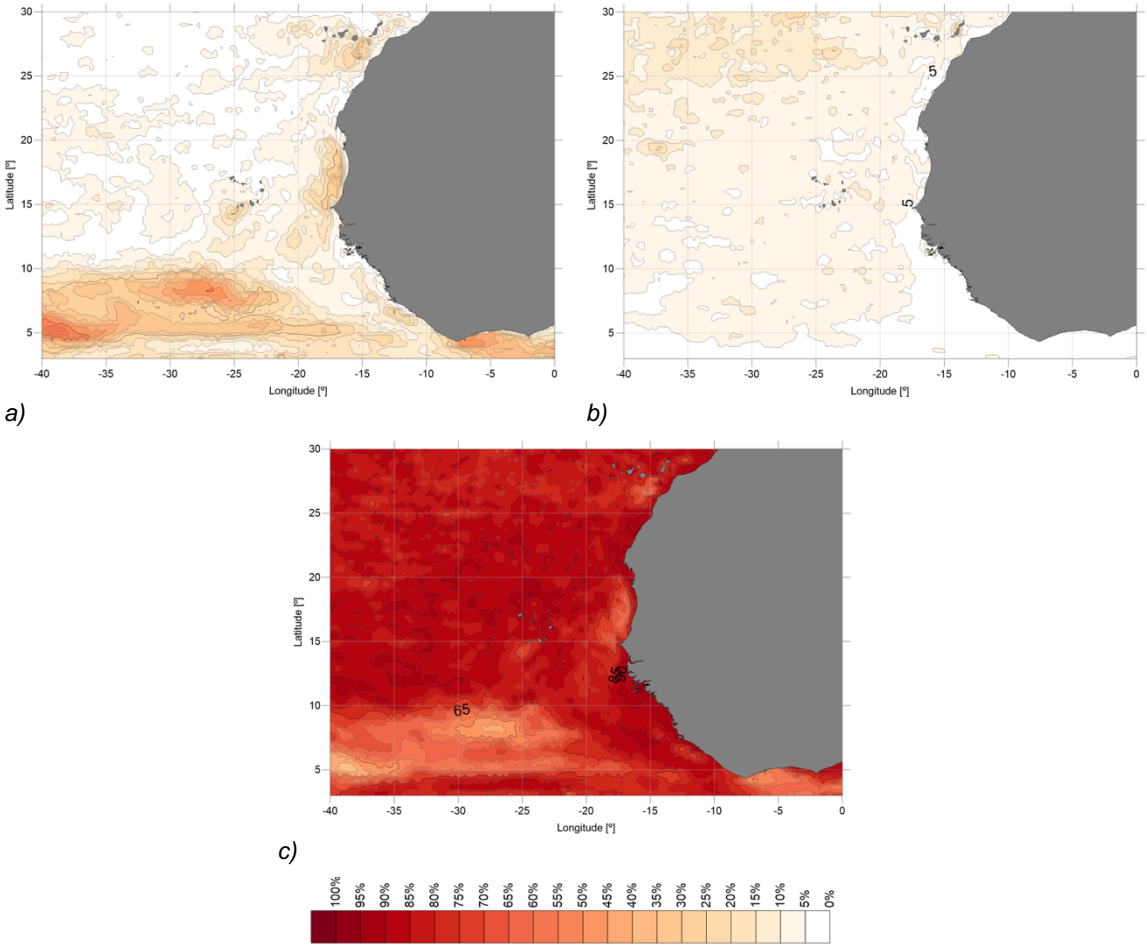

Figure 39 –Contribution of the annual, interannual and residual components of the magnitude to the total variance. a) percentage of the annual signal contribution, b) percentage of the interannual signal contribution, c) percentage of the residual signal contribution.

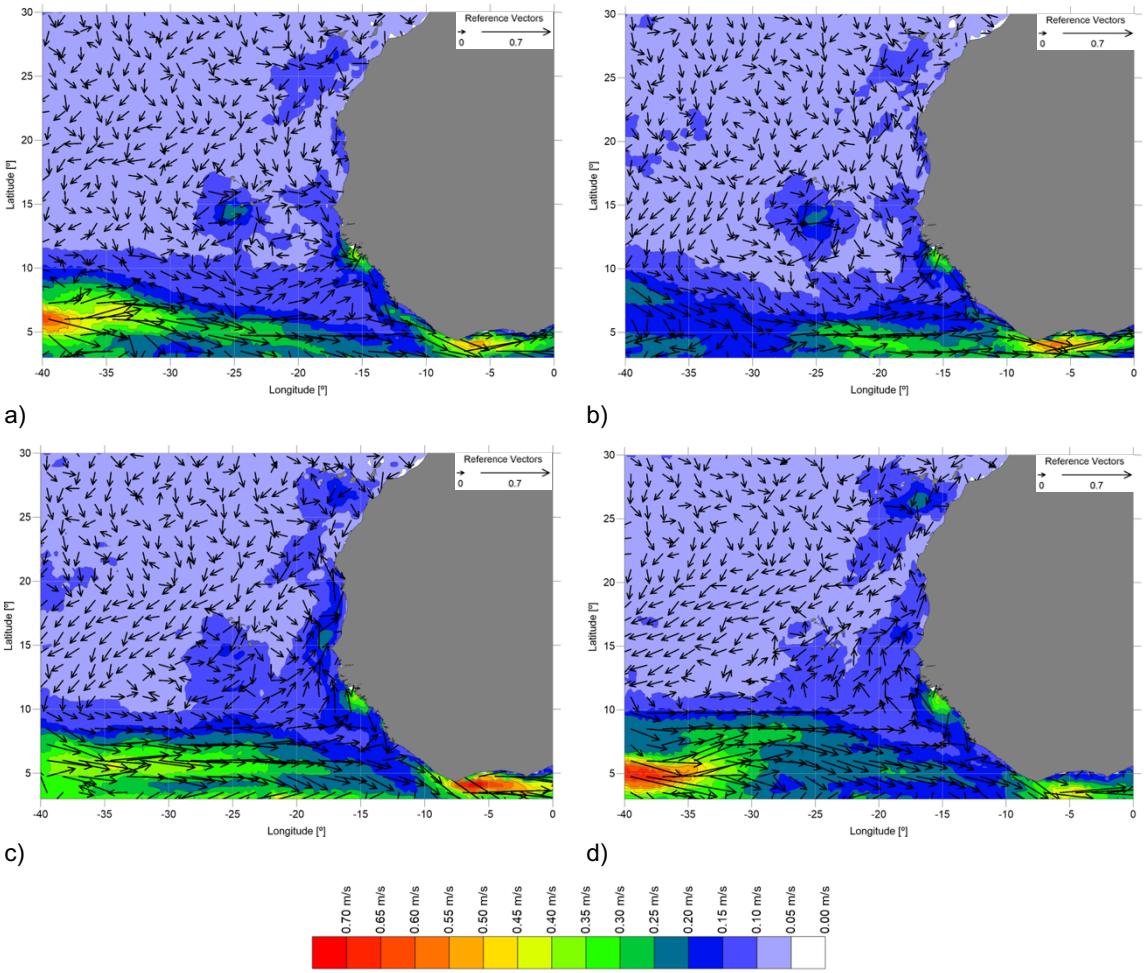

Figure 40 – Magnitude seasonal means (coloured) and geostrophic currents means (vectors) over the 1993 – 2020 period: a) winter, b) spring, c) summer, d) autumn.

Although increasing and decreasing trends of the magnitude of the surface geostrophic currents are found along the study area (Figure 41), the overall 1993-2020 magnitude trend is negative and equal to -6.2×10^{-5} m/s per year (Figure 42a), in opposition to the positive mean global trend of 3.0×10^{-5} m/s/year shown previously in section 3.1.3. South of 10°N, opposite sign trends, similar to the ones for EKE, are shown around latitude 5°N, which may be a consequence of the NECC and nSEC influence in the area. Along the African coast, the magnitude of the surface geostrophic currents seems to be increasing. This could be related to the fact that this is a region where strong upwelling occurs, causing the sea level to decrease significantly, which increases the cross-shore pressure gradient due to the sea level difference between the coastal and offshore regions and enhances the surface geostrophic current along the coast (Jung & Cho, 2020). However, further investigation is needed, taking also into account upwelling-inducing mechanisms, such as wind stress and meanders (since this is an energetic region), to clarify these results.

Besides an annual and semi-annual signal, the PSD (Figure 42b) also shows the existence of a third weaker and lower frequency seasonal signal, even though in the time series decomposition (third topmost panel in Figure 43) only two signals are visible: one peaking in summer and the other in autumn. However, the semi-annual signal visible (third topmost panel in Figure 43) disappears if the time series is computed only for latitudes between 10°N and 30°N (not shown in this report), excluding the latitude band most influenced by the NECC and the nSEC.

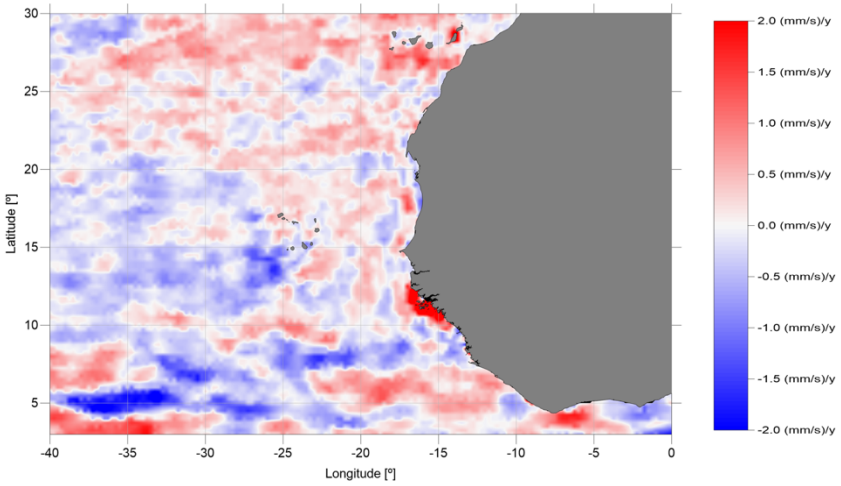

Figure 41 – Regional change of the magnitude of the surface geostrophic currents for the study area: slope (mm/s/year) of the linear trend for the 28-year period.

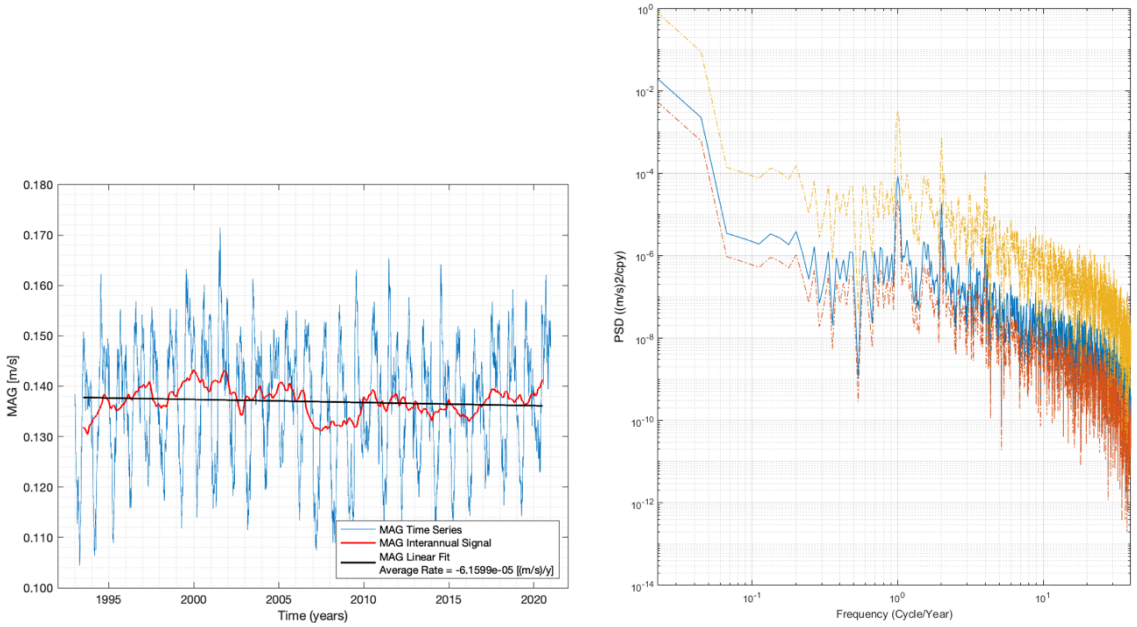

a) b)

Figure 42 – Time series of mean magnitude for the study area (a) and PSD (in blue) (b) for the 28-year period. Red and yellow lines in the PSD identify the lower and upper 95% confidence interval limits, respectively.

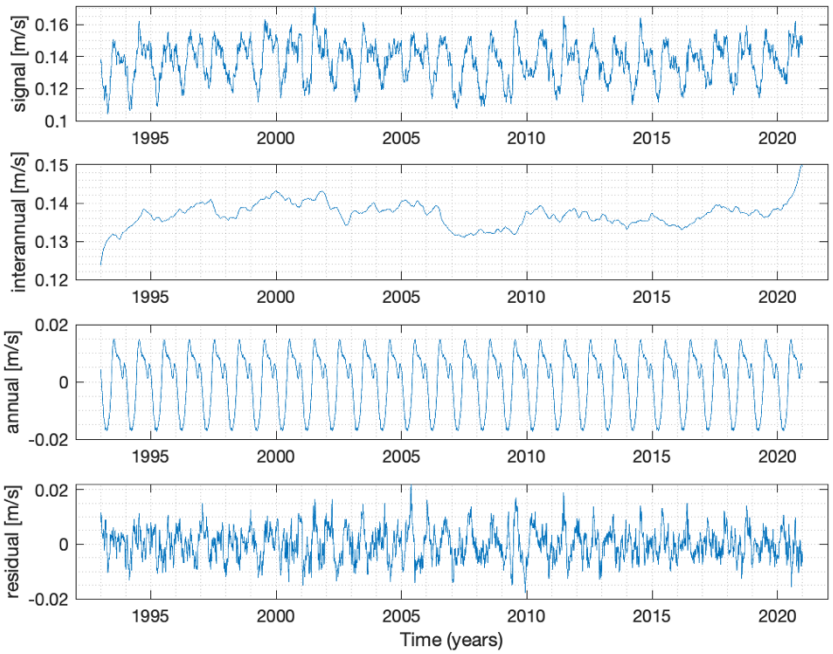

Figure 43 – Magnitude time series decomposition for the study area over the 28-year period.

3.3 Characterization of the climate indices

The seasonal mean indices states are presented in Figure 44 for the overall 28 years period. Significant positive phases are highlighted in red using a threshold value of +0.5σ (σ being the s.d.) and negative phases are highlighted in blue using a threshold value of -0.5σ. In a preliminary analysis of the indices' states, it may be noted:

- NAO seasonal states seem to show a pattern shift after 2007, in particular during summer, with a predominance of negative phases, and during autumn, with a predominance of positive ones. The reasons for this shift should be investigated. During winter, when the index has a stronger impact, the predominance of positive states agrees with the increasing trend over the last decades referred to by Hurrel (1995) and by Stephenson et al. (2000).
- TNA winter and summer positive and negative states resemble each other while spring and autumn states seem to oppose each other, with spring having a prevalence of negative phases and autumn of positive ones. It is also worthy of note the long period between 2001 and 2017 where there has not been any negative TNA index phase during autumn.
- TSA spring and autumn states seem to oppose each other in a mirror way relating to TNA. In this case, the prevalence of positive phases occurs in autumn and the positive ones in spring. This fits with what would be expected

since both TNA and TSA indices characterize SST gradients but in different hemispheres.

- AMM spring and autumn states seem to oppose each other similarly to TNA. However, the exclusively positive phases during autumn are more extensive than TNA, ranging from 1995 to 2017. Also, winter presents a long period of only positive phases, from 1996 to 2013.
- WHWP states are clearly distinct for winter and spring, with almost only negative phases, and for summer and autumn with almost only positive ones, as would be expected since its effects start in the eastern Pacific in spring and only then start to expand into the Atlantic during summer up until early autumn (Wang & Enfield, 2001). Summer and autumn relevant positive phases generally coincide with El Niño events during the previous winter and spring (Climate Prediction Center Internet Team, 2022), with emphasis on the 1997/98 and 2014/2016 peaks with positive phases also in winter and spring, following two of the major El Niño events registered.
- SOI winter negative phases occur during El Niño years and the positive phases allow us to generally identify La Niña years (Climate Prediction Center Internet Team, 2022), as would be expected.

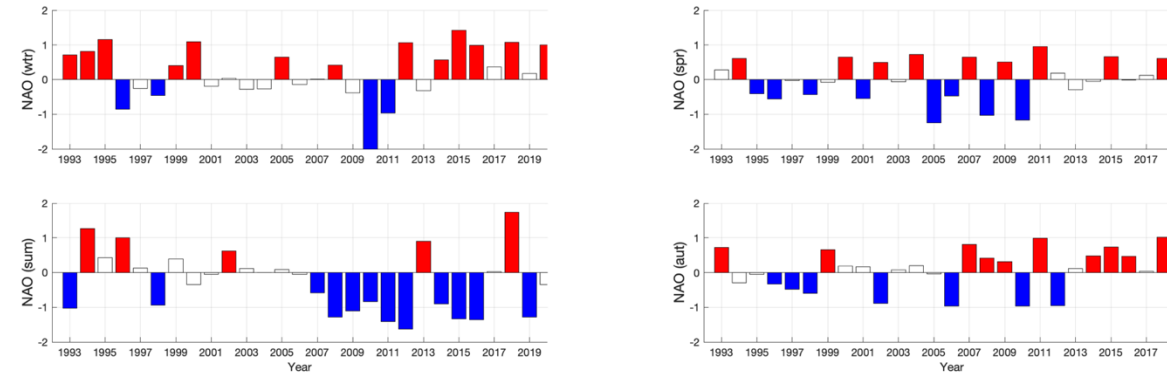

a)

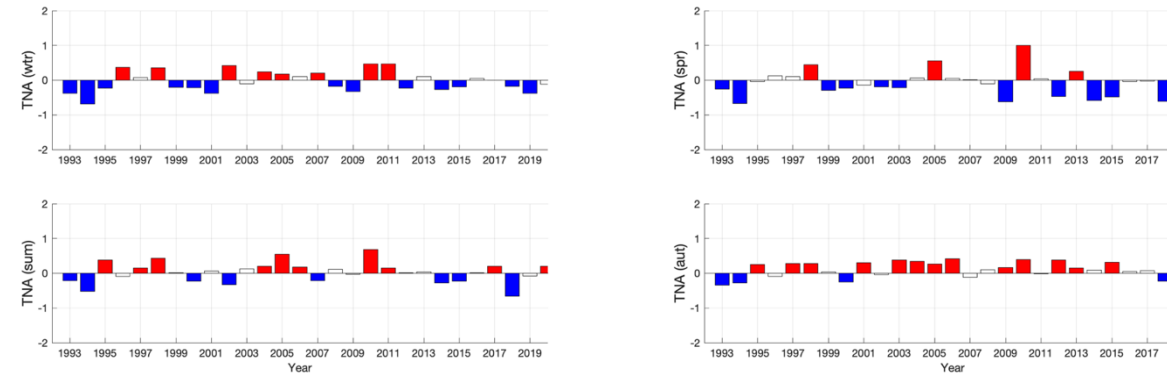

b)

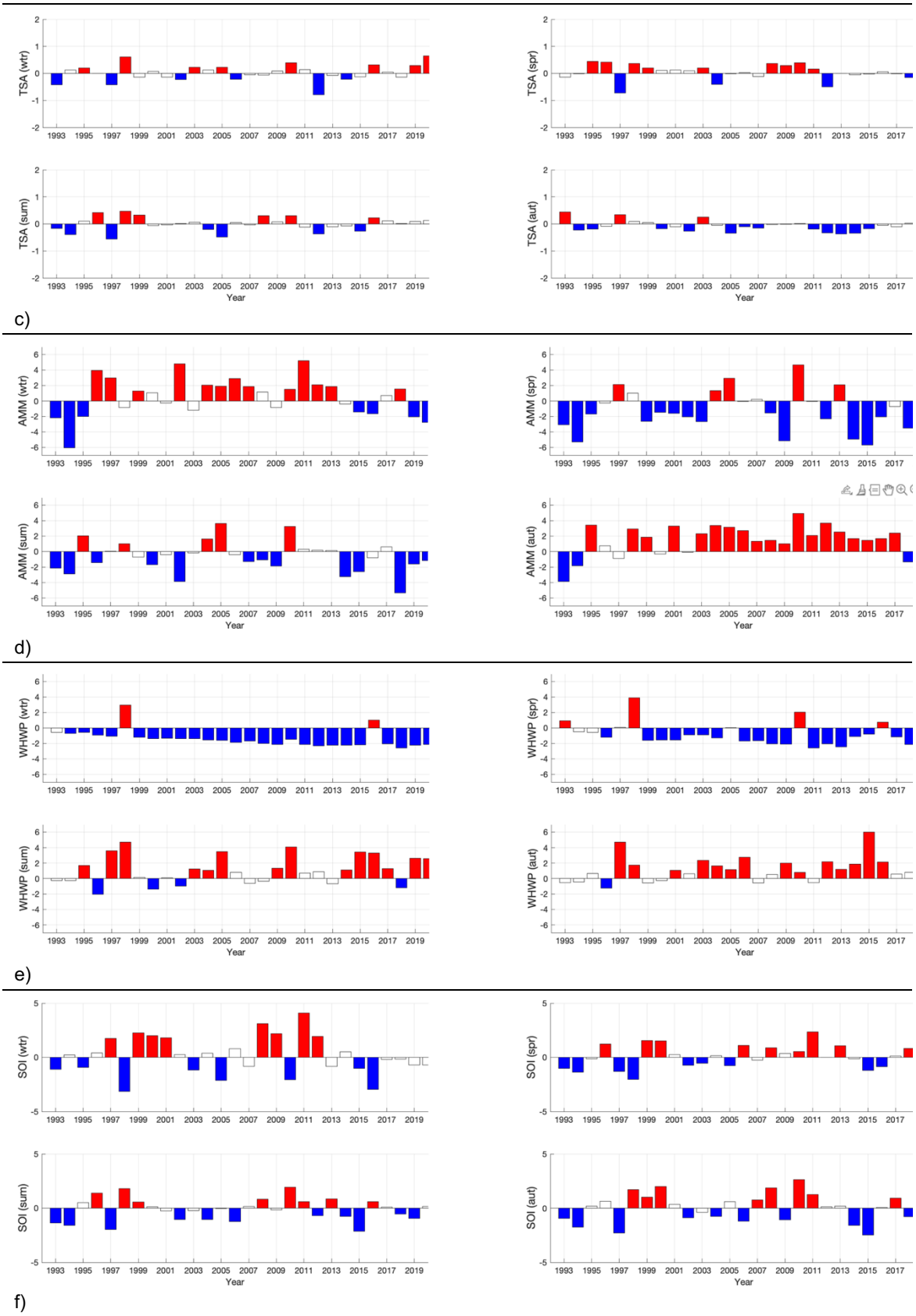

Figure 44 – CI standardized seasonal mean time series over the 28-year period: a) NAO, b) TNA, c) AMM, d) TSA, e) WHWP, f) SOI

Other CI were analysed, namely:

- East Atlantic (EA), defined as a difference in SLP between a dipole of anomalies between two centres located over Greenland and the British Islands–Baltic Sea area (Criado-Aldeanueva & Soto-Navarro, 2020).
- East Atlantic–West Russia (EA–WR)[16], consisting of the difference of SLP between four main anomaly centres located over Europe, Northern China, the central North Atlantic, and the north of the Caspian Sea;
- Atlantic Multidecadal Oscillation (AMO) index, based on the North Atlantic SST (Enfield et al., 2001);
- East Central Tropical Pacific SST (Niño 3.4)[17] in the region from 5°N to 5°S and 170 to 120°W.

However, the correlations found did not present particular interest and therefore were excluded from this dissertation.

3.4 Correlation maps

3.4.1 NAO

The correlation between the NAO index and the SLA (Figure 45a and d) seems to be stronger during winter when this CI is usually more relevant, although areas with some extension can still also be found during spring. During winter, when both the NAO and the CC are stronger, the higher negative correlation values seem to go along with this current's path, all the way from the African coast at around 33°N and also drifting west at around 20°N. The strong negative correlation along the coast north of 20°N, both in winter and spring, coincides with the area of continuous upwelling.

Mean EKE levels during NAO negative phase (Figure 45c and f) show an energy increment when compared with the mean EKE levels during its positive phase, between latitudes 15°N and 25°N (Figure 45 b and e), consistent with a sea level rising probably due to the weakening of the Azores high-pressure centre during NAO negative phase.

[16] https://www.cpc.ncep.noaa.gov/data/teledoc/eawruss.shtml
[17] https://psl.noaa.gov/data/climateindices/list/

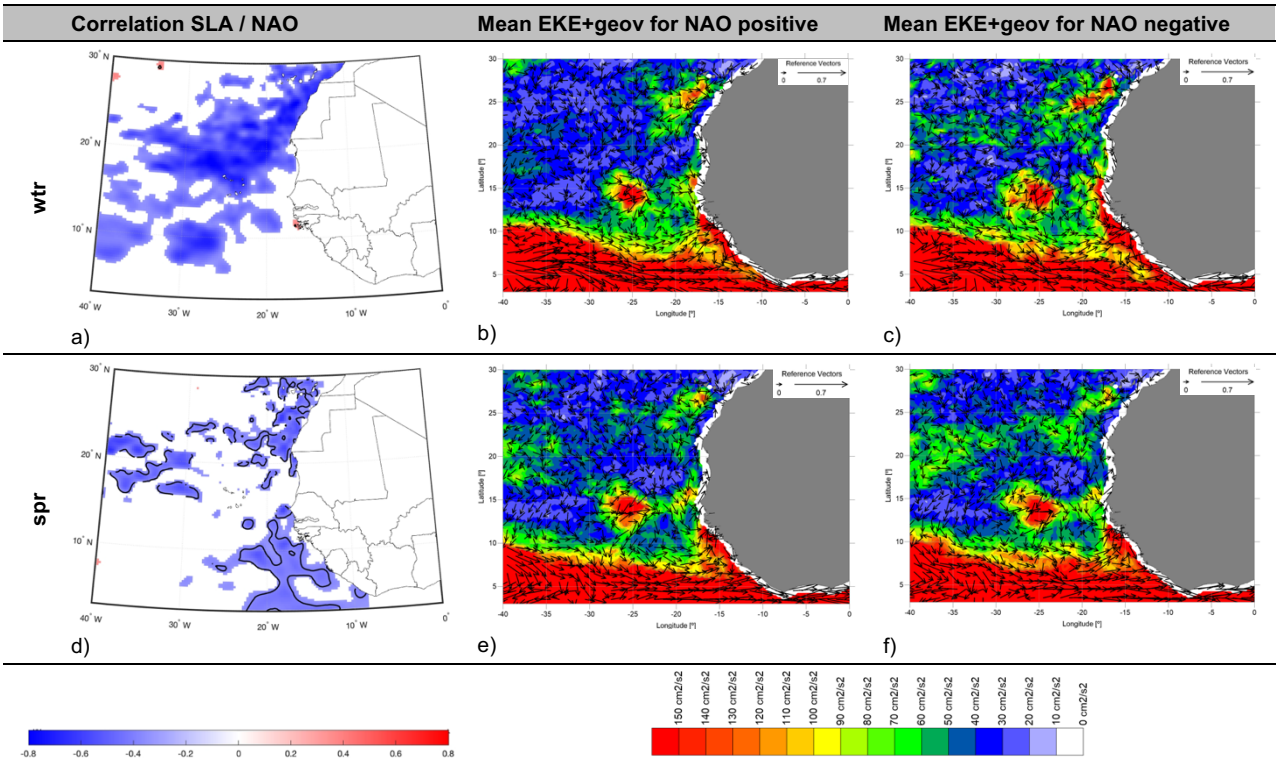

Figure 45 – Seasonal significant correlations (95% confidence) between SLA and NAO index (a and d). EKE (in colour) and geostrophic velocities (in vectors in m/s) means during positive (b and e) and negative (c and f) phases of the NAO pattern. EKE colour scaling was saturated south of 10° N so that the energy patterns could emerge outside the band dominated by the NECC.

3.4.2 TNA

Positive correlation values between TNA and SLA occur mainly in winter, spring, and summer (Figure 46a, d and g). The larger correlation areas are found during spring and summer. This could be related to the augment of the SST, and its consequent increase in sea level, associated with the highest solar radiations that reach this region during summer months. In autumn, the correlation areas are smaller, but strong correlation values can still be seen along the African coast, north of 10°N, in the areas characterized by strong upwelling.

For each season, the mean EKE during the months when the TNA is positive (Figure 46b, e and h) seems to be higher when compared with the mean EKE for the months when the TNA is negative (Figure 46c, f and i). Since the TNA is a mode that takes into consideration the SSTA, it is logical to think that the higher SST in the region (positive TNA values), the more energy at the surface of the ocean. So, a stronger EKE activity could be expected in the region. This difference is more evident in the seasons when the high correlation area is larger, as during spring along the band between latitudes 15°N and 25°N (Figure 46e and f). During autumn, when the correlation is weaker, and possibly because they are the result of the SST anomalies in the area that persisted for

more than one season after they were generated (Huang & Shukla, 2005), the differences between the mean EKE during the TNA positive and negative phases are not so obvious (Figure 46k and l).

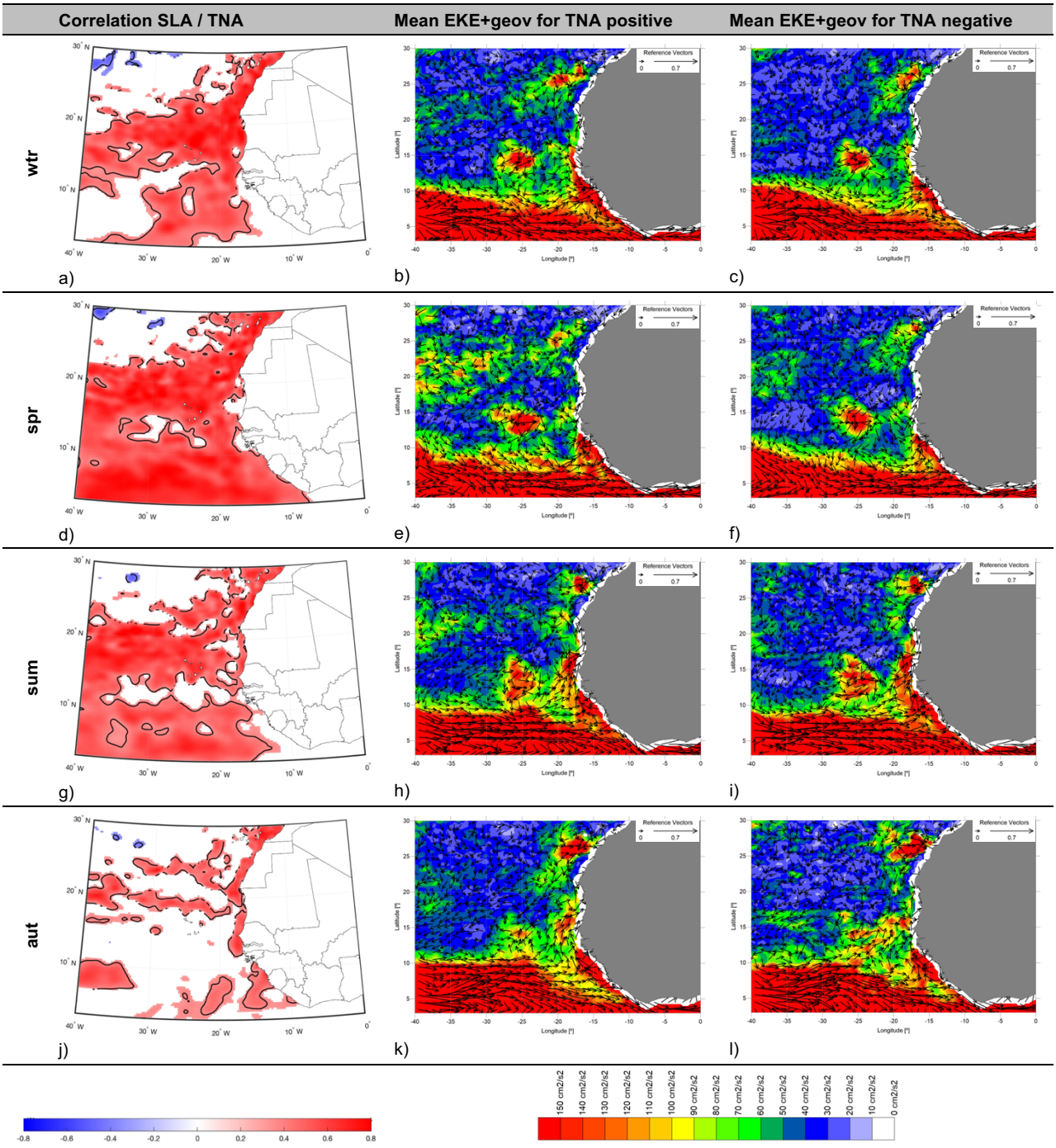

Figure 46 – Seasonal significant correlations (95% confidence) between SLA and TNA index (a, d, g, and j). EKE (in colour) and geostrophic velocities (in vectors in m/s) means during positive (b, e, h, and k) and negative (c, f, l, and l) phases of the TNA pattern. EKE colour scaling was saturated south of 10° N so that the energy patterns could emerge outside the band dominated by the NECC.

3.4.3 TSA

High correlation values were found between the TSA index and SLA during winter, spring and summer although in limited areas (Figure 47a, d and g). A positive correlation is mainly concentrated along the African coast while a negative correlation spot can be found in the bottom left corner of the study area (around 5ºN and 35ºW) during winter and summer. The positive correlation during winter along the African coast north of 20°N coincides with the continuous upwelling in the area. South of 10ºN, positive correlation areas are identified during winter and spring but in summer they are limited to the zonal-oriented African coast of the Ivory Coast and Ghana. This may be related to the maximum intensities of the NECC and the GD during this season.

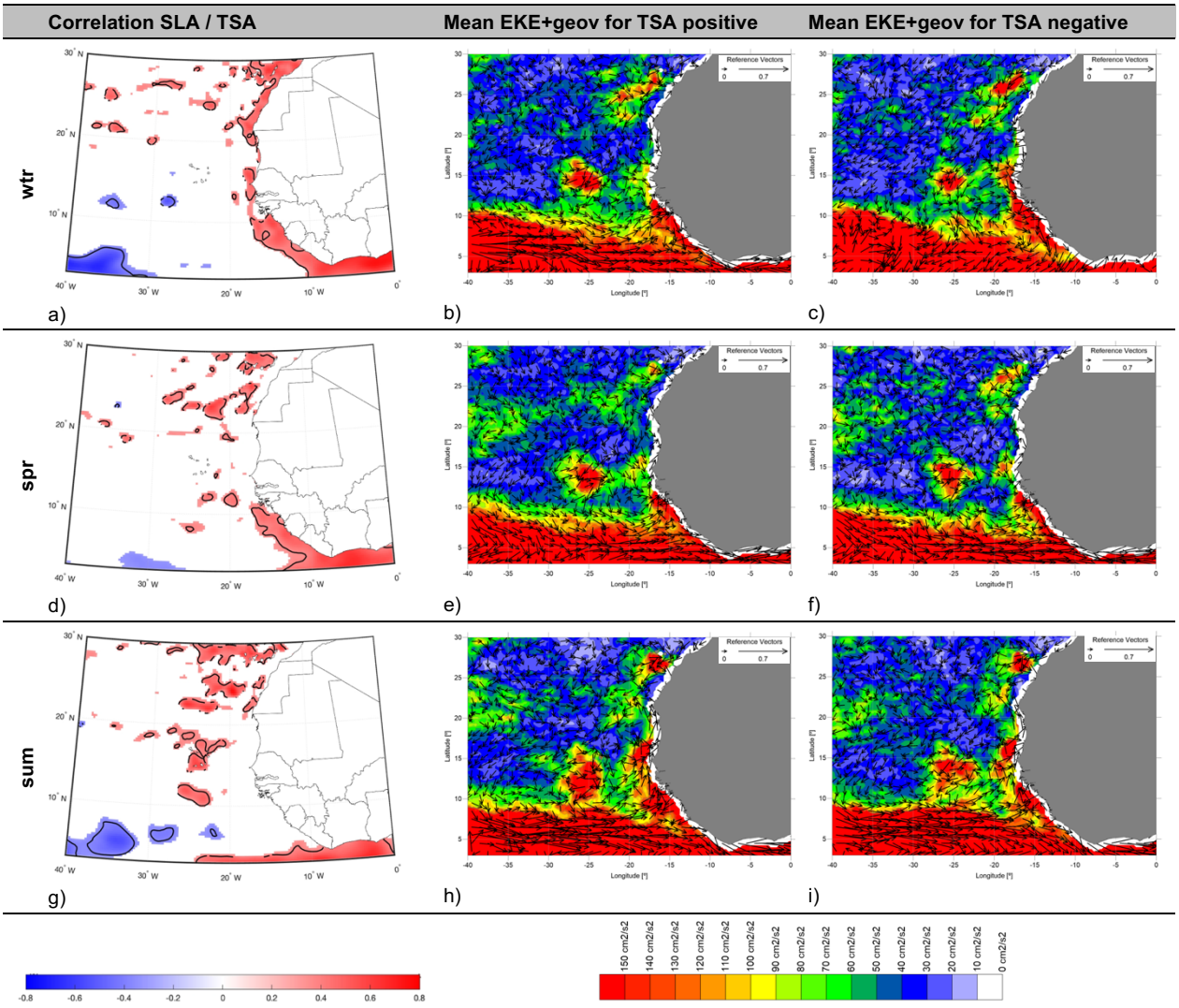

Figure 47 – Seasonal significant correlations (95% confidence) between SLA and TSA index (a, d and g). EKE (in colour) and geostrophic velocities (in vectors in m/s) means during positive (b, e, and h) and negative (c, f, and I) phases of the TSA pattern. EKE colour scaling was saturated south of 10° N so that the energy patterns could emerge outside the band dominated by the NECC.

Figure 48 presents the same data as Figure 47, but now the EKE colour scaling was desaturated south of 10°N to allow a more detailed analysis of the latitude band where the negative spot is shown in the correlation maps. In winter and summer, the geostrophic velocities and the mean EKE seem to present a different pattern south of 10°N, during TSA positive (Figure 47b and h, Figure 48b and h) and negative (Figure 47c and i Figure 48c and i) phases. During the negative phases, the velocities show higher turbulence and higher mean EKE, west of 30-35°W, particularly in winter. This variation may be contributing to the negative correlation spots (Figure 47a and g, Figure 48a and g), not present in spring, when the geostrophic velocities and the mean EKE seem to be very alike during both TSA positive (Figure 47e, Figure 48e) and negative (Figure 47f, Figure 48f) phases.

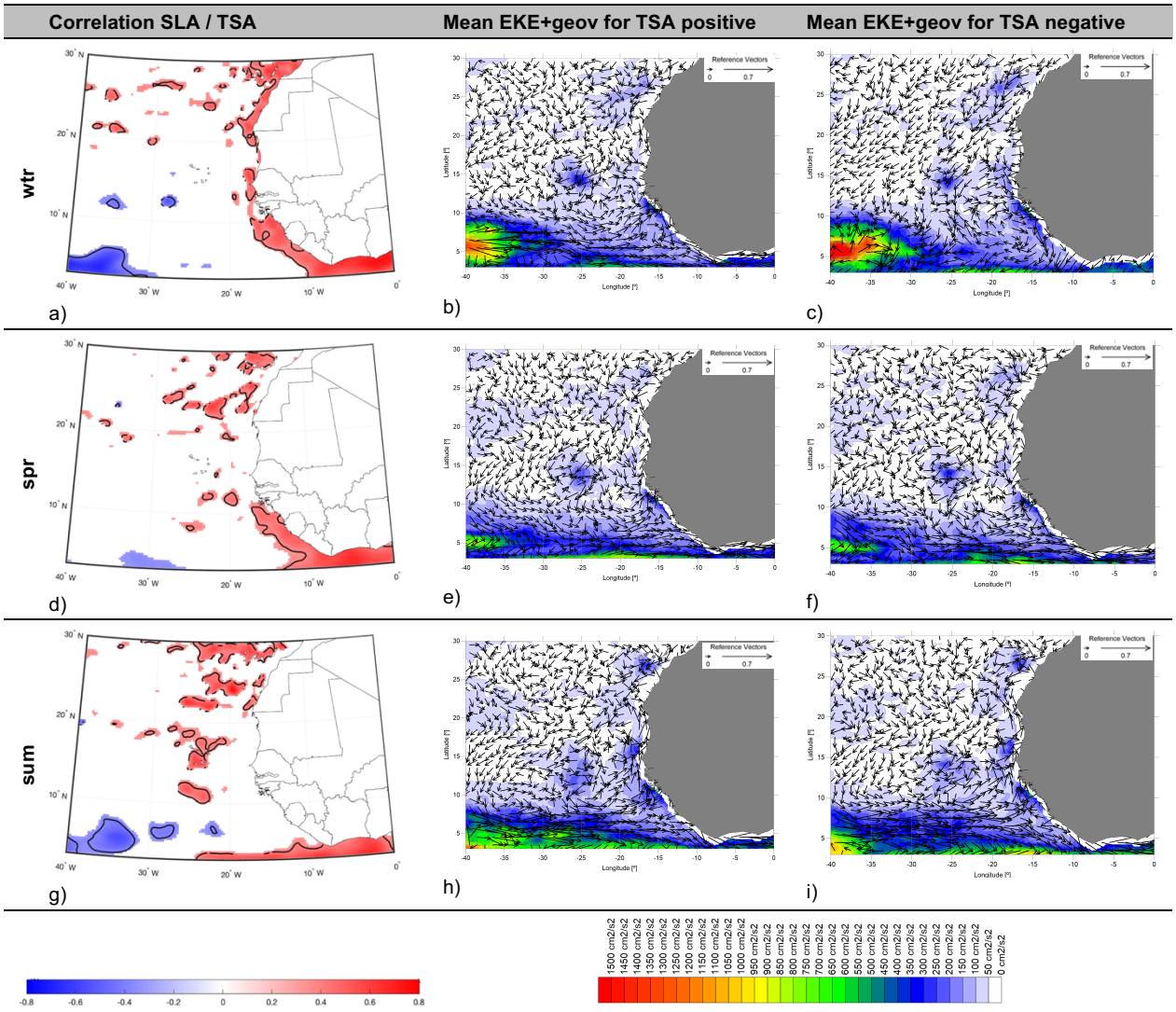

Figure 48 – Same as Figure 47 using a desaturated EKE colour scaling south of 10° N so that the energy patterns could emerge in this latitude band.

3.4.4 AMM

The AMM pattern behaviour is very similar to the one observed from the TNA (subsection 3.4.2), with the highest positive correlations occurring from winter to summer and in a particularly extended area during spring (Figure 49a, d and g) when the CI variance usually reaches its maximum (Vimont & Kossin, 2007). During autumn, though high positive correlations were found, they occur in more limited and scattered areas (Figure 49j) and, similar to TNA, they may be related to the persistence of the SST anomalies in the area for more than one season after they were generated (Huang & Shukla, 2005).

The positive correlation along the African coast between 10°N and 20°N during summer and autumn coincides with the minimum of the seasonal upwelling in the area, which usually reaches its maximum intensity during winter and spring (Mittelstaedt, 1991).

Finally, the energy patterns shown in the maps are in line with the previously stated for the TNA pattern, with higher mean EKE intensity levels during AMM positive phases (Figure 49b, e, and h) than during negative phases (Figure 49c, f, and i), particularly between latitudes 15° N and 25° N in spring.

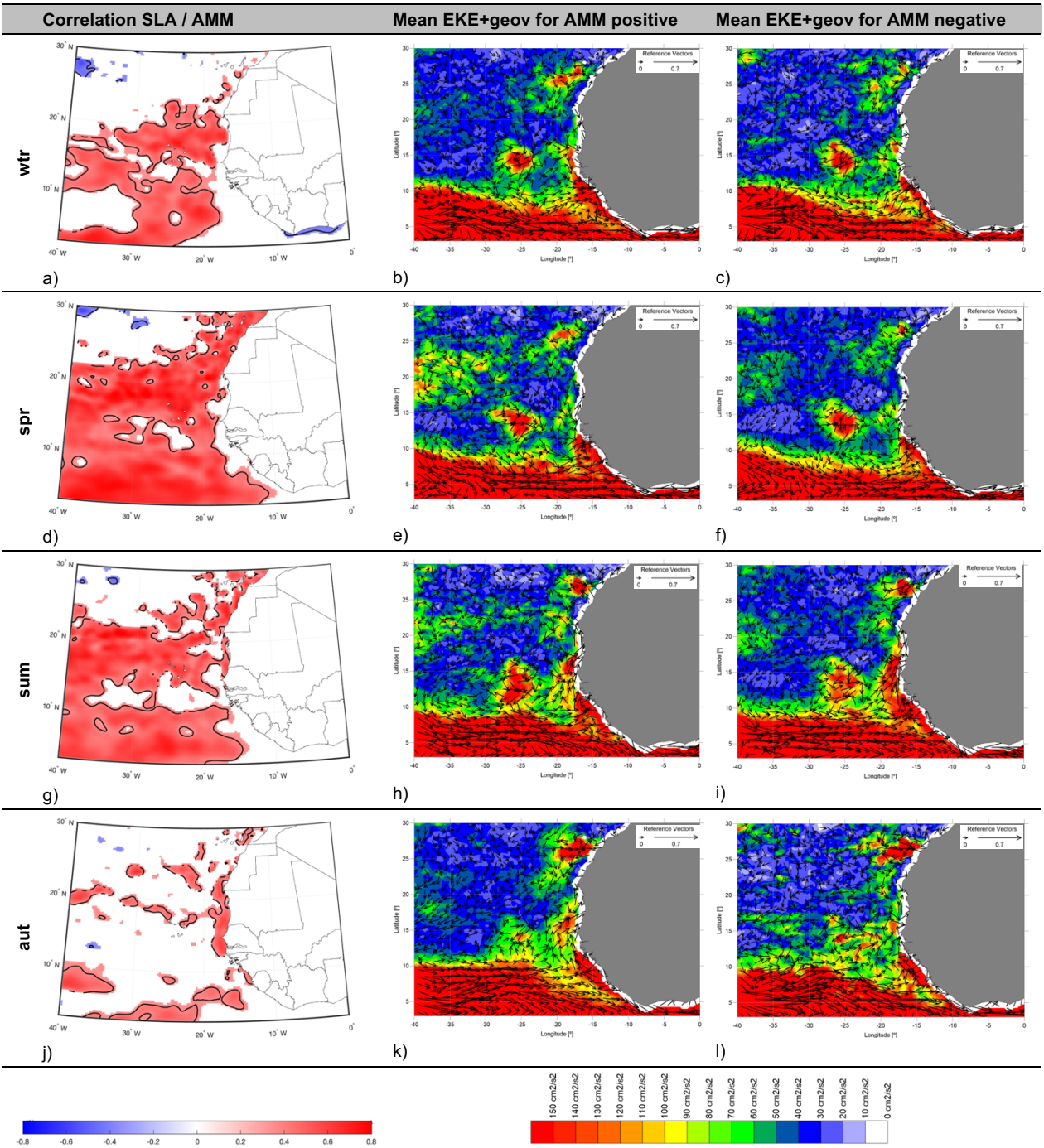

Figure 49 – Seasonal significant correlations (95% confidence) between SLA and AMM index (a, d, g, and j). EKE (in colour) and geostrophic velocities (in vectors in m/s) means during positive (b, e, h, and k) and negative (c, f, I, and l) phases of the AMM pattern. EKE colour scaling was saturated south of 10° N so that the energy patterns could emerge outside the band dominated by the NECC.

3.4.5 WHWP

The correlation between WHWP and SLA presents high positive values in spring and summer (Figure 50a and d) when the CI is stronger in the Atlantic Ocean. In spring, the correlation area is more extensive south of latitude 10°N, during NECC's minimum intensity season. During summer, on the other hand, the highest levels of correlation are located south of 20°N in the westward area of the study region between 40°W and approximately 27°W. The mean EKE maps during WHWP positive phases (Figure 50b and e) show higher values than the mean EKE maps during WHWP negative phases (Figure 50c and f).

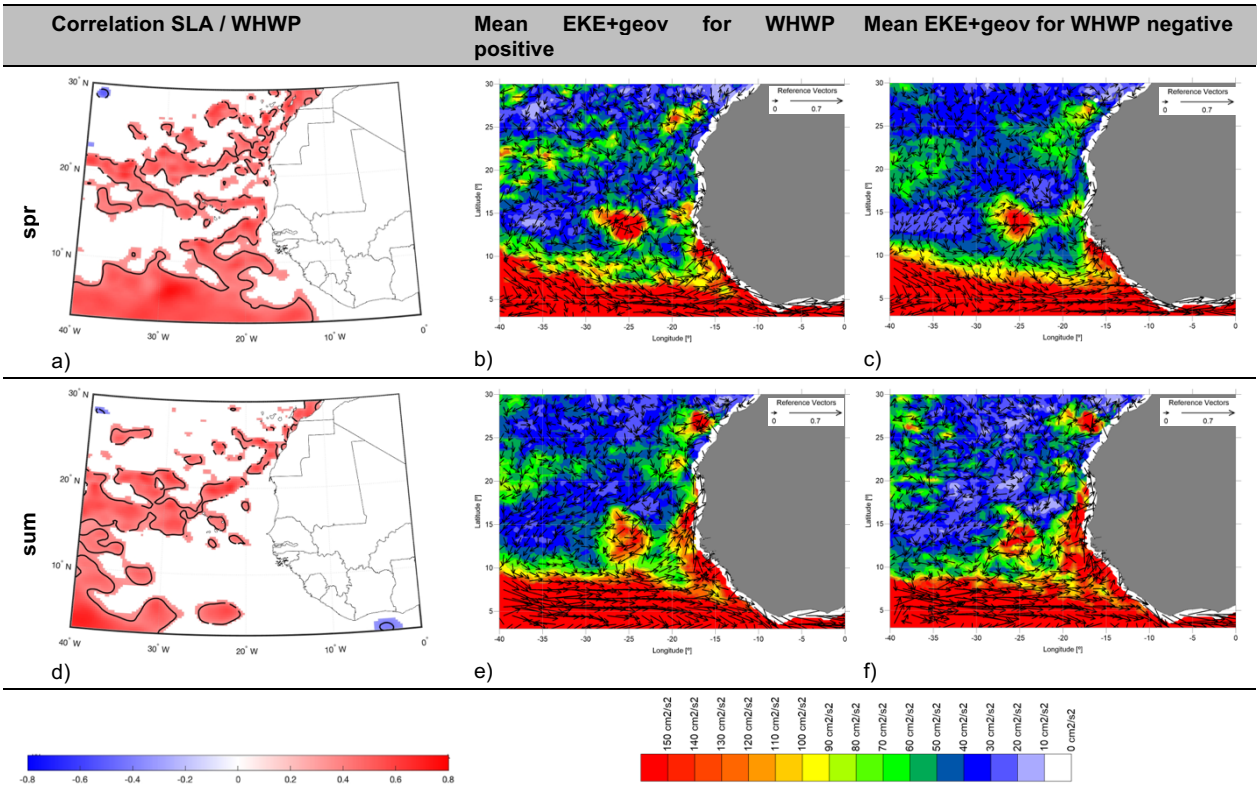

Figure 50 – Seasonal significant correlations (95% confidence) between SLA and WHWP index (a and d). EKE (in colour) and geostrophic velocities (in vectors in m/s) means during positive (b and e) and negative (c and f) phases of the WHWP pattern. EKE colour scaling was saturated south of 10° N so that the energy patterns could emerge outside the band dominated by the NECC.

The winter NAO phase has been referred to interfere either constructively (negative phase) or destructively (positive phase) with the strength of the warm pool that develops in the Atlantic Ocean (Enfield et al., 2006). Between 1993 and 2020, only two years with WHWP positive phases during summer were preceded by a NAO negative phase, in 1998 and 2010 after a very strong and a strong El Niño event, respectively. Figure 44e shows these were the two strongest warm pools registered during this period. On the other hand, even though 2015/16's winter registered the strongest El

Niño ever recorded since 1993, that year's winter NAO phase was positive and the positive summer warm pool was weaker than the ones in 1998 and 2010. These results are in good agreement with the NAO potential to reinforce or mitigate the SSTA that originated in the Pacific, as referred to in previous studies. Comparing the mean SLA for the seasons when WHWP is positive in summer and NAO is negative in winter (Figure 51a) with the mean SLA for the seasons when WHWP is positive in summer and NAO is positive in winter (Figure 51b), although the areas with positive SLA levels are more extensive during winter' NAO positive phases, they are also smoother and comprise more reduced amplitudes. The EKE levels are also higher during winter's NAO negative phases, particularly north of latitude 10°N, as well as the geostrophic velocities (Figure 51c and d).

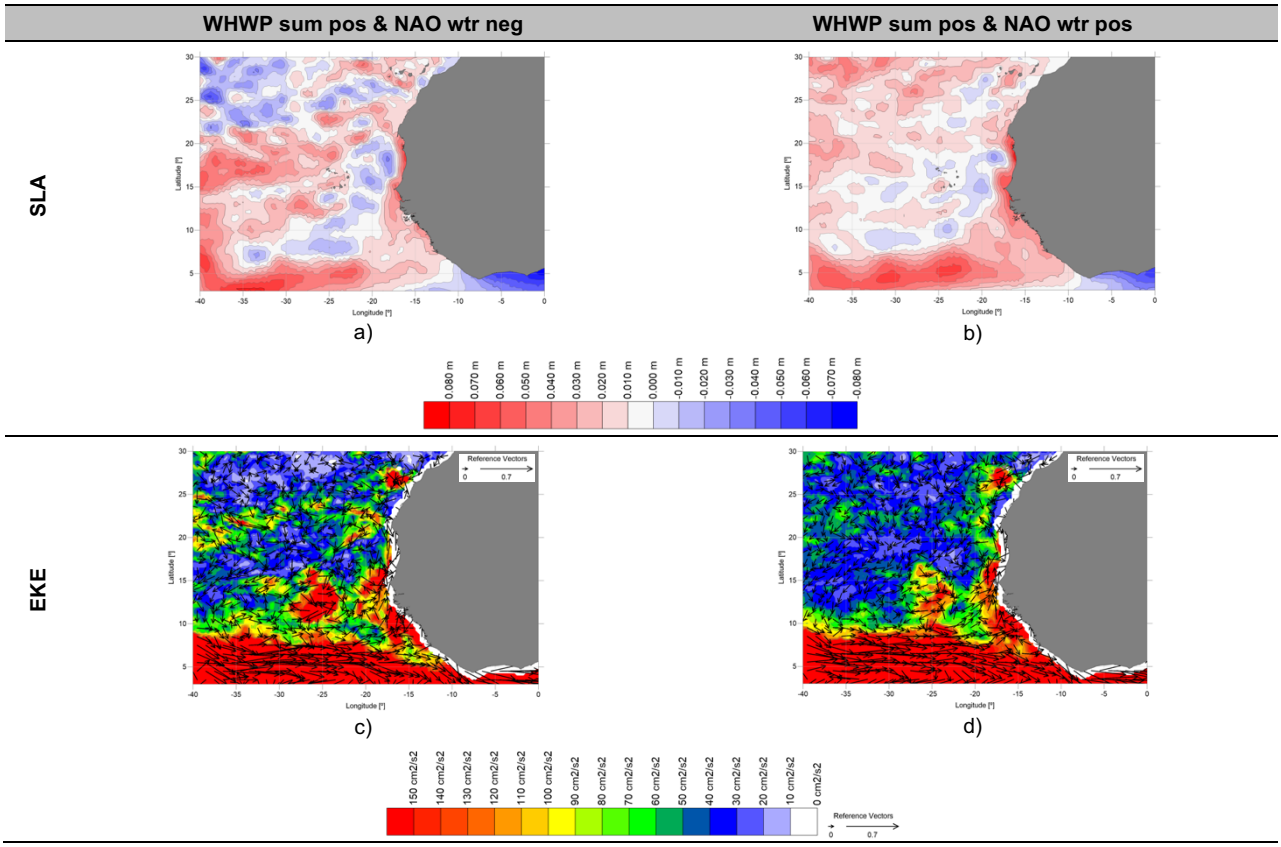

Figure 51 – Seasonal SLA (a and b) and EKE and geostrophic velocities (c and d) means when the WHWP phase is positive in summer and the NAO phase is negative in winter (a and c) or the NAO phase is positive in winter (b and d). EKE colour scaling was saturated south of 10° N so that the energy patterns could emerge outside the band dominated by the NECC.

3.4.6 SOI

Although the sea surface pressure centres to determine the SOI are located far in the Pacific, it is long recognised that this mode has a strong global impact (Power & Kociuba, 2011). The mean EKE when SOI phases are positive is higher than during SOI negative phases (Figure 52a).

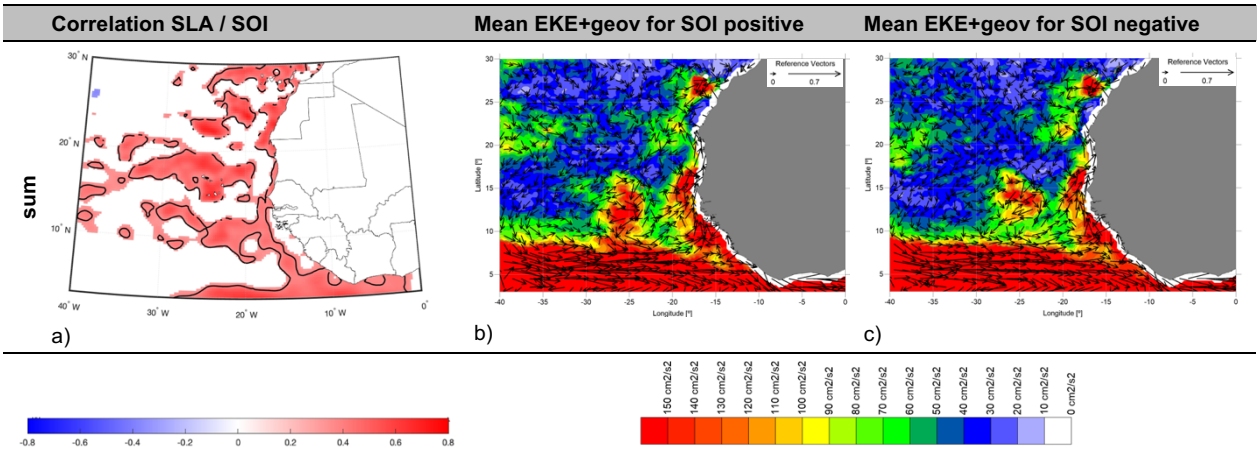

Figure 52 – Seasonal significant correlations (95% confidence) between SLA and SOI index (a). EKE (in colour) and geostrophic velocities (in vectors in m/s) means during positive (b) and negative (c) phases of the SOI pattern. EKE colour scaling was saturated south of 10° N so that the energy patterns could emerge outside the band dominated by the NECC.

4. Conclusions

The seal level anomaly (SLA), eddy kinetic energy (EKE), and magnitude of the surface geostrophic currents in the Eastern Tropical Atlantic Ocean (ETAO) region 3° to 30°N, 40°W to 0° present a strong seasonality, particularly south of 10°N which are related to the main currents in the area, namely the North Equatorial Counter Current (NECC). The sea level in the ETAO seems to be rising at a rate of 3.25 mm/y, higher than the global average of 3.15 mm/y (not including the GIA correction). On the other hand, the EKE presents a decreasing rate of -0.41 cm^2/s^2 per year, in opposition to the global strengthening of the mesoscale activity of 0.0064 cm^2/s^2 per year. A similar pattern occurs with the magnitude of the surface geostrophic currents, with a negative trend equal to -6.2×10^{-5} m/s per year in the ETAO while the global trend is positive and equal to 3.0×10^{-5} m/s per year. However, both EKE and magnitude seem to be strongly influenced by the results south of 10°N.

Moreover, atmospheric events may also be impacting the oceanic fields in this region. Along this study, strong correlations have been found between SLA and several climate indices (CI), namely the North Atlantic Oscillation (NAO), Tropical North Atlantic (TNA), Tropical South Atlantic (TSA), Atlantic Meridional Mode (AMM), Western Hemisphere Warm Pool (WHWP) and Southern Oscillation Index (SOI). Correlations between EKE or magnitude with each CI did not present significant values within the study region and so were excluded from this dissertation. North of 10°N and when the correlation between SLA and each CI is positive (negative), the mean EKE intensity seems to increase in the months when that CI is in a significantly positive (negative) phase. This energetic difference is more evident when the correlation areas are wider.

Given the six analysed CI, only NAO presented negative correlations with SLA and with a wider prevalence during winter, when it is stronger. The similarity between AMM and TNA correlations with SLA may be a consequence of their common areas of influence within de study region. On the other hand, even though TSA shares its area with AMM, its influence, despite neighbouring the study region, it's just outside, in the south. Therefore, correlations may be weaker and more focused in the southern upwelling region, closer to its northern latitude of influence. The apparent influence of the NAO on the strength of the WHWP seems to agree with previous studies (Enfield et al., 2006) but further investigation is needed. Since different CI act in the same region with different impacts and different time scales, cross-interference between some of them is

something that may be expected. Known interferences as well as probing for eventual new ones should be more thoroughly investigated.

Fine-tuning the different contributions to ocean circulation and its coupling with CI is essential to develop reliable models to monitor and predict climate variations in decadal and multidecadal timescales, following the objective of several research programs created since the early ’90s. Some examples of these programmes are the Atlantic Climate Change Program – ACCP (Molinari et al., 1994), the Climate Variability and Prediction Research Programme – CLIVAR[18] and the World Ocean Circulation Experiment – WOCE[19] (Griffies & Bryan, 1997). The ongoing climatic emergency urges fighting actions that should be taken based on the best and most detailed information available.

[18] https://usclivar.org/
[19] https://web.archive.org/web/20090417055821/http://www.noc.soton.ac.uk/OTHERS/woceipo/ipo.html

5. Future work

To better understand the correlations found between SLA and each CI in the ETAO, the main factors influencing the mean sea level variation should also be analysed, namely the SSTA, the SLP, the surface wind stress, and the precipitation patterns. The preparation of composite maps including these variables will help to understand the different contributions from each variable. They are also expected to help clarify which NAO and SOI atmospheric disturbances induce the strong correlations with SLA. It also may be of interest to review this study introducing a temporal lag between the oceanic variables and the climate indices, since the consequences of the variations might only be noticed in a delayed time window.

In addition to the NAO interference with WHWP, other cross-interference between different CI should also be investigated.

The EKE and surface geostrophic currents regional change should be further investigated, to assess the characteristics of the mesoscale activity and the phenomena influencing the results north and south of latitude 10°N.

Once the reprocessed TOPEX dataset is released, including the 1993-1998 instrumental drift correction, a review of this study should be considered, to include this correction.

References

Abdalla, S., Abdeh Kolahchi, A., Ablain, M., Adusumilli, S., Aich Bhowmick, S., Alou-Font, E., Amarouche, L., Andersen, O. B., Antich, H., Aouf, L., Arbic, B., Armitage, T., Arnault, S., Artana, C., Aulicino, G., Ayoub, N., Badulin, S., Baker, S., Banks, C., … Zlotnicki, V. (2021). Altimetry for the future: Building on 25 years of progress. *Advances in Space Research*, *68*(2), 319–363. https://doi.org/10.1016/j.asr.2021.01.022

Ablain, M., Cazenave, A., Larnicol, G., Balmaseda, M., Cipollini, P., Faugère, Y., Fernandes, M. J., Henry, O., Johannessen, J. A., Knudsen, P., Andersen, O., Legeais, J., Meyssignac, B., Picot, N., Roca, M., Rudenko, S., Scharffenberg, M. G., Stammer, D., Timms, G., & Benveniste, J. (2015). Improved sea level record over the satellite altimetry era (1993-2010) from the Climate Change Initiative project. *Ocean Science*, *11*(1), 67–82. https://doi.org/10.5194/os-11-67-2015

Arbic, B. K., Scott, R. B., Chelton, D. B., Richman, J. G., & Shriver, J. F. (2012). Effects of stencil width on surface ocean geostrophic velocity and vorticity estimation from gridded satellite altimeter data. *Journal of Geophysical Research: Oceans*, *117*(3). https://doi.org/10.1029/2011JC007367

Arnault, S., & Fonds, O. R. S. T. Q. M. (1987). Tropical Atlantic Geostrophic Currents and Ship Drifts. *JOURNAL OF GEOPHYSICAL RESEARCH*, *92*, 5076–5088.

Binfoff, N. L., Cheung, W. W. L., Kairo, J. G., Aristegui, J., Guinder, V. A., Hallberg, R., Hilimi, N., Jiao, N., Karim, M. S., Levin, L., O'Donoghue, S., Purca Cuicapusa, S. R., Rinkevich, B., Suga, T., Tagliabue, A., & Williamson, P. (2019). 2019: Changing Ocean, Marine Ecosystems, and Dependent Communities. In *The Ocean and Cryosphere in a Changing Climate*. Cambridge University Press. https://doi.org/10.1017/9781009157964.007

Bischof, B., Rowe, E., Mariano, A. J., & Ryan, E. H. (2004). *"The North Equatorial Current" Ocean Surface Currents (2004)*. https://oceancurrents.rsmas.miami.edu/atlantic/north-equatorial.html

Bonhoure, D., Rowe, E., Mariano, A. J., & Ryan, E. H. (2004). *"The South Equatorial Sys Current" Ocean Surface Currents (2004)*. https://oceancurrents.rsmas.miami.edu/atlantic/south-equatorial.html.

Cabanes, C., Cazenave, A., & le Provost, C. (2001). *Sea Level Rise During Past 40 Years Determined from Satellite and in Situ Observations* (Vol. 294). www.sciencemag.org

Chafik, L., Nilsen, J. E. Ø., & Dangendorf, S. (2017). Impact of North Atlantic teleconnection patterns on northern European sea level. *Journal of Marine Science and Engineering*, *5*(3). https://doi.org/10.3390/jmse5030043

Church, J. A., & White, N. J. (2011). Sea-Level Rise from the Late 19th to the Early 21st Century. *Surveys in Geophysics*, *32*(4–5), 585–602. https://doi.org/10.1007/s10712-011-9119-1

Climate Prediction Center Internet Team. (2022). *Historical El Nino / La Nina episodes (1950-present)*. https://origin.cpc.ncep.noaa.gov/products/analysis_monitoring/ensostuff/ONI_v5.php

Criado-Aldeanueva, F., & Soto-Navarro, J. (2020). Climatic indices over the mediterranean sea: A review. In *Applied Sciences (Switzerland)* (Vol. 10, Issue 17). MDPI AG. https://doi.org/10.3390/app10175790

Cygnus Team. (2015). *Cygnus Research International*. https://www.cygres.com/OcnPageE/Glosry/SpecE.html

de Viron, O., Dickey, J. O., & Ghil, M. (2013). Global modes of climate variability. *Geophysical Research Letters*, *40*(9), 1832–1837. https://doi.org/10.1002/grl.50386

Dimoune, D. M., Hernandez, F., & Araujo, M. (2020). Variability of the Atlantic Ocean North Equatorial Counter Current from 15 years of ADCP Observations and GLORYS12V1 Reanalysis. *Journal of Geophysical Research Oceans*. https://doi.org/10.1002/essoar.10504797.1

Doi, T., Tozuka, T., & Yamagata, T. (2009). Interannual variability of the Guinea Dome and its possible link with the Atlantic Meridional Mode. *Climate Dynamics*, *33*(7–8), 985–998. https://doi.org/10.1007/s00382-009-0574-z

Donev, J. M. K. C. et al. (2017). *Energy Education - North Atlantic Oscillation [online]*. https://energyeducation.ca/encyclopedia/North_Atlantic_Oscillation

Ducet, N., le Traon, P. Y., & Reverdin, G. (2000). Global high-resolution mapping of ocean circulation from TOPEX/Poseidon and ERS-1 and -2. *Journal of*

Geophysical Research: Oceans, *105*(C8), 19477–19498. https://doi.org/10.1029/2000jc900063

Efthymiadis, D., Hernandez, F., & le Traon, P.-Y. (2002). Large-scale sea-level variations and associated atmospheric forcing in the subtropical north-east Atlantic Ocean. In *Deep-Sea Research II* (Vol. 49).

Enfield, D. B., Lee, S. K., & Wang, C. (2006). How are large western hemisphere warm pools formed? *Progress in Oceanography*, *70*(2–4), 346–365. https://doi.org/10.1016/j.pocean.2005.07.006

Enfield, D. B., Mestas-Nuñez, A. M., Mayer, D. A., & Cid-Serrano, L. (1999). How ubiquitous is the dipole relationship in tropical Atlantic sea surface temperatures? *Journal of Geophysical Research: Oceans*, *104*(C4), 7841–7848. https://doi.org/10.1029/1998jc900109

Enfield, D. B., Mestas-Nuñez, A. M., & Trimble, P. J. (2001). The Atlantic multidecadal oscillation and its relation to rainfall and river flows in the continental U.S. *Geophysical Research Letters*, *28*(10), 2077–2080. https://doi.org/10.1029/2000GL012745

Erasmi, W., Siedler, G., & Onken, R. (1998). Energy conversion in the Cape Verde Frontal Zone. *Journal of Geophysical Research: Oceans*, *103*(C10), 21469–21479. https://doi.org/10.1029/98JC01887

Fernandes, J., & Lazaro, C. (2005). *Oceanographic Characterization of the Cape Verde Region Using Multisensor Data*. https://www.researchgate.net/publication/228998394

Griffies, S. M., & Bryan, K. (1997). A predictability study of simulated North Atlantic multidecadal variability. *Climate Dynamics*, *13*, 459–487.

Gyory, J., Bischof, B., Mariano, A. J., & Ryan, E. H. (2005). *The Guinea Current "Ocean Surface Currents (2005)*. https://oceancurrents.rsmas.miami.edu/atlantic/guinea.html

Gyory, J., Mariano, A. J., & Ryan, E. H. (2013). *"The Canary Current" Ocean SurfaceCurrents*. https://oceancurrents.rsmas.miami.edu/atlantic/canary.html

Hormann, V., Lumpkin, R., & Foltz, G. R. (2012). Interannual North Equatorial Countercurrent variability and its relation to tropical Atlantic climate modes.

Journal of Geophysical Research: Oceans, *117*(4). https://doi.org/10.1029/2011JC007697

Huang, B., & Shukla, J. (2005). *Ocean-Atmosphere Interactions in the Tropical and Subtropical Atlantic Ocean*.

Hurrel, J. W. (1995). Decadal Trends in the North Atlantic Oscillation: Regional Temperatures And Precipitation. *Science*, *269*, 676–679.

Iglesias, I., Lorenzo, M. N., Lázaro, C., Fernandes, M. J., & Bastos, L. (2017). Sea level anomaly in the North Atlantic and seas around Europe: Long-term variability and response to North Atlantic teleconnection patterns. *Science of the Total Environment*, *609*, 861–874. https://doi.org/10.1016/j.scitotenv.2017.07.220

Jung, J., & Cho, Y. K. (2020). Persistence of coastal upwelling after a plunge in upwelling-favourable wind. *Scientific Reports*, *10*(1). https://doi.org/10.1038/s41598-020-67785-x

Kämpf, J., & Chapman, P. (2016a). Other Important Upwelling Systems. In *Upwelling Systems of the World* (pp. 363–393). Springer International Publishing. https://doi.org/10.1007/978-3-319-42524-5_9

Kämpf, J., & Chapman, P. (2016b). The Functioning of Coastal Upwelling Systems. In *Upwelling Systems of the World* (pp. 31–65). Springer International Publishing. https://doi.org/10.1007/978-3-319-42524-5_2

Lagerloef, G. S. E., Mitchum, G. T., Lukas, R. B., & Niiler, P. P. (1999). *Tropical Pacific Near-Surface Currents Estimated from Altimeter, Wind, and Drifter Data Wind, and Drifter Data*.

Lázaro, C., Fernandes, M. J., Santos, A. M. P., & Oliveira, P. (2005). Seasonal and interannual variability of surface circulation in the Cape Verde region from 8 years of merged T/P and ERS-2 altimeter data. *Remote Sensing of Environment*, *98*(1), 45–62. https://doi.org/10.1016/j.rse.2005.06.005

Legeais, J.-F. (2021). *Copernicus Climate Change Service Product Quality Assessment Report Sea Level*.

Lindsey, R. (2009). *Climate Variability: Southern Oscillation Index*. https://www.cpc.ncep.noaa.gov/data/indices/soi

Martínez-Moreno, J., Hogg, A. M. C., England, M. H., Constantinou, N. C., Kiss, A. E., & Morrison, A. K. (2021). Global changes in oceanic mesoscale currents over the satellite altimetry record. *Nature Climate Change*, *11*(5), 397–403. https://doi.org/10.1038/s41558-021-01006-9

Mertz, F., & Legeais, J. (2020). *Copernicus Climate Change Service Product User Guide and Specification Sea Level v1.2*.

Mittelstaedt, E. (1991). *The ocean boundary along the northwest African coast: Circulation and oceanographic properties at the sea surface* (Vol. 26).

Molinari, R. L., Battisti, D., Bryan, K., & Walsh, J. (1994). The Atlantic Climate Change Program. *Bulletin of the American Meteorological Society*, *75*(7), 1191–1199.

Narayan, N., Paul, A., Mulitza, S., & Schulz, M. (2010). Trends in coastal upwelling intensity during the late 20th century. *Ocean Science*, *6*(3), 815–823. https://doi.org/10.5194/os-6-815-2010

Null, J. (2022). *El Niño and La Niña Years and Intensities*. https://ggweather.com/enso/oni.htm

Oppenheimer, M., Glavovic, B. V., Hinkel, J., vander Wal, R., Magnan, A. K., Abd-Elgawad, A., Cai, R., Cifuentes-Jara, DeConto, R. M., Ghosh, T., Hay, J., Isla, F., Marzeion, B., Meyssignac, B., & Sebesvari, Z. (2019). 2019: Sea Level Rise and Implications for Low-Lying Islands, Coasts and Communities. In *The Ocean and Cryosphere in a Changing Climate*. Cambridge University Press. https://doi.org/10.1017/9781009157964.006

Panagiotopoulos, F., Shahgedanova, M., & Stephenson, D. B. (2002). A review of Northern Hemisphere winter-time teleconnection patterns. *Journal De Physique. IV : JP*, *12*(10). https://doi.org/10.1051/jp4:20020450

Park, J. H., Kug, J. S., An, S. il, & Li, T. (2019). Role of the western hemisphere warm pool in climate variability over the western North Pacific. *Climate Dynamics*, *53*(5–6), 2743–2755. https://doi.org/10.1007/s00382-019-04652-0

Peltier, W. R. (2001). Global Glacial Isostatic Adjustment and Modern Instrumental Records of Relative Sea Level History. In B. C. Douglas, M. S. Kearney, & S. P. Leatherman (Eds.), *Sea Level Rise: History and Consequences* (Academic Press, pp. 65–95). International Geophysics Series, vol 75.

Peña-Izquierdo, J., Pelegrí, J. L., Pastor, M. v., Castellanos, P., Emelianov, M., Gasser, M., Salvador, J., & Vázquez-Domínguez, E. (2012). The continental slope current system between Cape Verde and the Canary Islands. *Scientia Marina*, *76*(SUPPL.1), 65–78. https://doi.org/10.3989/scimar.03607.18C

Philander, S. G. (2001). Atlantic Ocean Equatorial Currents. In *Encyclopedia of Ocean Sciences* (pp. 188–191). Elsevier. https://doi.org/10.1006/rwos.2001.0361

Power, S. B., & Kociuba, G. (2011). The impact of global warming on the Southern Oscillation Index. *Climate Dynamics*, *37*(9–10), 1745–1754. https://doi.org/10.1007/s00382-010-0951-7

Pujol, M. I., Faugère, Y., Taburet, G., Dupuy, S., Pelloquin, C., Ablain, M., & Picot, N. (2016). DUACS DT2014: The new multi-mission altimeter data set reprocessed over 20 years. *Ocean Science*, *12*(5), 1067–1090. https://doi.org/10.5194/os-12-1067-2016

Richardson, P. L., Arnault, S., Garzoli~, S., & Bruce, J. G. (1992). Annual cycle of the Atlantic North Equatorial Countercurrent. In *Deep-Sea Research* (Vol. 39, Issue 6).

Roberts, J. B., & Clayson, C. A. (2012). *Closing the seasonal ocean surface temperature balance in the Eastern tropical oceans from remote sensing and model reanalyses*.

Rodrigues, R. R., Rothstein, L. M., & Wimbush, M. (2007). Seasonal variability of the South Equatorial Current bifurcation in the Atlantic Ocean: A numerical study. *Journal of Physical Oceanography*, *37*(1), 16–30. https://doi.org/10.1175/JPO2983.1

Roldán-Gómez, P. J., González-Rouco, J. F., Melo-Aguilar, C., & Smerdon, J. E. (2022). The Role of Internal Variability in ITCZ Changes Over the Last Millennium. *Geophysical Research Letters*, *49*(4). https://doi.org/10.1029/2021GL096487

Rummel, R. (Reiner), & Sansò, F. (Fernando). (1993). *Satellite altimetry in geodesy and oceanography*. Springer-Verlag.

Sarr, C. A. T., Ndour, M. M. M., Haddad, M., & Sakho, I. (2021). Estimation of Sea Level Rise on the West African Coasts: Case of Senegal, Mauritania and Cape Verde. *International Journal of Geosciences*, *12*(02), 121–137. https://doi.org/10.4236/ijg.2021.122008

Servain, J., Wainer, L., McCreary, J. P., & Dessier, A. (1999). Relationship between the equatorial and meridional modes of climatic variability in the tropical Atlantic. *Geophysical Research Letters*, *26*(4), 485–488. https://doi.org/10.1029/1999GL900014

Skliris, N., Marsh, R., Appeaning Addo, K., & Oxenford, H. (2022). Physical drivers of pelagic sargassum bloom interannual variability in the Central West Atlantic over 2010–2020. *Ocean Dynamics*, *72*(6), 383–404. https://doi.org/10.1007/s10236-022-01511-1

Stephenson, D. B., Pavan, V., & Bojariu, R. (2000). Is the North Atlantic Oscillation a Random Walk? *INTERNATIONAL JOURNAL OF CLIMATOLOGY Int. J. Climatol*, *20*, 1–18. http://www.cru.uea.ac.uk/.

Stramma, L., & Schott, F. (1999). The mean flow field of the tropical Atlantic Ocean. In *Deep-Sea Research II* (Vol. 46).

Taburet, G., Mertz, F., & Legeais, J.-F. (2021). *Copernicus Climate Change Service Product User Guide and Specification Sea Level*.

Tamisiea, M. E., & Mitrovica, J. X. (2011). The moving boundaries of sea level change: Understanding the origins of geographic variability. *Oceanography*, *24*(2), 24–39. https://doi.org/10.5670/oceanog.2011.25

Torge, W., & Müller, J. (2012). *Geodesy*.

Vajda, P., Panisova, J., Vajda, P., & Pánisová, J. (2005). Practical comparison of formulae for computing normal gravity at the observation point with emphasis on the territory of Slovakia. *Contributions to Geophysics and Geodesy*, *35*. https://www.researchgate.net/publication/236035242

Vangriesheim, A., Bournot-Marec, C., & Fontan, A.-C. (2003). Flow variability near the Cape Verde frontal zone (subtropical Atlantic Ocean). In *Oceanologica Acta* (Vol. 26). www.elsevier.com/locate/oceact

Vimont, D. J., & Kossin, J. P. (2007). The Atlantic Meridional Mode and hurricane activity. *Geophysical Research Letters*, *34*(7). https://doi.org/10.1029/2007GL029683

Wagner, T., Beirle, S., Dörner, S., Borger, C., & van Malderen, R. (2021). Identification of atmospheric and oceanic teleconnection patterns in a 20-year global data set of the atmospheric water vapour column measured from satellites in the visible

spectral range. *Atmospheric Chemistry and Physics*, *21*(7), 5315–5353. https://doi.org/10.5194/acp-21-5315-2021

Waliser, D., & Jiang, X. (2015). *Encyclopedia of Atmospheric Sciences* (G. R. North, Ed.; Second Edition, Vol. 6). Elsevier.

Wallace, J. M., & Hobbs, P. v. (2006). *Atmospheric Science - An Introductory Survey*.

Wang, C., & Enfield, D. B. (2001). The tropical western hemisphere warm pool. *Geophysical Research Letters*, *28*(8), 1635–1638. https://doi.org/10.1029/2000GL011763

Woolf, D. K., Shaw, A. G. P., & Tsimplis, M. N. (2003). The influence of the North Atlantic Oscillation on sea-level variability in the North Atlantic region. *Global Atmosphere and Ocean System*, *9*(4), 145–167. https://doi.org/10.1080/10236730310001633803

Zhang, H., Ma, X., Zhao, S., & Kong, L. (2021). Advances in Research on the ITCZ: Mean Position, Model Bias, and Anthropogenic Aerosol Influences. In *Journal of Meteorological Research* (Vol. 35, Issue 5, pp. 729–742). Chinese Meteorological Society. https://doi.org/10.1007/s13351-021-0203-2